Phanerozoic Exhumation History of Hall Peninsula, Baffin Island: Insights from Apatite and Zircon (U-Th-Sm)/He Thermochronology and 3D Thermokinematic Modeling

by

C. Gabriel Creason

Submitted in partial fulfillment of the requirements
for the degree of Master of Science

at

Dalhousie University
Halifax, Nova Scotia
April 2015

TABLE OF CONTENTS

LIST OF TABLES

LIST OF FIGURES

ABSTRACT

The eastern Canadian Arctic Rim (eCAR) is a rugged, high-relief landscape extending along the continental margin from northern Labrador to southeastern Ellesmere Island. While much of the relief along the eCAR may be related to rift-flank uplift and incision during and after rifting between Canada and Greenland, rock thermal histories derived from previous thermochronologic studies from the northern and southern regions of the eCAR, as well as in West Greenland, are incompatible with a single, representative exhumation history for the entire eCAR. Potential causes for the disparate histories include the existence of a crustal root under Labrador and multiple rifting events over the past 400 Ma. This study aims to characterize the long-term exhumation history of Hall Peninsula, Baffin Island, and, by linking together previous thermochronologic studies in the eCAR, test various models of tectonic and geomorphic evolution of southeastern Baffin Island.

In total, 28 rock samples, collected along one vertical and two iso-elevation transects, were analyzed by low-temperature (U-Th-Sm)/He thermochronometry (26 apatite-He (AHe), 7 zircon-He (ZHe); 5 aliquots each) to help define the cooling history of the rocks on Hall Peninsula. Results from these samples reveal highly dispersed cooling ages, spanning 75–1078 Ma in the AHe data, and 326–1229 Ma in the ZHe data. Strong correlations between effective U concentration (eU = U + 0.235*Th + 0.005*Sm) and AHe and ZHe cooling age indicate that the cooling ages are heavily influenced by the effects of alpha-recoil damage. Thermal modeling of individual samples (using HeFTy) suggests a history of protracted, slow cooling across the entire Peninsula, with most cooling events initiating from middle Paleozoic. This is supported by the results of modeling with a 3D thermokinematic program (PECUBE) to determine the collective tT history of the rocks on Hall Peninsula. A series of tectonomorphic scenarios were simulated in PECUBE to test whether the spatial distribution of AHe ages could be explained through a simple (i.e., vertical) exhumation by erosional processes, or if it requires a more complex exhumational history (e.g., faulting). Despite the limitations of the highly dispersed data, the results from both the HeFTy and PECUBE models indicate that Hall Peninsula experienced extremely slow cooling (≤ 1 ºC/Ma) throughout the Phanerozoic. The models are consistent with a regional Carboniferous-Permian cooling event that may have triggered rapid cooling, followed by an extremely slow exhumation averaging less than 10 m/Ma. In contrast to the Greenland conjugate margin and Torngat Mountains to the south, it appears that Hall Peninsula did not experience rapid cooling during rifting between Baffin Island and Greenland.

LIST OF ABBREVIATIONS USED

AFT – Apatite Fission-track Thermochronometry

AHe – Apatite (U-Th-Sm)/He Thermochronometry

Bt – Biotite

C-NGO – Canada-Nunavut Geoscience Office

DGC – Dalhousie Geochronology Centre

eCAR – Eastern Canadian Arctic Rim

ECSOOT – Eastern Canadian Shield Onshore-Offshore Transect

eU – Effective Uranium Concentration

GOF – Goodness-of-fit

Grt – Garnet

GSC – Geological Survey of Canada

Hbl – Hornblende

HePRZ – Helium Partial Retention Zone

HeTM – Helium Trapping Model

Kfs – Potassium Feldspar

Ms – Muscovite

NA – Neighborhood Algorithm

Opx – Orthopyroxene

RDAAM – Radiation Damage Accumulation and Annealing Model

Sil – Sillimanite

T_c – Closure Temperature

THO – Trans-Hudson Orogen

UFZ – Ungava Fault Zone

UT – University of Texas, Austin

ZHe – Zircon (U-Th-Sm)/He Thermochronometry

ZRDAAM – Zircon Radiation Damage Accumulation and Annealing Model

ACKNOWLEDGEMENTS

I am especially thankful to my advisor, John Gosse; without his unwavering enthusiasm and persistent encouragement, this project would not have been possible. I thank Mike Young for not only his guidance with this project, but also for sharing his wealth of knowledge in the practice of field geology. I am grateful to David Whipp for his help and direction with the use of PECUBE, and for his valuable advice in navigating this project.

I owe much gratitude to the Gosse-ling research group – Guang Yang, Lea Braschi, Annina Margreth, Alan Hidy and Tom Lakeman – for the lively scientific discussions and continued support. Many thanks to Matt Kliffer for his assistance with sample processing. Roman Kislitsyn and Danny Stockli are thanked for their guidance and assistance with lab analyses. I am thankful to Pierre Valla for generously sharing with us his modified PECUBE code. I also thank the entire faculty and staff of the Earth Sciences Department at Dalhousie for the help and support provided both in the classroom and with my research. I must also thank my fellow graduate students for their friendship and the entertainment they provided during my time at Dalhousie. Thank you to my friends and family, in particular my parents, for your moral support and encouragement during my pursuit of this degree. Lastly, but certainly not least, I thank my partner and best friend, Whitney Moore, for her endless support.

CHAPTER 1 – INTRODUCTION

1.1 Introduction

The eastern Canadian Arctic Rim (eCAR) comprises a barren, rugged, high elevation and high relief terrain that spans over 1200 km, across various structural, lithologic, and cratonic domains from Labrador to Ellesmere Island, (Fig. 1.1). Topography in this terrain exceeds 1500 m in a narrow strip within 100–200 km of the coastal margin. Beyond the high relief coastal regions, much of the eCAR maintains its high elevation, but in a low relief landscape that progressively decreases elevation landward. How does such a high relief region along a passive continental margin evolve? One hypothesis is that the eCAR has formed as a result of rift-flank uplift. The landscape morphology of eCAR is consistent with many ancient and modern rift margins around the world such as the eastern Australian continental margin, western margin of Scandinavia, and Eritrean margin of the Red Sea.

While the syn- and post-rift sediments preserved offshore, where present, record the denudation of the eCAR and other elevated passive margins, the record is insufficient for reconstructing the onshore evolution of the margin (i.e., changes in the rate and style of exhumation cannot be reconstructed from a complex and incomplete marine sedimentary record) or for testing the rift-flank uplift hypothesis. To establish the detailed history needed to characterize the spatial and temporal variations in the landscape evolution of these regions, a more indirect approach that measures the thermal history of crustal rocks has been employed (e.g., Braun and van der Beek, 2004). This ‘thermochronology’ has been achieved with (U-Th-Sm)/He and fission-track analyses in apatite, owing to the sensitivity of those methods to temperature histories ≤ 120 ºC. For a typical geothermal

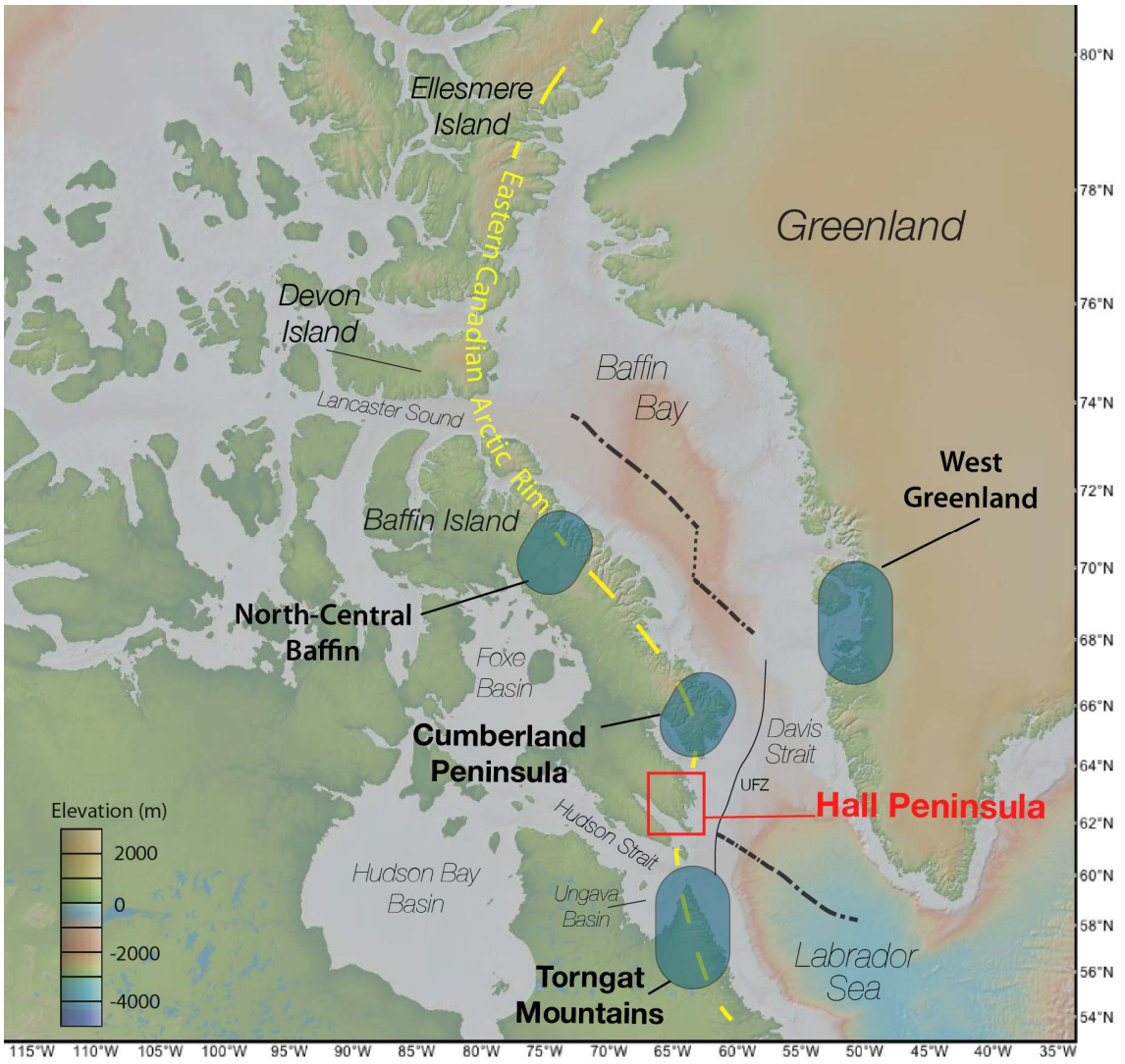

Figure 1.1. Eastern Canadian Arctic Rim (eCAR). Dashed yellow line follows high-relief terrain of the eCAR. Bold dashed line is approximate location of extinct spreading axis of Baffin Bay and Labrador Sea, from Oakey and Chalmers (2012). Bold dotted line is approximate location of the transform margin, from Chalmers and Pulvertaft (2001) and Oakey and Chalmers (2012); thin black line is Ungava Fault Zone (UFZ), from (Chalmers and Pulvertaft, 2001). Shaded blue regions denote locations of previous low-temperature thermochronology studies (see text for discussion). Modified from Creason et al. (2013).

gradient of 20–30 ºC/km, these and other thermochronometers record temperatures that correspond to the upper 4–6 km of the crust, and hence yield information regarding the processes acting at or near the surface, making them ideal for depicting the geologic history of erosion, sedimentation, or faulting (Ehlers and Farley, 2003).

Informed with thermochronology results, the conventional understanding of the development of these elevated continental margin landscapes ascribes them as a byproduct of the rifting process, with much of the relief having been generated by incision in response to rift-flank uplift (e.g., Balestrieri et al., 2005; Brown et al., 2002; Gallagher and Brown, 1999; Persano et al., 2002). However, a renewed debate over the fundamentals of the landscape evolution of elevated passive margins, such as those in Northern Europe and Greenland, has called the role of rift-flank uplift into question. For example, recently it has been proposed by some that, in addition to rift-related uplift, the elevated topography in these landscapes is inherited from an earlier pre-rift event, possibly being remnant of an ancient orogen (e.g., McGregor et al., 2013; Nielsen et al., 2009b). Still others have argued for the contrary, purporting that elevated passive continental margins are not remnants of ancient orogens, or necessarily even the result of rift-flank uplift, but instead that the elevated margins have formed during renewed, post-rift tectonism, unrelated to the rifting process (e.g., Japsen et al., 2012).

Development of the high relief of the eCAR could correspond to uplift and exhumation during and after rifting between Canada and Greenland. However, previous studies investigating the landscape evolution of the eCAR and the response to rifting have yielded contrasting results. In the south, thermochronology of the Torngat Mountains reveals that the topography was generated around 150 Ma, concurrent with offshore rift sediments and basalts, as a result of rapid rift-flank uplift of a margin supported by a buoyant crustal root (Centeno, 2005). The spatial distribution of cooling ages indicates the rift margin evolved via a pinned-divide style of erosion since that time. However, to the north, thermochronology reveals that the pattern of apatite-helium (AHe)

ages on the north-central Baffin Island margin predate separation from Greenland, and mimics that of both pinned-divide and escarpment-retreat landscape evolution recognized at other rift shoulders (Yaehne, 2008).

The main objective of this thesis is to characterize the exhumation history of Hall Peninsula using a combination of low-temperature thermochronometers ((U-Th-Sm)/He in apatite and zircon) and thermal modeling. Because Hall Peninsula is situated along the eCAR at a location between the previous studies of Centeno (2005) and Yaehne (2008), a thermochronology study here serves to link the contrasting exhumation histories, providing insight into the variable exhumation along the length of the eCAR. This study also aims to establish the various controls on exhumation with the aid of a 3D thermokinematic modeling program. This involves developing models to test in an attempt to link patterns in the exhumation record with potential non-rift processes, such as motion along offshore faults or the tilting of plausible grabens (e.g. Frobisher Bay and Cumberland Sound) defined by rift boundaries. Together, these results will help better define a comprehensive, long-term exhumation history of the eCAR.

To achieve these objectives, the samples analyzed this study were collected along one vertical and two horizontal transects across Hall Peninsula (Fig. 1.2), in an arrangement consistent with previous thermochronologic studies in the eCAR (Centeno, 2005; Yaehne, 2008), as well as in other elevated passive margins (e.g., Balestrieri et al., 2005; Persano et al., 2002). The goal of the vertical transect was to determine variations in the cooling rate due to vertical exhumation, and establish if there is rapid cooling that could reflect rift-flank uplift. A coastline-perpendicular transect was collected with the aim of providing evidence for differential cooling across the margin as a result of erosion during

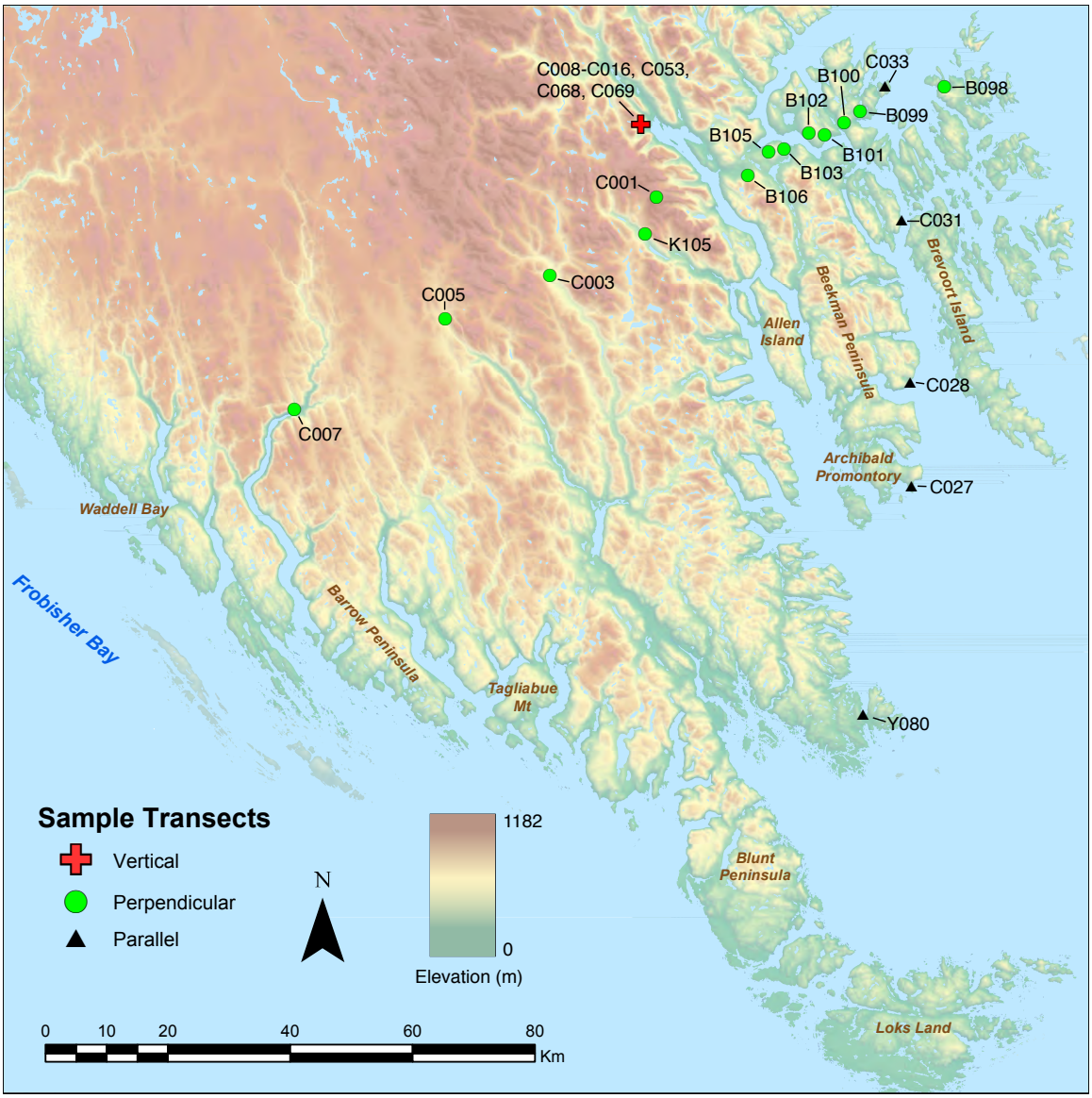

Figure 1.2. Apatite and zircon (U-Th-Sm)/He sample locations. In total 28 samples were collected along three transects: one perpendicular and one parallel to the Cumberland Sound coastline, sampled at a constant elevation (~250 m and 0 m, respectively); and one vertically oriented, sampled at various elevations, in order to capture the maximum topographic relief in the smallest horizontal distance.

rift-flank uplift, tilting of the crustal block or motion along bounding faults. The motivation for collecting a coastline-parallel transect was to constrain the timing of incision of the numerous fjords along the coast, as well as provide evidence for any differential cooling along the peninsula margin (i.e., as a result of tectonic tilting).

This study is part of a multi-year, collaborative effort between Dalhousie Geochronology Centre (DGC), the Geological Survey of Canada (GSC), the Canada-Nunavut Geoscience Office (C-NGO), and the University of Texas, Austin (UT). In addition to testing the hypotheses and ideas of the geomorphic and tectonic history of Hall Peninsula, and placing it in the context of the eCAR, this research also contributes to our understanding of the exhumation of Paleozoic stratigraphy on Baffin Island, as well as the sediment flux to the Cumberland Sound and Frobisher Bay. Knowledge of the sediment flux from Hall Peninsula will be helpful for ongoing petroleum interests in the region. Given the recent development of offshore Ordovician carbonates and organic-rich shale as a potential source rock, these results provide timely information for the stratigraphic characterization of the Baffin Shelf region, having direct implications for the renewed interest in the petroleum exploration in Cumberland Sound (e.g., Zhang, 2013; Zhang et al., 2014).

CHAPTER 2 – BACKGROUND

2.1 Geologic setting

2.1.1 Precambrian tectonics

Hall Peninsula is located on southeastern Baffin Island and forms part of the Paleoproterozoic Trans-Hudson Orogen (THO), a Himalayan-scale collisional orogenic belt that extends from south-central to northeastern North America (Hoffman, 1988; Lewry and Collerson, 1990; St-Onge et al., 2009). The bedrock of Hall Peninsula is divided into two general domains (Machado et al., 2013; Scott, 1996), each remnant of deformation and metamorphism at various stages of the THO. The eastern domain of Hall Peninsula comprises an Archean tonalite orthogneiss complex, with a crystallization age of 2842 ±3 Ma (zircon U-Pb; Rayner, 2014), while the western domain consists mostly of pelitic to psammitic metasedimentary rocks, deposited between ca. 2.1–1.9 Ga (zircon U-Pb; Rayner, 2014), that are variably intruded by orthopyroxene-bearing diorite to monzogranite (ca. 1.89 – 1.85 Ga; zircon U-Pb; Rayner, 2014; Scott, 1999) (Fig. 2.1). Preliminary estimates for the timing of peak metamorphic conditions on Hall Peninsula during the THO are between ca. 1.85–1.83 Ga (Skipton et al., 2013), yet cooling ages between 1690 ±3 to 1657 ±3 Ma from muscovite $^{40}Ar/^{39}Ar$ thermochronology reveal that elevated post-peak metamorphism temperatures (i.e., ≥ 420 ºC) were maintained for at least 140 Ma, providing evidence for protracted, slow cooling following orogenesis (Skipton et al., 2015).

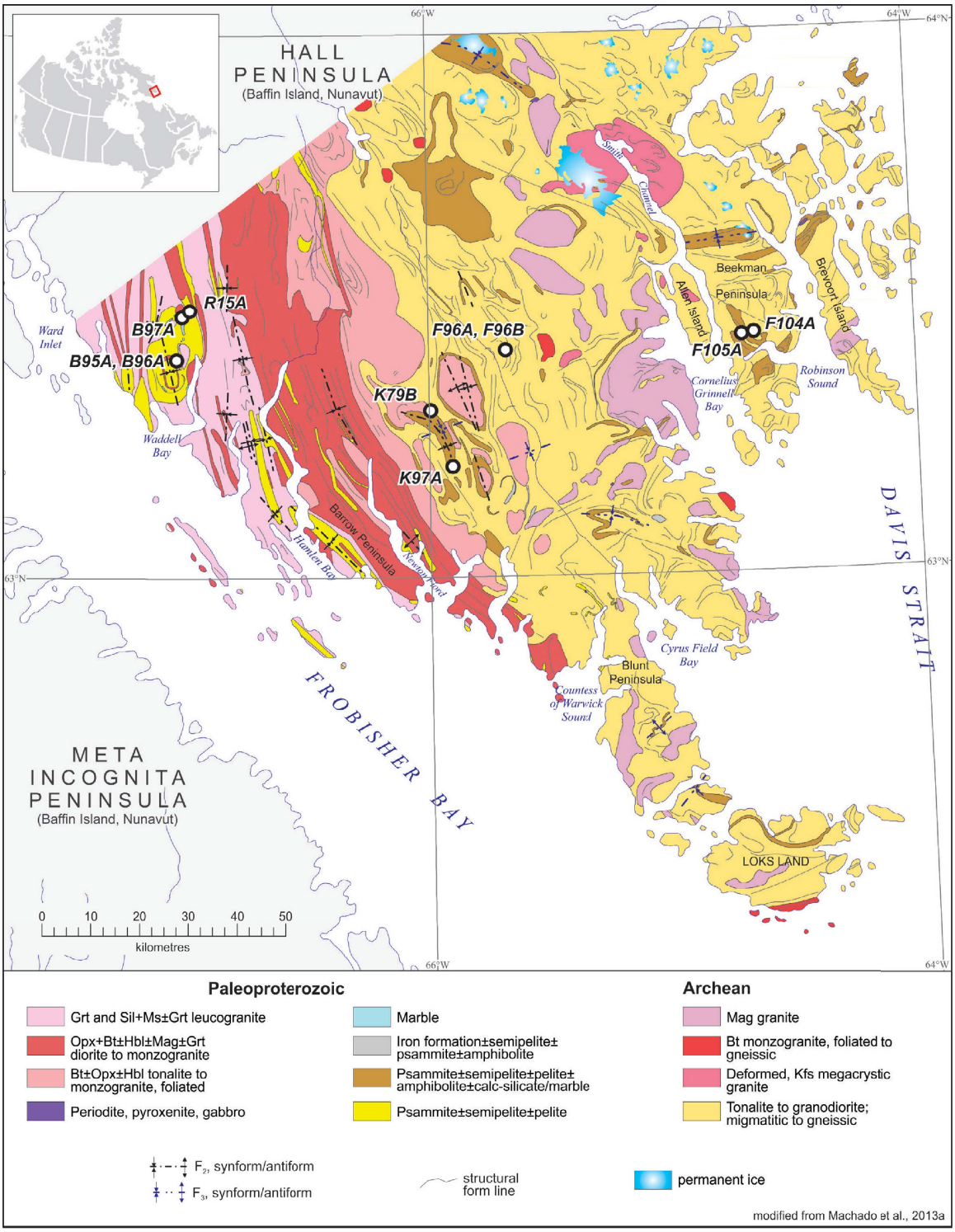

Figure 2.1. Simplified bedrock geology map of southern Hall Peninsula, Baffin Island. Samples indicated were analyzed for zircon U-Pb geochronology (Rayner, 2014). Mineral abbreviations: Grt, garnet; Sil, sillimanite; Ms, muscovite; Opx, orthopyroxene; Bt, biotite; Hbl, hornblende; Kfs, potassium feldspar. From Rayner (2014) (modified after Machado et al., 2013).

2.1.2 Phanerozoic history

Presently no Phanerozoic-aged rocks crop out on Hall Peninsula; however, this was not always the case. Hall Peninsula is located along the eastern margin of the southeast Arctic platform, which in the early to middle Paleozoic served as a stage for widespread

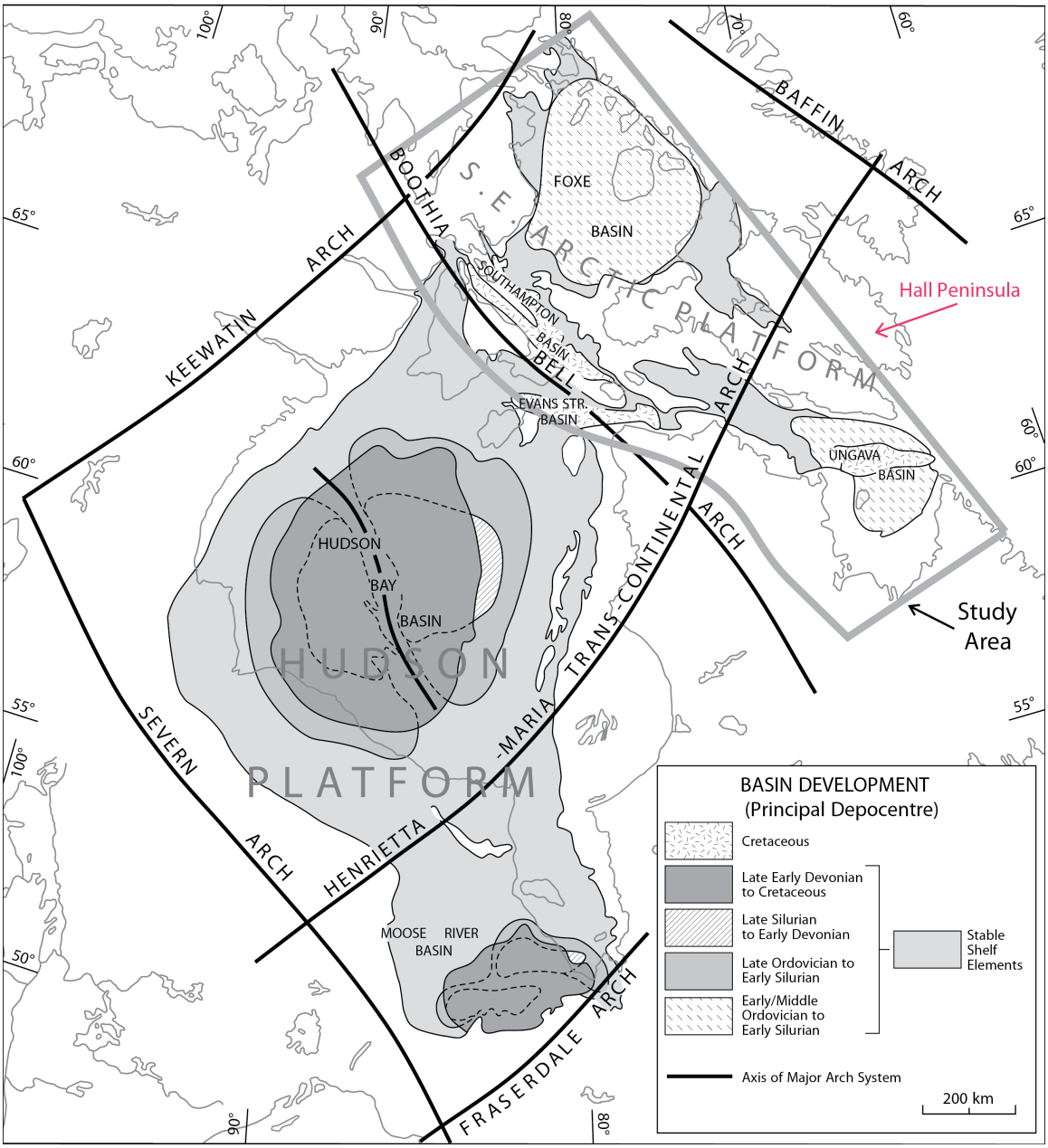

Figure 2.2. Location of Hall Peninsula relative to the southeastern Arctic and Hudson platforms, highlighting the prominent arch systems defining Phanerozoic tectonic activity. Modified from Sanford and Grant (2000).

deposition of marine successions (Fig. 2.2) (Sanford, 1987). At that time a network of orthogonal arches, spanning around and through the Hudson and southeastern Arctic platforms, persisted as structural highs and largely controlled the regional distribution of marine seaways and deposition of the marine sediments (Sanford, 1987). Deposition of the km-thick, late Proterozoic Bylot Supergroup on northern Baffin Island in NW-trending fault-bound basins oriented sub-parallel to these arches (e.g., Baffin Arch; Fig. 2.2) suggests that orientation of these arches may be linked to pre-existing faults of large offset. Reactivation of the arch-forming structures at various times in the Paleozoic is accredited with forming many of the basins and sub-basins (half-grabens) in the eastern Arctic (e.g., Foxe Basin, Hudson Bay Basin, Ungava Basin) (Fig. 2.3) (Sanford and Grant, 1990, 1998). Most notably, in the Early Silurian basement uplift along these arches resulted in epiorogeny, manifested as large-scale block-faulting throughout the platforms (Sanford and Grant, 2000). A final episode of uplift of the arch systems occurred during the Cretaceous, continuing the deformation style of block-faulting, resulting in half-graben development and subsequent sedimentation within the Hudson Strait (Ungava Basin), Southampton Basin (Sanford and Grant, 2000) and Cumberland Sound (MacLean et al., 1982; MacLean et al., 1986).

While erosion of the cratonic cover during the Phanerozoic has removed onshore evidence for this deposition, much of the record is preserved offshore. Seismic and core records collected around southeastern Baffin Island reveal Paleozoic through Cenozoic sediments on the seafloor of both Frobisher Bay and Cumberland Sound (MacLean et al., 1977; MacLean et al., 1982; Sanford and Grant, 1998). Furthermore, Jurassic kimberlites on Hall Peninsula contain traces of an Ordovician limestone entrained as xenoliths in

Jurassic intrusions (Zhang and Pell, 2013; Zhang and Pell, 2014). Although rare, these xenoliths provide key evidence for the history of sedimentary cover on the peninsula. Analyses of conodont microfossils within the carbonate xenoliths revealed that they correlate with the Upper Ordovician and Lower Silurian lithostratigraphic units found in drill core collected offshore in Frobisher Bay and Cumberland Sound, as well as

A

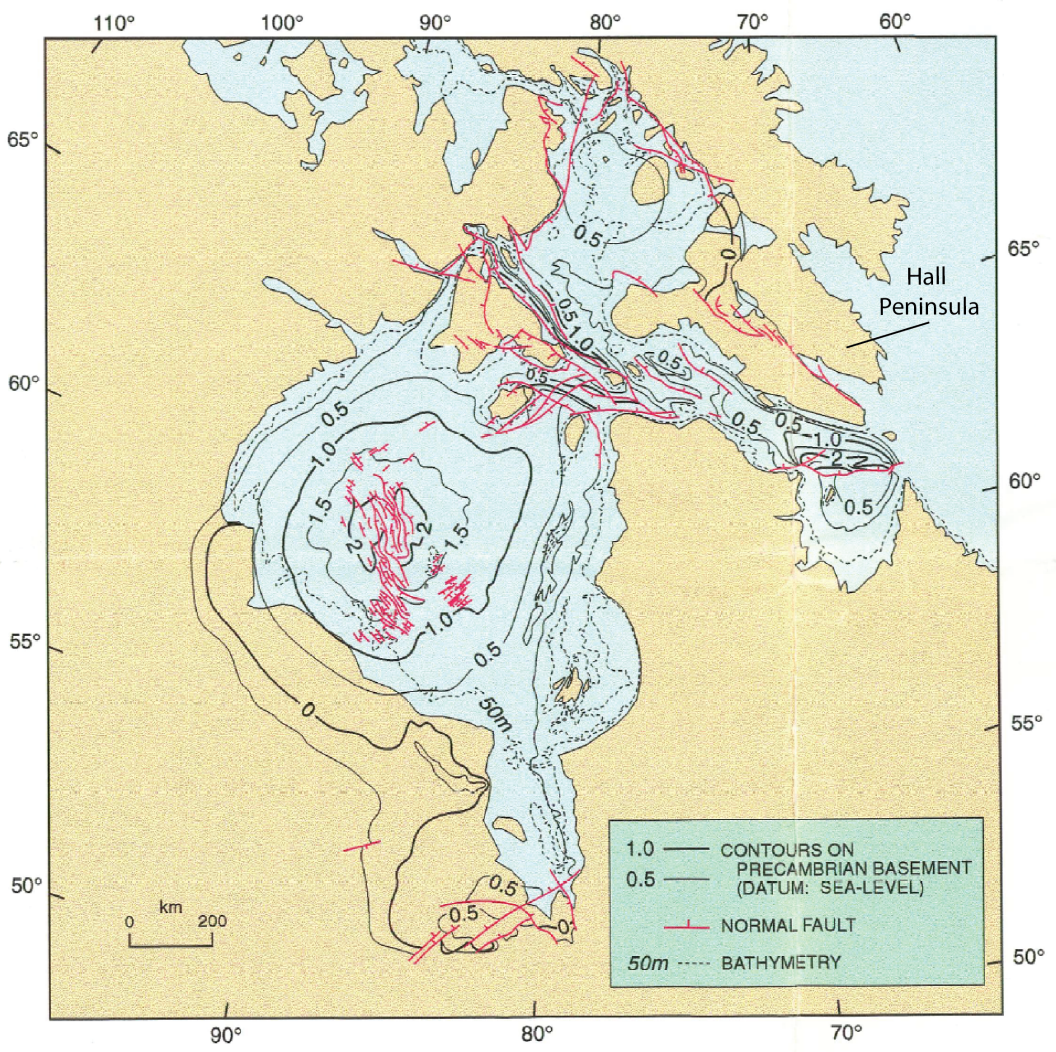

Figure 2.3. (A) Structural and (B) tectonic framework of the Hudson and southeastern Arctic platforms. Modified from Sanford and Grant (1998). Figure continues on next page.

B

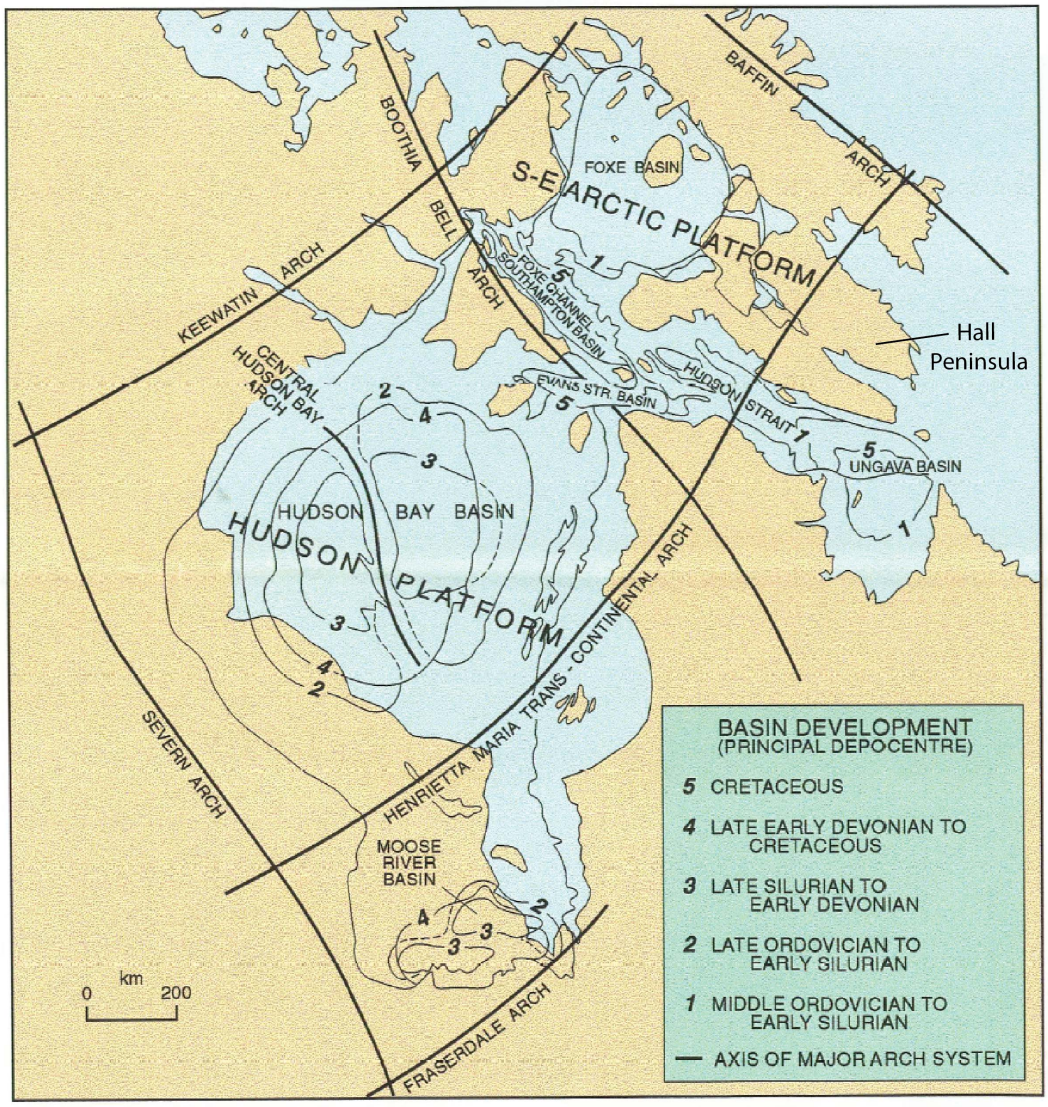

elsewhere in the Foxe Basin and Hudson Platform (Zhang and Pell, 2014). Through their correlations, Zhang and Pell (2014) were able to use the established thicknesses of the units elsewhere in the eastern Arctic to estimate thickness for the sedimentary cover on Hall Peninsula, prior to the emplacement of the kimberlites, between 270-305 m. Their observations demonstrate that Hall Peninsula was once overlain by an extensive cover that has since been removed, and, at the very least, provide a minimum average erosion rate of 2-3 m/Ma since the Jurassic.

2.1.3 Labrador Sea, Davis Strait, and Baffin Bay

The opening of the Labrador Sea, Davis Strait and Baffin Bay in the late Mesozoic–early Cenozoic was the most recent major tectonic event to affect northeastern. The onset of extension in proto-Baffin Bay and Labrador Sea is interpreted to have occurred between ca. 223–150 Ma, based on the age and composition of dyke swarms in West Greenland (Larsen et al., 2009). A distinct change in the composition of Late Jurassic dykes (ca. 150 Ma) has been cited as evidence that extension rates increased markedly during this time (Larsen et al., 2009). Extension in the proto-Labrador Sea was followed by rifting in the Early Cretaceous, evidenced by the emplacement of regional, coast-parallel dyke swarms (>400 km in length) in southwest Greenland (Watt, 1969). However, no evidence has been found for Jurassic rifting in Baffin Bay (Schenk, 2011). The earliest rift basalts and half-graben basin fill off northern Labrador (the Alexis and Bjarni Formations) occurred just after 150 Ma (Umpleby, 1979) . For the Davis Strait and Baffin Bay region, this was followed by punctuated periods of subsidence, sedimentation, faulting and magmatism (Chalmers and Pulvertaft, 2001; Larsen et al., 2009) until the initiation of seafloor spreading during Paleocene times (Chalmers and Laursen, 1995; Chalmers and Pulvertaft, 2001). Seafloor spreading continued through Paleocene to Eocene times (Funck et al., 2012; Suckro et al., 2012), during which the extension propagated northward to Baffin Bay, connecting through the Davis Strait by way of transtensional to transpressional motion along the Ungava Fault Zone (Funck et al., 2007) and Hudson Fracture Zone (Suckro et al., 2013). Transtensional extension in the Davis Strait is marked by extensive volcanism, thought to be coeval with the arrival of the proto-Icelandic plume at ca. 62 Ma (Gerlings et al., 2009). No evidence exists for

seafloor spreading in Baffin Bay or Labrador Sea after mid-Eocene times (Chalmers and Pulvertaft, 2001).

2.2 Rift evolution of the eastern Canadian Arctic Rim

Although the conventional paradigm predicts much of the relief along the eCAR may have been generated by incision in response to rift-flank uplift during and after rifting between Canada and Greenland, this hypothesis has not been tested along the entirety of its length (e.g., Torngat Mountains, northern Labrador, Centeno, 2005; north-central Baffin Island, NunavutYaehne, 2008), and the results from recent studies, demonstrating a variation in the exhumation style of the eCAR, further add to the debate over the evolution of landscapes in rifted margins. Meanwhile, knowledge of the evolution of the eastern Arctic Canadian passive continental margin has improved substantially in the past two decades because of an increase in marine seismic, magnetic, and gravity measurements (Funck et al., 2012; Funck et al., 2007; Gerlings et al., 2009; Skaarup et al., 2006; Suckro et al., 2012; Suckro et al., 2013) and more sophisticated geodynamical models (Oakey and Chalmers, 2012). At the same time, improvements in the application of low temperature thermochronometry (Flowers and Kelley, 2011; Flowers and Schoene, 2010; Shuster et al., 2006) and landscape evolution models for rift margins (Japsen et al., 2012; Nielsen et al., 2009b; Osmundsen and Redfield, 2011; Redfield and Osmundsen, 2012) have helped rejuvenate questions regarding the evolution of the North Atlantic along the eastern North American, Greenland, and Scandinavian margins.

2.2.1 Passive margin evolution

Thinning of the crust and lithosphere shortly after rift initiation, and before and during breakup, results in a combination of isostatic imbalance and thermal upwelling

forces that manifest along the rift margins as vertical motion, in an effect referred to as rift-flank uplift (Braun and Beaumont, 1989; Buck, 1986; McKenzie, 1978) (Fig. 2.4). However, because these forces operate for different time spans, their relative contribution to the rock and surface uplift varies with time. For example, the thermal effects of lithospheric thinning are thought to last only as a long as 50 Ma, while the isostatic response can last for much longer (Braun and Beaumont, 1989; Gallagher and Brown, 1997). Still, while the processes involved in forming passive continental margins are relatively more understood, the forces which drive post-rift evolution, and ultimately the longevity of continental margin escarpments and high elevation plains, remains the focus of continued debate (Chalmers et al., 2010; Japsen et al., 2006; Japsen et al., 2012; Japsen et al., 2013; Nielsen et al., 2010; Nielsen et al., 2009a; Nielsen et al., 2009b; Osmundsen and Redfield, 2011; Pedersen et al., 2012; Pedersen et al., 2013).

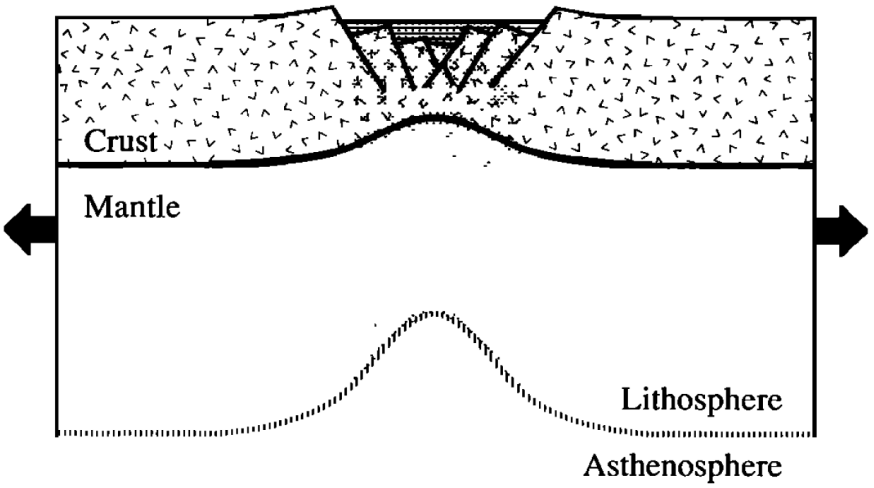

Figure 2.4. Schematic cross section of the crust and lithosphere during extension. Isostatic imbalance and thermal upwelling of hot asthenosphere result in uplift along the rift flanks. From Buck (1991).

Figure 2.5. Hypothetical 2-D cooling age-distance relationship for a transect of samples collected perpendicular to the margin, for two different end-member scenarios of rift-flank evolution. (A) Escarpment retreat model, which suggests uniform denudation across the escarpment, resulting in a 'wave' of linear landward retreat. The model predicts a gradual increase in cooling ages towards the modern escarpment, and relatively consistent ages thereafter. (B) Pinned divide / plateau degradation model, with denudation controlled by pre-existing drainages, resulting in downwearing of the escarpment. The model predicts a similar cooling ages for the low-elevation coastal region seaward of the modern escarpment, with an abrupt increase in cooling age at or near the escarpment, and a decreasing trend farther landward. From Gallagher and Brown (1999).

A

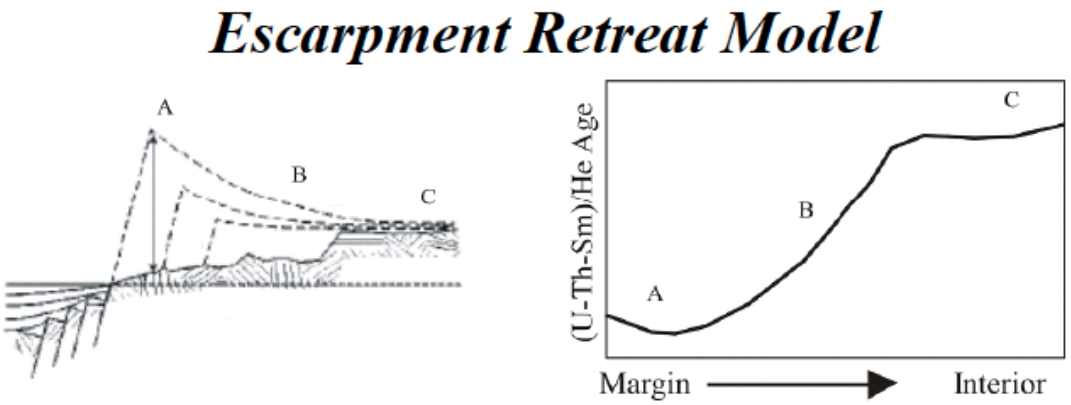

B

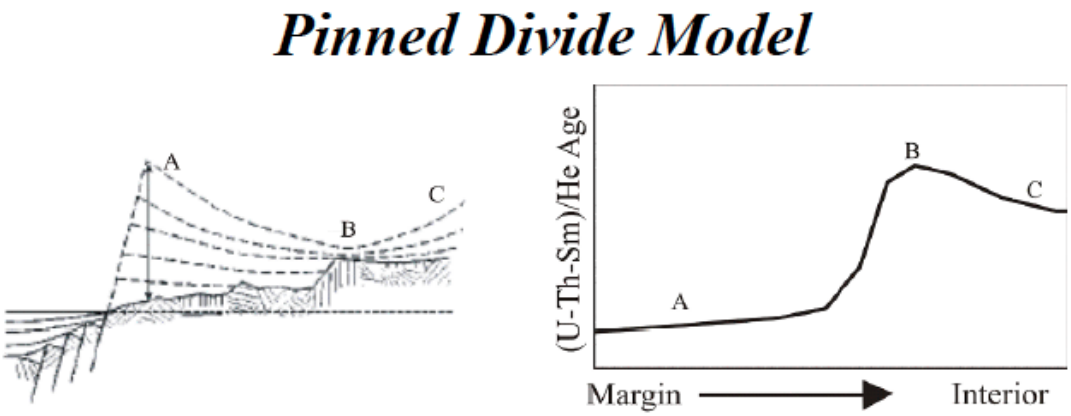

Many modern continental passive margins exhibit morphologies typified by large, seaward facing escarpments that divide a low elevation coastal area from a high-elevation, low relief interior plateau region (Kooi and Beaumont, 1994; van der Beek et al., 1995).

Our knowledge of the evolution of these rift shoulders has improved from geodynamical models that include surface processes (e.g., Kooi and Beaumont, 1994; van der Beek et al., 1995), and low-temperature thermochronology (e.g., apatite (U-Th-Sm)/He or apatite fission-track analyses; Gallagher and Brown, 1997; Gallagher et al., 1994). These studies led to the conventional understanding that rift-margin landscapes evolve through two end-member type scenarios (Fig. 2.5).

The first scenario involves a setting with denudation focused along the escarpment face, and minimal amounts of denudation occurring in the coastal area or interior plateau as the escarpment retreats landward (Fig. 2.5A). The alternative model is one of a pinned divide, or plateau degradation scenario, in which denudation of the escarpment is affected by a network of antecedent drainages. Denudation occurs on both sides of a drainage divide, rather than only along the escarpment face, resulting in a vertical downwearing of the rift-flank (Fig. 2.5B). However, since these two models can result in a morphologically similar landscape, insight from low-temperature thermochronology is often used to construe the detailed evolution of these landscapes. This approach has been used to characterize the escarpment evolution of several passive margins, including: the Great Escarpment of South Africa (Gallagher and Brown, 1999), the Drakensburg Escarpment (Brown et al., 2002) and the Blue Ridge escarpment of the eastern United States (Spotila et al., 2004).

2.2.2 Torngat Mountains

At the southernmost region of the eCAR, the Torngat Mountains are located along a high-relief margin with geophysical and thermochronological evidence for the presence of an anomalously thick (~50 km) crust. Discovery of the ~15 km crustal root by Funck

and Louden (1999) was based upon a wide-angle seismic transect for the Lithoprobe Eastern Canadian Shield Onshore-Offshore Transect (ECSOOT), although the 2-D nature of the study permitted only limited characterization of its geometry and composition. Through subsequent seismic tomography work by Funck et al. (2000), it was proposed that the root amalgamated during the ca. 1.86 Ga oblique convergence between the Archean Nain and SE Churchill cratons, and the subsequent development of the Abloviak Shear Zone along this boundary (ca. 1.82–1.80 Ga) led to the dismemberment of the root.

Results from apatite (U-Th-Sm)/He thermochronology in samples collected in a vertically-oriented transect provide evidence that the Torngat Mountains experienced a period of rapid cooling (from >80 to <40 ºC) between 150–140 Ma, coincident with the early stages of rifting in the Labrador Sea (Fig. 2.6; Centeno, 2005). The rapid cooling event was interpreted as a phase of accelerated, isostatically-driven uplift and exhumation in response to buoyant forces of the anomalously thick crustal root, with an average exhumation rate of ~240 m/Ma during this time, preceded and followed by a much slower average exhumation rate (10–15 m/Ma). Samples collected in a margin-perpendicular transect yielded a distribution of cooling ages that support a pinned-divide-type model for the margin evolution (Centeno, 2005). Samples collected along two iso-elevation margin-parallel transects revealed a sinusoidal pattern in the He ages that mimicked the wavelength of the topography owing to a circa regular spacing of the west-east major valleys that cut through the Torngat Mountains. The inferred relationship was interpreted to indicate that much of the fluvially-generated topography was created in the Mesozoic and Paleogene, much earlier than the Quaternary glacial incision that is commonly cited for relief generation in the region (Kessler et al., 2008).

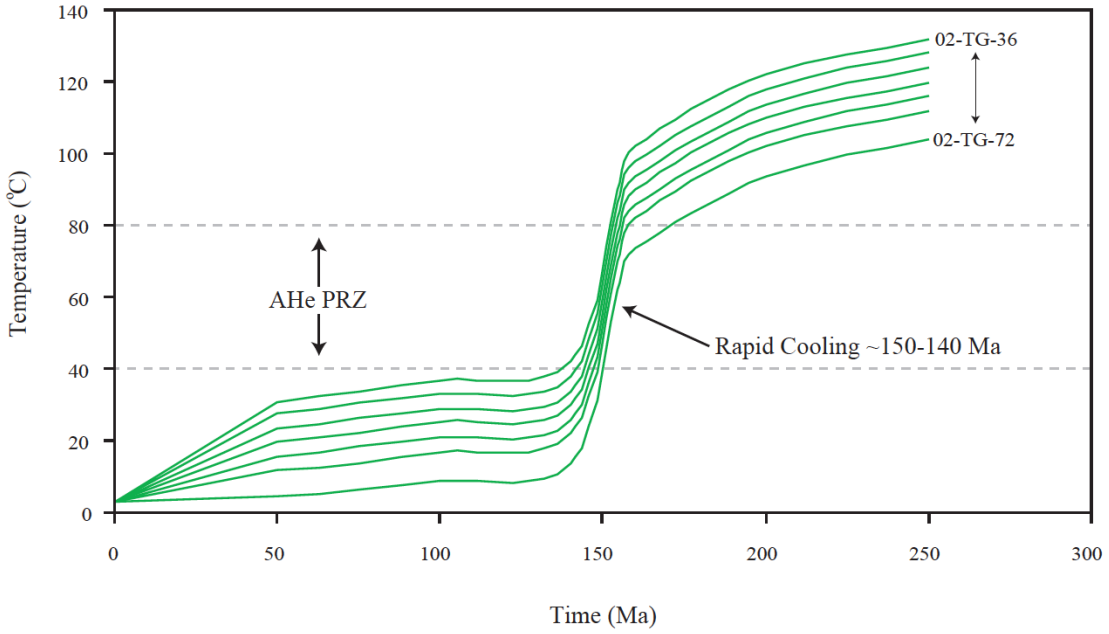

Figure 2.6. Best-fit time-temperature paths for samples from the Mount D'Iberville vertical transect in the Torngat Mountains, indicating a cooling history with accelerated rate of cooling between 160-140 Ma (Centeno, 2005). AHe PRZ is apatite helium partial retention zone (i.e., the range of temperatures in which helium retention is neither fully open or closed).

2.2.3 Baffin Island

Northward and across Hudson Strait from Labrador, a similar high-elevation high-relief terrain is maintained on north-central Baffin Island, however this region lacks evidence for an anomalously thick crust. Using a similar strategy to Centeno (2005), Yaehne (2008) collected samples in two transects (one vertical, one perpendicular to the offshore margin). However, in contrast to the Torngat Mountains, AHe cooling ages from the vertical transect,Yaehne (2008) indicated a slow and more constant cooling history, with low average exhumation rates of 10–13 m/Ma throughout Cenozoic and Mesozoic times, with no evidence for accelerated uplift during rifting in Baffin Bay. Results from the margin-perpendicular transect revealed a pattern of differential cooling on both sides of a pinned drainage divide, but notably younger ages near the Baffin Bay margin. These

were interpreted to reflect an exhumational style that was generated by a combination of the pinned divide and escarpment retreat (Yaehne, 2008).

Similarly, a history of slow cooling was also demonstrated for Cumberland Peninsula. Apatite fission-track ages presented by McGregor et al. (2013), ranging between ca. 440–200 Ma, support a history of very slow cooling. Based on the old cooling ages, they argue that the margin exhibited no exhumational response to late Mesozoic–early Cenozoic activity in the Baffin Bay/Davis Strait Region. McGregor et al. (2013) thus conclude that the majority of the present-day topography on Cumberland Peninsula is a remnant of earlier, higher topography formed in the Paleoproterozoic.

2.2.4 West Greenland

Despite its location on the conjugate side of Baffin Bay, interpretations for the evolution of the West Greenland margin differ from that of the Canadian margin. Using a combination of low-temperature thermochronology (Japsen et al., 2006; Japsen et al., 2005) and landscape analysis (Bonow et al., 2006a; Bonow et al., 2006b), previous studies have interpreted a history of renewed, post-rift uplift for the Canada-Greenland margins. This interpretation calls into question whether these landscapes reflect processes that occurred during or just after rifting, or, instead, later events that were unrelated to rifting processes. More recent studies have built upon this work, arguing for short lifespans for many passive margin landscapes, citing the presence of young peneplains and regional-scale unconformities as evidence for post-rift uplift and erosion, as recent as Neogene in West Greenland (Bonow et al., 2014; Japsen et al., 2006; Japsen et al., 2012; Japsen et al., 2005, 2013; Lidmar-Bergström et al., 2013). However, this interpretation remains highly contested, as the interpretation of AFT data has been largely disputed

(Green et al., 2011; Redfield, 2010), in addition to the understanding of the tectonic mechanisms responsible for the recent uplift (McGregor et al., 2012).

2.3 Late Cenozoic

The modern topography on Baffin Island has most certainly been generated by fluvial processes and glacial erosion (Sugden, 1976), but the rates and styles of landscape evolution have varied substantially spatially and temporally (Montgomery, 2002; Staiger et al., 2005). For instance, a high elevation low relief central zone on Hall Peninsula exhibits extensive weathering profiles through regolith, in stark contrast to the northeastern zones with glacier scouring, higher lake density, and deep glacial troughs feeding into the Cumberland Sound. Deep weathering profiles on summit plateaus are not uncommon in the Eastern Arctic Rim, and reflect the wide ranges of subglacial erosion that occur under polythermal ice covers. The timing and rates of erosion for specific locations or processes in the Quaternary are difficult to ascertain, and even the origin of the 1-km deep fiords—fluvial or glacial—remains debated.

CHAPTER 3 – METHODOLOGY

3.1 Overview of (U-Th-Sm)/He Thermochronology

The (U-Th-Sm)/He thermochronology method is based on the alpha decay of ^{238}U, ^{235}U, ^{232}Th and ^{147}Sm, and retention of ^{4}He within a mineral cooled below a specific range of temperatures (T_c) (Farley, 2002). When the minerals are above T_c, ^{4}He diffusion is equal to or greater than the rate of production, maintaining a state of dynamic equilibrium with an effective cooling age of zero (Farley 2002). Thus, a measurement of the parent/daughter ratio can provide the duration of time since the mineral cooled below T_c. However, complete ^{4}He retention does not occur instantaneously as the grain cools below a specific temperature, but rather it happens gradually over range of temperatures. This temperature range, known as the He partial retention zone (HePRZ; Wolf et al., 1998), is the span of temperatures where ^{4}He is neither fully retained nor completely diffused from the grain, and is primarily a function of cooling rate, decreasing as the cooling rate increases. Apatite and zircon are particularly useful thermochronometers due to their exceptionally low T_c (~70 ºC and ~180 ºC, respectively), making them ideal candidates for characterizing exhumational processes that affect the thermal field in the uppermost crust (e.g., incision, changes in exhumation rates, faulting) (Ehlers and Farley, 2003; Reiners, 2005). Furthermore, apatite-He (AHe) and zircon-He (ZHe) data analyzed in the same sample can yield additional insight into the thermal history by providing a sense of the rate of change of cooling with time.

In the case of slow cooling (< 1 ºC/Ma) and prolonged residence time in the He partial retention zone, apatite and zircon grains may no longer conform to well-

understood standard diffusion kinetics (e.g., Durango apatite; Farley, 2000), and thus require additional considerations when interpreting their cooling ages (e.g., Flowers and Kelley, 2011; Flowers et al., 2007; Green et al., 2006; Reiners, 2005; and others). In these circumstances, ^{4}He diffusion will be sensitive to the accumulation of defects in the crystal caused by prolonged exposure to alpha-emission recoil (Farley, 2000; Shuster et al., 2006). Although the occurrence of radiation damage has long been realized (e.g., Hurley, 1954), its relevance and importance to AHe and ZHe thermochronometry has been appreciated within only the last decade (Flowers et al., 2009; Gautheron et al., 2013; Gautheron et al., 2009; Guenthner et al., 2013; Nasdala et al., 2004; Shuster and Farley, 2009; Shuster et al., 2006).

3.2 Samples and Sampling Strategy

Twenty-eight rock samples were analyzed for (U-Th-Sm)/He data (21 AHe only, 7 AHe and ZHe; 5 aliquots each). Samples were collected during the 2012 Hall Peninsula Integrated Geoscience Project field season of the C-NGO, in cooperation with the bedrock and surficial mapping campaigns. The sampling strategy was based on a transect approach, comprising three different transects: a vertical transect of 10 samples covering 800 m relief across only 950 m horizontally; and two nearly constant elevation transects, with 13 samples collected perpendicular to the Cumberland Sound coastline, and 5 samples collected in a coastline-parallel orientation (sampled at ~250 m and ~0 m elevation, respectively) (Fig. 1.2). This sampling strategy follows the guidelines of Braun and van der Beek (2004) to utilize a transect sampling approach when collecting low-T thermochronology samples as an effective method for discerning an exhumational response to rifting in a passive-margin tectonic setting. The strategy also considered that

the deflection of isotherms by the periodically spaced deep valleys and fiords could be reflected in the distribution of He-ages along a single elevation (Centeno, 2005; House et al., 1998). Additionally, nine samples were collected at various elevations from across the peninsula to provide constraints for a 3D exhumation model (discussed in chapter 6), however, due to logistical constraints, these samples were not analyzed for this study.

3.3 (U-Th-Sm)/He Analysis

AHe and ZHe data were analyzed according to the standard procedure for (U-Th)/He thermochronology (Farley, 2002): mineral separation, grain selection, ^{4}He extraction, and U-Th-Sm analysis. Samples were initially pulverized to fragments less than 1 cm using a jawcrusher, then pulverized into grains less than 500 μm using a disk-mill. The first stage of separation was achieved using a Wilfley water table, where the grains are sorted into two groups, 'heavy' and 'light', with respect to their density. Heavy separates were further differentiated through density separation by immersion in a heavy liquid (i.e., lithium heteropolytungstates). The more dense separates were then put through a Frantz magnetic separator to selectively concentrate the apatite and zircon grains based on their magnetic susceptibility. The final step of mineral isolation involved using a stereomicroscope to observe the heavy mineral separates and extracting the candidate apatite and zircon grains. Grain selection was based on several criteria: minimum grain dimension (≥ 70 μm), euhedral grain shape, absence of inclusions or fractures, and lack of apparent chemical zoning. Once grains were selected, grain geometry was measured to ensure an appropriate correction for the amount of ^{4}He ejected from each grain (i.e., alpha-ejection correction; Farley et al., 1996). After measurement, each grain was packed into a platinum sleeve, placed onto a small planchette, loaded into an ultrahigh vacuum

He extraction line for He degassing. Degassing occurred by heating each individual aliquot with a neodymium-yttrium-aluminum-garnet laser to 1070 ºC for five minutes (apatite) or 1300 ºC for 10 minutes (zircon). All aliquots were reheated to ensure complete degassing (< 1% He during re-extract). An ultrahigh vacuum (UHV) noble gas extraction line routed the degassed helium to a Blazers Prisma QMS-200 quadrupole mass spectrometer where it was quantified. After complete degassing of He, the aliquots were removed and prepared for heavy isotope analysis. Each aliquot was dissolved and spiked with a known concentration of ^{230}Th, ^{235}U, and ^{149}Sm. After complete dissolution, ^{238}U, ^{232}Th, and ^{147}Sm isotope concentrations were analyzed using a Thermo Element2 HR inductively-coupled plasma mass spectrometer. All analytical work was carried out by C. Gabriel Creason: physical processing of samples was conducted at the Crystal Isolation Facility at the DGC; final grain selection and isotopic measurements were at carried out at the Jackson School of Geosciences (U-Th)/He and U-Pb Geo-Thermochronometry Lab at UT, under the guidance and supervision of Dr. Roman Kislitsyn and Dr. Danny Stockli.

CHAPTER 4 – APATITE AND ZIRCON (U-Th-Sm)/He RESULTS

4.1 Summary

In total, 105 AHe and 35 ZHe single-grain cooling ages were produced from 28 rock samples (Table 1). Most samples yielded abundant quantities of large, euhedral (gem-quality), inclusion-free apatite and zircon grains (Fig. 4.1); only two samples (C031 and C033) failed to yield datable apatite grains and thus were not included in the study (Table 2a-g). Despite the exceptional quality of the apatite and zircon grains, the measured He-ages exhibit a significant amount of dispersion (100+ Ma), even between aliquots of the same sample (Figs. 4.2–4.5). The considerable range in aliquot cooling ages precludes a straightforward interpretation of the data using the arithmetic mean of the aliquot ages for the cooling age of each sample. Even with weighted means or modal ages for each sample, there is no obvious relationship between cooling age and elevation in the vertical transect samples, or a spatial trend in cooling ages from the coastline-parallel or coastline-perpendicular samples (e.g., Gallagher and Brown, 1999). Fortunately, in recent years much effort has focused on characterizing (U-Th-Sm)/He data with large amounts of scatter in the aliquot cooling ages, providing insight to the potential causes of the dispersion (e.g., Flowers et al., 2009; Gautheron et al., 2009; Guenthner et al., 2013; Shuster et al., 2006). Presented here are the He cooling ages that were computed with the program Helios, without consideration of the effects of alpha-recoil damage or other causes of scatter. A detailed discussion of the sources of scatter and interpretation of the He ages is provided in Chapter 5.

A

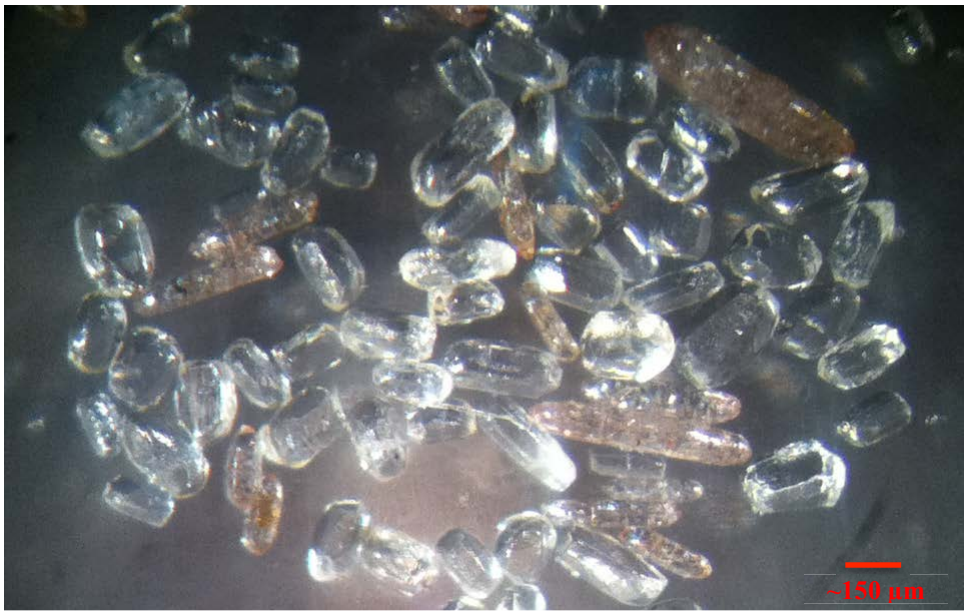

B

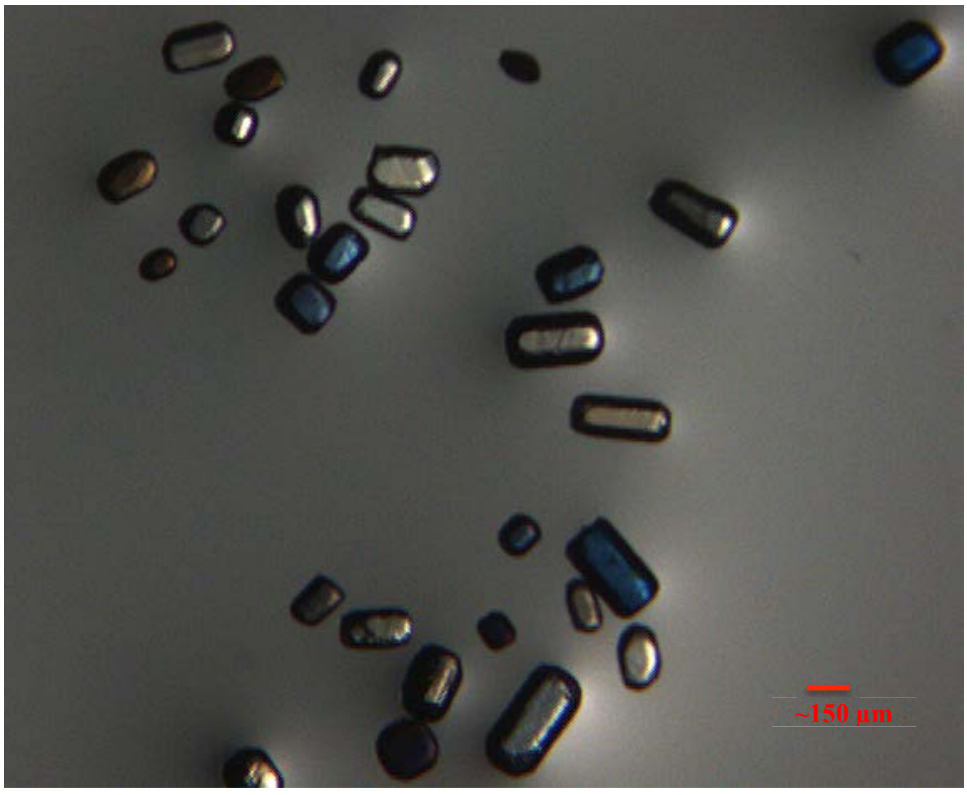

Figure 4.1. Apatite and zircon mineral separates from the samples. (A) Apatite and zircon grains from sample C053 (image under reflected light). (B) Apatite mineral separates from sample B106 (image under transmitted light). Most samples yielded high-quality, inclusion-free, large ($r \leq 60$ µm), subhedral to euhedral grains, which helped to appreciably reduce a portion of the uncertainty typically encountered in (U-Th-Sm)/He thermochronometry.

Table 1. Sample location and rock type. Upper box is vertical transect samples; middle box is coastline-perpendicular transect samples, ordered from northeast to southwest; lower box is coastline-parallel transect samples, ordered from North to South. Datum is WGS84. Sample field ID included the prefix "12MBC-"; however, this prefix is excluded herein for brevity.

SAMPLE # (12MBC-xxxx)	LATITUDE	LONGITUDE	ELEVATION (m)	Lithology
C016	63.81690000	-65.35660000	794.2	biotite granite
C008	63.80750000	-65.32800000	685.1	magnetite granite
C010	63.80960000	-65.31900000	561.9	biotite granite
C012	63.81150000	-65.31680000	431.1	biotite granite
C013	63.81210000	-65.31640000	375.0	biotite granite
C014	63.81280000	-65.31430000	311.0	biotite granite
C015	63.81440000	-65.31260000	225.9	biotite granite
C053	63.81450000	-65.31133000	183.5	biotite granite
C068	63.80974000	-65.30544000	114.0	biotite granite
C069	63.81014000	-65.30151000	35.1	biotite granite
B098	63.83240326	-64.31572883	222.4	biotite tonalite
B099	63.80506994	-64.59974202	252.0	biotite tonalite
B100	63.78999827	-64.65662533	244.3	biotite hornblende diorite
B101	63.77476661	-64.72326863	269.9	biotite tonalite
B102	63.77858994	-64.77428528	246.6	biotite diorite
B103	63.75847161	-64.85916357	243.0	monzogranite
B105	63.75529162	-64.91133354	236.0	biotite tonalite
B106	63.70989162	-65.06324514	249.8	monzogranite
C001	63.69900000	-65.29080000	260.1	biotite tonalite
K105	63.64591497	-65.33533835	266.9	biotite tonalite
C003	63.59340000	-65.65620000	326.5	biotite granite
C005	63.53770000	-66.00630000	397.0	granitic pegmatite
C007	63.41400000	-66.51410000	242.7	biotite monzogranite
C027	63.25268000	-64.51698000	0.0	biotite tonalite
C028	63.40376000	-64.49870000	5.0	biotite tonalite
C031	63.64214000	-64.48868000	3.0	biotite tonalite
C033	63.83968000	-64.51273000	18.0	biotite granite
Y080	62.91908834	-64.72139206	12.9	magnetite monzogranite

Table 2a. Reduced AHe data.

Sample	mineral	Sample Transect	Age (Ma)	Uncorr. Age (Ma)	2σ error (Ma)	U (ppm)	Th (ppm)	147Sm (ppm)	eU (ppm)	Th/U	[He] (nmol/g)	{He} (nmol/g)	Mass (ug)	Ft	ESR (μm)	Elev. (m)	[He]:eU	{He}:eU
C016-1	apatite	vertical	201.6	163.2	12.1	2.15	0.17	9.28	2.23	0.08	2.02	2.49	11.16	0.81	77.35	794	0.89	1.09
C016-2	apatite	vertical	164.6	135.4	9.9	1.45	0.52	6.07	1.60	0.36	1.20	1.46	16.00	0.82	85.80	794	0.73	0.89
C016-3	apatite	vertical	210.7	153.7	12.6	4.02	0.46	13.70	4.19	0.11	3.56	4.88	4.78	0.73	53.44	794	0.83	1.14
C016-4	apatite	vertical	221.3	179.6	13.3	2.64	0.25	7.77	2.74	0.10	2.72	3.35	12.60	0.81	78.58	794	0.98	1.21
C016-5	apatite	vertical	233.9	188.9	14.0	3.33	0.25	9.63	3.43	0.07	3.59	4.44	11.69	0.81	76.68	794	1.03	1.28
C008-1	apatite	vertical	482.1	370.3	28.9	4.55	5.14	23.91	5.86	1.13	12.28	15.99	7.60	0.77	67.05	685	2.05	2.67
C008-2	apatite	vertical	356.3	267.7	21.4	1.68	1.09	14.28	2.00	0.65	3.03	4.03	5.46	0.75	60.98	685	1.46	1.94
C008-3	apatite	vertical	269.5	219.8	16.2	0.97	0.40	10.42	1.11	0.41	1.39	1.70	13.42	0.82	82.72	685	1.19	1.46
C008-4	apatite	vertical	469.6	344.3	28.2	4.09	2.85	20.43	4.85	0.70	9.44	12.87	4.72	0.73	56.67	685	1.90	2.60
C008-5	apatite	vertical	224.2	181.0	13.5	1.04	0.53	9.71	1.22	0.51	1.24	1.53	11.98	0.81	79.41	685	0.98	1.21
C010-1	apatite	vertical	357.8	276.0	21.5	3.26	2.19	21.63	3.87	0.67	6.02	7.81	8.20	0.77	66.84	562	1.51	1.96
C010-2	apatite	vertical	280.0	222.0	16.8	1.73	1.11	20.16	2.08	0.64	2.63	3.31	10.10	0.79	74.15	562	1.20	1.51
C010-3	apatite	vertical	755.0	516.5	45.3	6.52	12.21	51.20	9.58	1.87	28.48	41.64	3.34	0.68	48.67	562	2.89	4.23
C010-4	apatite	vertical	436.8	302.7	26.2	1.23	1.23	12.43	1.58	0.99	2.72	3.92	3.55	0.69	49.16	562	1.65	2.39
C010-5	apatite	vertical	565.8	451.8	33.9	2.89	1.14	22.26	3.26	0.39	8.48	10.62	10.35	0.80	75.24	562	2.51	3.14
C012-1	apatite	vertical	278.9	224.8	16.7	2.18	1.00	17.48	2.50	0.46	3.17	3.93	11.83	0.81	78.77	431	1.22	1.51
C012-2	apatite	vertical	286.3	220.6	17.2	1.86	0.97	21.50	2.19	0.52	2.74	3.55	6.82	0.77	66.10	431	1.19	1.55
C012-3	apatite	vertical	386.3	308.1	23.2	1.78	0.80	12.84	2.03	0.45	3.54	4.44	9.44	0.80	75.10	431	1.69	2.12
C012-4	apatite	vertical	521.6	381.6	31.3	6.07	2.60	39.05	6.86	0.43	14.91	20.38	4.75	0.73	55.39	431	2.11	2.88
C012-5	apatite	vertical	523.8	415.9	31.4	6.27	3.53	41.97	7.29	0.56	17.33	21.82	11.65	0.79	74.34	431	2.31	2.91
C013-1	apatite	vertical	395.2	285.9	23.7	9.31	4.07	52.46	10.52	0.44	16.93	23.40	4.09	0.72	53.69	375	1.57	2.17
C013-2	apatite	vertical	513.7	337.5	30.8	20.21	33.10	98.63	28.32	1.64	53.89	82.02	2.55	0.66	44.21	375	1.87	2.84
C013-3	apatite	vertical	328.1	234.5	19.7	16.67	8.50	105.22	19.15	0.51	25.21	35.27	3.64	0.71	52.14	375	1.28	1.79
C013-4	apatite	vertical	439.6	294.9	26.4	6.86	3.30	49.67	7.87	0.48	13.13	19.58	2.21	0.67	44.42	375	1.61	2.41
C013-5	apatite	vertical	335.7	231.3	20.1	2.54	1.63	17.64	3.01	0.64	3.91	5.67	2.64	0.69	47.74	375	1.26	1.83

Table 2b. Reduced AHe data.

Sample	mineral	Sample Transect	Age (Ma)	Uncorr. Age (Ma)	2σ error (Ma)	U (ppm)	Th (ppm)	147Sm (ppm)	eU (ppm)	Th/U	[He] (nmol/g)	{He} (nmol/g)	Mass (ug)	Ft	ESR (μm)	Elev. (m)	[He]:eU	{He}:eU
C014-1	apatite	vertical	257.4	202.1	15.4	1.66	2.23	13.79	2.24	1.34	2.54	3.24	9.34	0.78	73.09	311	1.10	1.40
C014-2	apatite	vertical	601.0	421.8	36.1	2.09	10.28	17.62	4.55	4.92	10.89	15.52	3.64	0.70	53.16	311	2.35	3.35
C014-3	apatite	vertical	456.8	313.8	27.4	1.02	1.75	10.95	1.48	1.72	2.64	3.84	3.25	0.69	49.05	311	1.72	2.50
C014-4	apatite	vertical	614.3	416.6	36.9	2.05	2.63	18.81	2.75	1.28	6.58	9.70	2.86	0.68	47.07	311	2.30	3.40
C014-5	apatite	vertical	420.5	263.9	25.2	2.07	5.42	23.27	3.44	2.61	5.14	8.18	2.08	0.63	40.87	311	1.44	2.30
C015-1	apatite	vertical	173.3	108.8	10.4	1.08	1.35	13.10	1.45	1.26	0.89	1.42	1.61	0.63	39.96	226	0.58	0.93
C015-2	apatite	vertical	414.6	296.4	24.9	4.36	2.04	18.26	4.92	0.47	8.19	11.46	3.29	0.72	52.05	226	1.63	2.28
C015-3	apatite	vertical	843.2	549.9	50.6	2.37	3.13	17.54	3.18	1.32	10.11	15.50	1.85	0.65	43.22	226	3.09	4.74
C015-4	apatite	vertical	372.1	291.3	22.3	1.36	0.93	12.87	1.64	0.68	2.71	3.46	8.66	0.78	70.66	226	1.59	2.03
C015-5	apatite	vertical	574.2	433.3	34.5	5.67	3.44	22.91	6.58	0.61	16.21	21.48	5.94	0.75	61.75	226	2.42	3.21
C053-1	apatite	vertical	619.4	433.1	37.2	1.50	4.59	15.63	2.63	3.07	6.52	9.33	3.43	0.70	52.09	184	2.40	3.44
C053-2	apatite	vertical	499.3	390.0	30.0	2.38	2.52	25.14	3.09	1.06	6.91	8.85	9.14	0.78	71.14	184	2.15	2.75
C053-3	apatite	vertical	454.3	340.8	27.3	1.74	1.33	17.48	2.13	0.76	4.15	5.54	5.66	0.75	61.00	184	1.87	2.49
C053-4	apatite	vertical	740.4	561.5	44.4	1.86	2.13	14.80	2.43	1.15	7.90	10.42	6.41	0.76	64.15	184	3.15	4.16
C053-5	apatite	vertical	168.5	102.9	10.1	0.99	1.64	17.88	1.46	1.65	0.85	1.40	1.58	0.61	38.30	184	0.55	0.90
C068-1	apatite	vertical	593.1	460.3	35.6	6.53	2.86	26.23	7.32	0.44	19.22	24.77	7.48	0.78	67.40	114	2.58	3.32
C068-2	apatite	vertical	603.5	465.5	36.2	6.77	3.10	27.05	7.62	0.46	20.25	26.26	7.27	0.77	66.00	114	2.61	3.38
C068-3	apatite	vertical	309.9	223.2	18.6	7.06	5.60	31.93	8.51	0.79	10.59	14.71	3.94	0.72	54.01	114	1.22	1.70
C068-4	apatite	vertical	276.7	184.8	16.6	1.80	1.46	14.44	2.21	0.81	2.29	3.43	2.34	0.67	44.74	114	1.00	1.50
C068-5	apatite	vertical	407.2	295.3	24.4	3.31	2.03	24.05	3.90	0.61	6.51	8.97	3.88	0.73	54.62	114	1.62	2.23
C069-1	apatite	vertical	167.7	127.1	10.1	5.68	0.28	28.47	5.89	0.05	4.14	5.47	7.14	0.76	59.63	35	0.69	0.91
C069-2	apatite	vertical	75.2	59.1	4.5	3.32	0.20	12.35	3.43	0.06	1.11	1.41	8.74	0.79	68.18	35	0.32	0.40
C069-3	apatite	vertical	283.3	230.0	17.0	6.69	0.17	19.53	6.83	0.03	8.73	10.75	11.78	0.81	78.03	35	1.26	1.55
C069-4	apatite	vertical	200.6	159.7	12.0	6.10	0.31	21.97	6.28	0.05	5.54	6.96	9.94	0.80	71.88	35	0.87	1.09
C069-5	apatite	vertical	242.4	187.9	14.5	7.57	0.30	26.86	7.78	0.04	8.10	10.45	7.79	0.78	64.59	35	1.02	1.32

Table 2c. Reduced AHe data.

Sample	mineral	Sample Transect	Age (Ma)	Uncorr. Age (Ma)	2σ error (Ma)	U (ppm)	Th (ppm)	147Sm (ppm)	eU (ppm)	Th/U	[He] (nmol/g)	{He} (nmol/g)	Mass (ug)	Ft	ESR (μm)	Elev. (m)	[He]:eU	{He}:eU
B098-1	apatite	perpendicular	358.7	287.6	21.5	18.74	0.52	7.68	18.90	0.03	30.17	37.63	9.79	0.80	73.75	222	1.59	1.99
B098-2	apatite	perpendicular	582.7	463.1	35.0	23.61	0.60	14.80	23.82	0.03	62.51	78.66	9.80	0.79	71.06	222	2.62	3.29
B098-3	apatite	perpendicular	332.7	230.2	20.0	9.63	0.70	4.66	9.81	0.07	12.46	18.01	2.45	0.69	46.06	222	1.27	1.83
B098-4	apatite	perpendicular	408.5	315.8	24.5	10.41	0.38	5.28	10.53	0.04	18.51	23.95	6.23	0.77	63.90	222	1.75	2.27
B098-5	apatite	perpendicular	449.4	363.1	27.0	22.94	0.46	10.11	23.10	0.02	46.95	58.10	12.78	0.81	76.21	222	2.03	2.51
B099-1	apatite	perpendicular	373.7	323.7	22.4	23.95	1.95	23.64	24.52	0.08	44.30	51.14	30.89	0.87	112.18	252	1.80	2.08
B099-2	apatite	perpendicular	334.8	269.7	20.1	17.86	1.36	25.68	18.30	0.08	27.43	34.05	10.69	0.81	75.77	252	1.49	1.85
B099-3	apatite	perpendicular	319.6	271.1	19.2	19.65	1.54	14.17	20.07	0.08	30.18	35.58	22.25	0.85	98.36	252	1.50	1.77
B099-4	apatite	perpendicular	412.5	339.8	24.8	23.33	2.19	18.46	23.92	0.09	45.42	55.15	14.14	0.82	84.16	252	1.89	2.30
B099-5	apatite	perpendicular	369.2	290.4	22.2	20.22	2.30	14.58	20.82	0.11	33.60	42.72	8.37	0.79	68.93	252	1.61	2.04
B100-1	apatite	perpendicular	332.5	247.0	20.0	13.71	3.40	6.28	14.52	0.25	19.83	26.70	5.10	0.74	57.21	244	1.36	1.83
B100-2	apatite	perpendicular	327.8	217.3	19.7	25.98	4.76	9.86	27.12	0.18	32.48	48.99	2.38	0.66	42.21	244	1.20	1.80
B100-3	apatite	perpendicular	362.8	274.0	21.8	25.21	4.77	9.60	26.36	0.19	40.04	53.01	6.41	0.76	60.01	244	1.52	2.01
B100-4	apatite	perpendicular	375.7	307.5	22.5	25.00	5.54	16.23	26.36	0.22	45.12	55.13	16.89	0.82	82.76	244	1.71	2.08
B100-5	apatite	perpendicular	313.5	229.4	18.8	17.06	3.31	16.26	17.90	0.19	22.69	31.02	4.90	0.73	54.34	244	1.26	1.72
B101-1	apatite	perpendicular	371.4	284.3	22.3	25.52	4.01	19.01	26.54	0.16	41.90	54.75	7.27	0.77	62.57	270	1.57	2.06
B101-2	apatite	perpendicular	367.8	286.2	22.1	32.42	7.83	29.89	34.38	0.24	54.70	70.29	7.51	0.78	67.04	270	1.58	2.04
B101-3	apatite	perpendicular	303.4	228.0	18.2	17.81	3.45	5.82	18.63	0.19	23.43	31.19	5.91	0.75	59.03	270	1.26	1.67
B101-4	apatite	perpendicular	455.0	357.0	27.3	25.91	4.83	16.28	27.10	0.19	54.14	69.01	8.07	0.78	68.78	270	1.99	2.54
B101-5	apatite	perpendicular	348.7	273.7	20.9	17.78	3.09	14.49	18.56	0.17	28.19	35.92	7.99	0.78	68.83	270	1.51	1.93
B102-1	apatite	perpendicular	238.8	185.9	14.3	26.80	1.03	11.07	27.09	0.04	27.66	35.52	6.76	0.78	65.62	247	1.02	1.31
B102-2	apatite	perpendicular	222.4	165.8	13.3	20.46	1.63	14.75	20.91	0.08	19.02	25.51	4.88	0.75	56.81	247	0.91	1.22
B102-3	apatite	perpendicular	278.1	208.3	16.7	17.55	1.40	18.85	17.97	0.08	20.64	27.55	5.63	0.75	57.73	247	1.14	1.53
B102-4	apatite	perpendicular	232.1	182.6	13.9	17.02	1.66	6.48	17.43	0.10	17.48	22.21	8.22	0.79	68.95	247	1.00	1.27
B102-5	apatite	perpendicular	253.6	202.5	15.2	18.11	1.37	7.04	18.47	0.08	20.56	25.76	9.33	0.80	72.83	247	1.11	1.39

Table 2d. Reduced AHe data.

Sample	mineral	Sample Transect	Age (Ma)	Uncorr. Age (Ma)	2σ error (Ma)	U (ppm)	Th (ppm)	147Sm (ppm)	eU (ppm)	Th/U	[He] (nmol/g)	{He} (nmol/g)	Mass (ug)	Ft	ESR (µm)	Elev. (m)	[He]:eU	{He}:eU
B103-1	apatite	perpendicular	842.9	543.9	50.6	86.69	114.53	68.83	113.40	1.32	351.60	544.85	2.05	0.65	42.27	243	3.09	4.79
B103-2	apatite	perpendicular	630.3	463.5	37.8	45.53	54.82	52.78	58.41	1.20	153.27	208.42	4.80	0.74	58.26	243	2.61	3.55
B103-3	apatite	perpendicular	523.8	380.9	31.4	45.53	53.93	59.36	58.24	1.18	124.63	171.41	4.16	0.73	56.31	243	2.13	2.93
B103-4	apatite	perpendicular	406.7	280.2	24.4	30.33	28.14	36.29	36.99	0.93	57.66	83.70	2.58	0.69	48.36	243	1.55	2.25
B103-5	apatite	perpendicular	556.5	387.5	33.4	58.08	56.53	46.25	71.33	0.97	155.21	222.90	2.97	0.70	49.74	243	2.17	3.11
B105-1	apatite	perpendicular	307.3	242.9	18.4	12.44	2.11	5.46	12.95	0.17	17.38	21.99	9.14	0.79	70.66	236	1.34	1.69
B105-2	apatite	perpendicular	451.8	359.6	27.1	21.26	6.60	14.72	22.85	0.31	46.00	57.80	9.30	0.80	73.70	236	2.01	2.52
B105-3	apatite	perpendicular	526.8	440.3	31.6	46.41	18.43	30.23	50.81	0.40	126.32	151.16	20.07	0.84	93.32	236	2.48	2.97
B105-4	apatite	perpendicular	395.8	318.4	23.7	23.60	4.68	14.09	24.74	0.20	43.90	54.57	9.64	0.80	76.32	236	1.77	2.20
B105-5	apatite	perpendicular	522.8	419.4	31.4	47.17	14.91	18.87	50.70	0.32	119.72	149.25	10.54	0.80	76.22	236	2.36	2.94
B106-1	apatite	perpendicular	250.7	194.1	15.0	23.68	44.67	88.99	34.41	1.89	37.13	47.95	7.98	0.77	70.20	250	1.06	1.37
B106-2	apatite	perpendicular	302.9	224.5	18.2	35.11	74.95	95.28	52.84	2.13	65.99	89.01	5.42	0.74	60.85	250	1.24	1.67
B106-3	apatite	perpendicular	269.9	188.7	16.2	29.92	71.31	96.60	46.82	2.38	49.06	70.18	3.15	0.70	51.73	250	1.04	1.48
B106-4	apatite	perpendicular	319.5	228.5	19.2	50.65	90.11	122.92	72.01	1.78	91.48	127.91	4.86	0.72	54.48	250	1.26	1.76
B106-5	apatite	perpendicular	270.9	196.4	16.3	20.32	53.25	70.52	32.93	2.62	35.96	49.60	4.39	0.73	57.26	250	1.08	1.49
K105-1	apatite	perpendicular	206.6	159.5	12.4	4.73	0.36	38.98	5.01	0.08	4.48	5.80	6.37	0.77	63.99	267	0.86	1.11
K105-2	apatite	perpendicular	264.7	193.6	15.9	2.47	0.64	13.49	2.69	0.26	2.90	3.97	4.22	0.73	54.64	267	1.05	1.44
K105-3	apatite	perpendicular	235.4	169.5	14.1	7.39	1.51	12.83	7.80	0.20	7.28	10.11	3.84	0.72	51.99	267	0.93	1.29
K105-4	apatite	perpendicular	203.6	155.0	12.2	3.87	0.39	18.36	4.05	0.10	3.48	4.58	5.16	0.76	61.04	267	0.84	1.10
K105-5	apatite	perpendicular	190.7	140.3	11.4	2.38	0.74	7.44	2.58	0.31	2.00	2.72	4.01	0.74	55.85	267	0.76	1.04
C001-1	apatite	perpendicular	271.1	196.8	16.3	8.29	1.12	23.07	8.66	0.13	9.44	13.01	4.03	0.73	52.75	260	1.07	1.48
C001-2	apatite	perpendicular	196.5	145.8	11.8	7.89	3.04	17.24	8.67	0.39	6.96	9.38	5.47	0.74	57.68	260	0.79	1.07
C001-3	apatite	perpendicular	300.0	205.1	18.0	8.20	2.06	25.66	8.80	0.25	10.02	14.65	2.82	0.68	45.60	260	1.12	1.64
C001-4	apatite	perpendicular	204.5	161.5	12.3	6.39	0.80	19.44	6.67	0.12	5.95	7.53	9.00	0.79	70.01	260	0.88	1.11
C001-5	apatite	perpendicular	213.9	155.6	12.8	9.89	1.68	30.23	10.42	0.17	8.95	12.31	3.68	0.73	53.24	260	0.85	1.16

Table 2e. Reduced AHe data.

Sample	mineral	Sample Transect	Age (Ma)	Uncorr. Age (Ma)	2σ error (Ma)	U (ppm)	Th (ppm)	147Sm (ppm)	eU (ppm)	Th/U	[He] (nmol/g)	{He} (nmol/g)	Mass (ug)	Ft	ESR (µm)	Elev. (m)	[He]:eU	{He}:eU
C003-1	apatite	perpendicular	309.7	215.7	18.6	6.96	0.91	24.37	7.29	0.13	8.74	12.55	3.32	0.70	47.15	327	1.18	1.69
C003-2	apatite	perpendicular	312.3	203.0	18.7	3.84	1.01	8.24	4.12	0.26	4.62	7.11	1.75	0.65	40.79	327	1.11	1.71
C003-3	apatite	perpendicular	305.8	205.2	18.3	4.06	1.86	14.00	4.56	0.46	5.20	7.75	2.73	0.67	44.39	327	1.12	1.67
C003-4	apatite	perpendicular	308.0	205.4	18.5	4.84	0.83	17.51	5.12	0.17	5.84	8.76	2.05	0.67	42.70	327	1.12	1.68
C003-5	apatite	perpendicular	278.1	206.8	16.7	3.78	0.56	18.61	4.00	0.15	4.61	6.20	4.89	0.74	56.77	327	1.13	1.51
C005-1	apatite	perpendicular	331.8	240.8	19.9	118.64	17.55	85.86	123.11	0.15	163.92	225.81	3.57	0.73	52.85	397	1.33	1.83
C005-2	apatite	perpendicular	348.0	285.1	20.9	122.62	8.94	100.34	125.18	0.07	198.24	242.01	14.52	0.82	81.75	397	1.58	1.93
C005-3	apatite	perpendicular	321.6	229.8	19.3	53.55	3.22	68.30	54.63	0.06	69.42	97.15	4.33	0.71	50.02	397	1.26	1.77
C005-4	apatite	perpendicular	468.4	315.3	28.1	2.33	1.90	16.12	2.85	0.81	5.08	7.55	2.38	0.67	45.54	397	1.73	2.57
C005-5	apatite	perpendicular	322.8	231.6	19.4	10.82	0.79	25.04	11.13	0.07	14.31	19.94	3.38	0.72	50.71	397	1.27	1.77
C007-1	apatite	perpendicular	406.5	249.8	24.4	3.52	2.07	136.43	4.68	0.59	7.04	11.45	1.36	0.61	37.41	243	1.30	2.12
C007-2	apatite	perpendicular	1077.9	804.1	64.7	0.90	0.59	82.28	1.44	0.65	7.81	10.47	5.53	0.75	59.64	243	4.16	5.58
C007-3	apatite	perpendicular	140.6	96.6	8.4	1.74	4.70	71.77	3.18	2.70	1.80	2.63	2.95	0.69	49.74	243	0.51	0.74
C007-4	apatite	perpendicular	744.3	589.2	44.7	1.61	0.54	64.43	2.06	0.33	7.56	9.54	9.03	0.79	72.25	243	3.15	3.98
C007-5	apatite	perpendicular	353.3	261.5	21.2	2.19	1.38	87.62	2.95	0.63	4.65	6.29	4.75	0.74	58.12	243	1.36	1.84
C028-1	apatite	parallel	274.4	201.6	16.5	11.17	13.93	19.56	14.48	1.25	16.16	21.99	5.34	0.73	58.14	5	1.11	1.51
C028-2	apatite	parallel	184.7	127.4	11.1	6.19	6.95	17.80	7.88	1.12	5.54	8.02	2.97	0.69	48.86	5	0.69	1.01
C028-3	apatite	parallel	323.5	224.2	19.4	10.23	12.42	19.75	13.19	1.21	16.41	23.67	3.05	0.69	49.54	5	1.23	1.78
C028-4	apatite	parallel	162.1	103.4	9.7	4.53	8.21	7.87	6.46	1.81	3.67	5.75	1.84	0.64	41.74	5	0.56	0.89
C028-5	apatite	parallel	211.7	148.5	12.7	4.90	5.40	11.95	6.20	1.10	5.08	7.25	3.45	0.70	50.94	5	0.81	1.16
C027-1	apatite	parallel	417.8	321.5	25.1	5.00	0.52	21.41	5.23	0.10	9.47	12.30	6.46	0.77	63.46	0	1.77	2.30
C027-2	apatite	parallel	224.3	163.9	13.5	7.05	1.54	34.54	7.57	0.22	6.89	9.43	4.16	0.73	54.30	0	0.89	1.22
C027-3	apatite	parallel	692.1	536.4	41.5	10.71	0.82	42.84	11.11	0.08	34.38	44.35	7.51	0.78	64.88	0	3.03	3.91
C027-4	apatite	parallel	444.1	337.3	26.6	4.49	0.74	26.41	4.80	0.16	9.16	12.07	5.53	0.76	61.01	0	1.86	2.45
C027-5	apatite	parallel	935.5	716.9	56.1	7.62	3.72	19.70	8.57	0.49	36.03	47.02	6.79	0.77	64.64	0	4.15	5.42

Table 2f. Reduced AHe and ZHe data.

Sample	mineral	Sample Transect	Age (Ma)	Uncorr. Age (Ma)	2σ error (Ma)	U (ppm)	Th (ppm)	147Sm (ppm)	eU (ppm)	Th/U	[He] (nmol/g)	{He} (nmol/g)	Mass (ug)	Ft	ESR (µm)	Elev. (m)	[He]:eU	{He}:eU
Y080-1	apatite	parallel	193.4	147.7	11.6	4.68	0.83	28.93	5.02	0.18	4.13	5.40	6.24	0.76	62.22	13	0.80	1.04
Y080-2	apatite	parallel	223.0	183.7	13.4	3.70	0.44	34.47	3.97	0.12	4.11	4.99	14.51	0.82	84.57	13	0.99	1.20
Y080-3	apatite	parallel	54.0	42.8	3.2	2.94	28.79	31.12	9.73	9.78	2.32	2.92	11.61	0.79	79.73	13	0.23	0.30
Y080-4	apatite	parallel	214.0	162.4	12.8	4.54	0.72	40.61	4.91	0.16	4.47	5.90	5.07	0.76	60.75	13	0.87	1.15
Y080-5	apatite	parallel	243.0	192.3	14.6	16.58	0.46	11.75	16.74	0.03	17.71	22.37	8.92	0.79	69.95	13	1.05	1.33
zB098-1	zircon	perpendicular	1049.1	790.2	62.9	143.56	29.98	1.37	150.47	0.21	701.94	931.89	5.75	0.75	46.50	222	4.66	6.19
zB098-2	zircon	perpendicular	1005.4	767.2	60.3	113.27	10.30	1.36	115.65	0.09	522.66	684.95	6.06	0.76	48.09	222	4.52	5.92
zB098-3	zircon	perpendicular	326.9	255.0	19.6	379.22	406.55	105.17	473.34	1.07	668.61	857.22	10.80	0.78	54.81	222	1.41	1.81
zB098-4	zircon	perpendicular	1066.6	789.1	64.0	105.86	15.81	1.42	109.50	0.15	510.40	689.88	4.53	0.74	43.65	222	4.66	6.30
zB098-5	zircon	perpendicular	1006.1	761.0	60.4	142.76	31.12	1.64	149.93	0.22	670.59	886.63	5.99	0.76	47.18	222	4.47	5.91
zC001-1	zircon	perpendicular	684.1	538.0	41.0	192.58	27.54	2.39	198.93	0.14	610.72	776.59	8.45	0.79	54.08	260	3.07	3.90
zC001-2	zircon	perpendicular	800.0	619.2	48.0	195.95	48.38	9.89	207.14	0.25	739.16	955.10	6.46	0.77	51.29	260	3.57	4.61
zC001-3	zircon	perpendicular	439.6	349.8	26.4	298.07	39.88	11.59	307.31	0.13	600.12	754.12	9.72	0.80	56.70	260	1.95	2.45
zC001-4	zircon	perpendicular	451.0	344.7	27.1	423.01	19.74	5.31	427.58	0.05	822.11	1075.73	5.41	0.76	48.12	260	1.92	2.52
zC001-5	zircon	perpendicular	395.3	307.8	23.7	261.01	73.67	13.08	278.03	0.28	475.70	610.82	8.07	0.78	52.65	260	1.71	2.20
zC008-1	zircon	vertical	1132.3	886.7	67.9	106.30	57.26	1.62	119.49	0.54	632.09	807.22	10.65	0.78	54.59	685	5.29	6.76
zC008-2	zircon	vertical	754.5	646.8	45.3	54.72	30.55	1.86	61.76	0.56	230.60	269.03	35.82	0.86	85.12	685	3.73	4.36
zC008-3	zircon	vertical	1023.8	792.9	61.4	89.77	49.53	1.39	101.18	0.55	472.15	609.61	7.96	0.77	52.40	685	4.67	6.02
zC008-4	zircon	vertical	1021.4	876.6	61.3	88.44	44.80	1.52	98.76	0.51	515.93	601.15	37.60	0.86	85.59	685	5.22	6.09
zC008-5	zircon	vertical	974.0	817.2	58.4	68.39	37.59	0.89	77.05	0.55	371.81	443.14	27.64	0.84	75.05	685	4.83	5.75
zC053-1	zircon	vertical	1229.1	971.1	73.7	68.90	41.90	0.90	78.55	0.61	460.61	583.03	8.69	0.79	56.73	184	5.86	7.42
zC053-2	zircon	vertical	939.9	753.7	56.4	83.24	66.13	1.62	98.47	0.79	433.58	540.70	14.64	0.80	60.82	184	4.40	5.49
zC053-3	zircon	vertical	945.7	734.5	56.7	91.02	52.43	1.18	103.09	0.58	442.02	569.11	8.30	0.78	53.01	184	4.29	5.52
zC053-4	zircon	vertical	1037.1	848.6	62.2	77.62	49.43	1.17	89.01	0.64	447.61	547.01	18.32	0.82	66.28	184	5.03	6.15
zC053-5	zircon	vertical	947.2	771.8	56.8	126.31	102.25	3.18	149.87	0.81	677.30	831.20	17.24	0.81	65.40	184	4.52	5.55

Table 2g. Reduced ZHe data.

Sample	mineral	Sample Transect	Age (Ma)	Uncorr. Age (Ma)	2σ error (Ma)	U (ppm)	Th (ppm)	147Sm (ppm)	eU (ppm)	Th/U	[He] (nmol/g)	{He} (nmol/g)	Mass (ug)	Ft	ESR (μm)	Elev. (m)	[He]:eU	{He}:eU
zC068-1	zircon	vertical	958.3	767.4	57.5	144.59	83.28	3.67	163.78	0.58	736.89	920.21	11.92	0.80	59.93	114	4.50	5.62
zC068-2	zircon	vertical	1015.6	801.8	60.9	134.39	80.14	2.34	152.85	0.60	721.86	914.35	11.09	0.79	56.54	114	4.72	5.98
zC068-3	zircon	vertical	949.0	759.9	56.9	94.08	66.32	2.06	109.36	0.70	486.20	607.24	14.77	0.80	60.22	114	4.45	5.55
zC068-4	zircon	vertical	983.6	772.2	59.0	86.78	51.19	2.98	98.58	0.59	446.53	568.81	8.87	0.79	55.27	114	4.53	5.77
zC068-5	zircon	vertical	921.5	740.7	55.3	96.65	47.06	1.22	107.49	0.49	465.49	579.09	11.41	0.80	60.66	114	4.33	5.39
zC069-1	zircon	vertical	1030.9	823.9	61.9	159.77	43.10	1.59	169.70	0.27	829.06	1037.35	12.23	0.80	58.38	35	4.89	6.11
zC069-2	zircon	vertical	869.7	746.7	52.2	105.33	32.52	1.22	112.83	0.31	493.69	575.07	34.55	0.86	84.77	35	4.38	5.10
zC069-3	zircon	vertical	860.4	723.3	51.6	105.79	39.47	2.17	114.88	0.37	485.14	577.10	22.27	0.84	75.14	35	4.22	5.02
zC069-4	zircon	vertical	829.4	696.4	49.8	136.91	30.92	2.35	144.04	0.23	584.14	695.77	18.71	0.84	73.86	35	4.05	4.83
zC069-5	zircon	vertical	868.1	735.1	52.1	99.79	25.13	1.21	105.58	0.25	454.36	536.54	23.38	0.85	77.71	35	4.30	5.08
zY080-1	zircon	parallel	662.2	548.7	39.7	224.56	58.55	7.13	238.07	0.26	746.09	900.52	18.21	0.83	69.02	13	3.13	3.78
zY080-2	zircon	parallel	791.7	616.6	47.5	168.40	43.15	2.33	178.35	0.26	633.53	813.40	9.08	0.78	52.57	13	3.55	4.56
zY080-3	zircon	parallel	414.7	337.3	24.9	288.33	56.77	22.33	301.51	0.20	567.06	697.07	13.55	0.81	62.82	13	1.88	2.31
zY080-4	zircon	parallel	630.4	501.9	37.8	314.87	91.59	12.89	336.01	0.29	957.74	1203.07	9.98	0.80	57.51	13	2.85	3.58
zY080-5	zircon	parallel	522.5	408.4	31.3	422.21	85.90	7.62	442.02	0.20	1014.18	1297.58	9.27	0.78	53.06	13	2.29	2.94

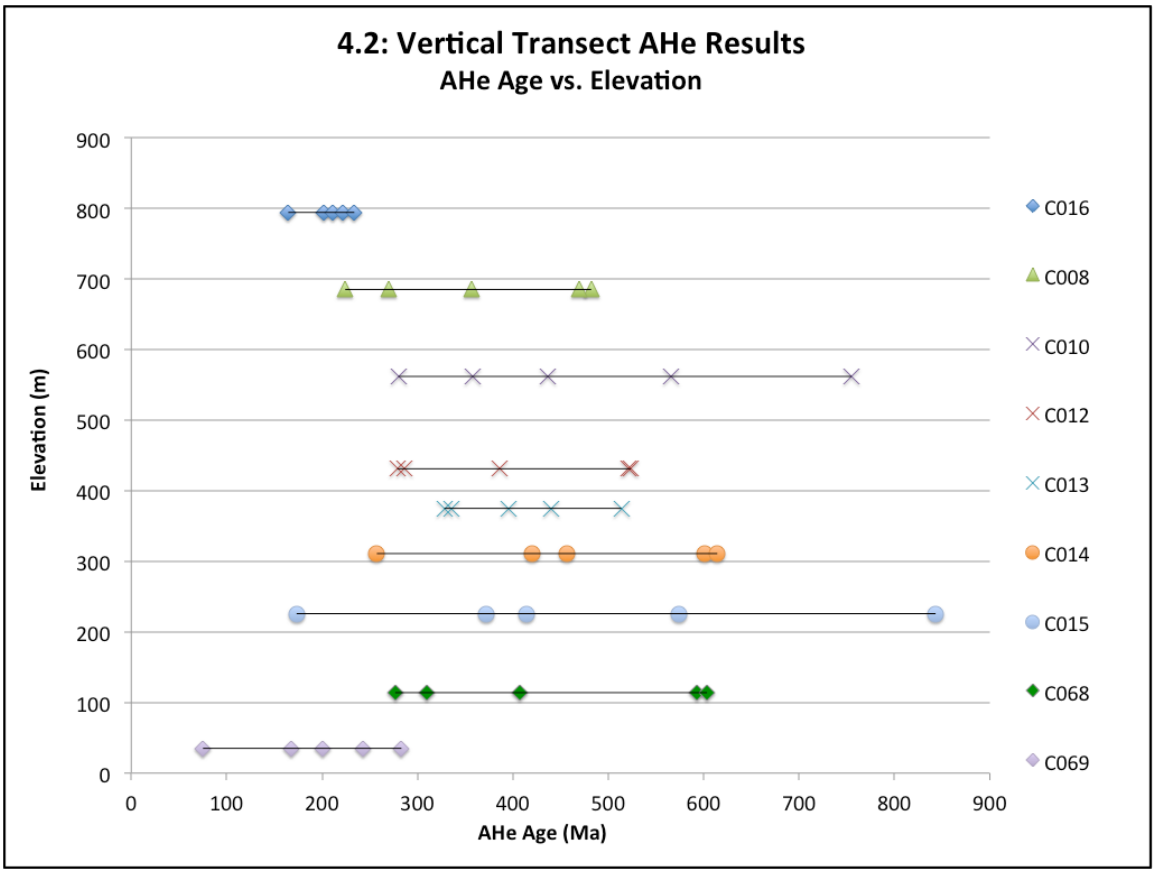

Figure 4.2. Results from AHe analyses on the vertical transect samples (see Fig. 3.1 for map). Each sample had five aliquots analyzed; aliquots presented with similar symbol and color are from the same sample. Grey line added to aid with clarity, indicating grains from the same sample.

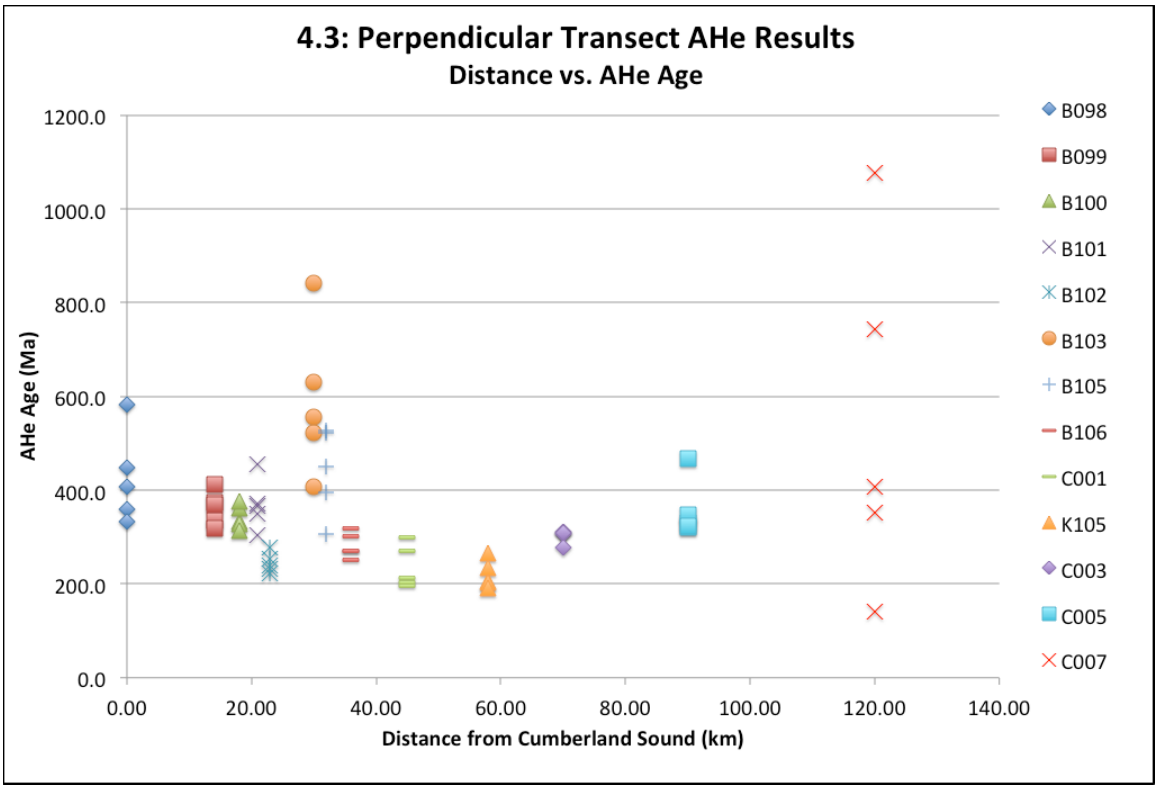

Figure 4.3. AHe results from the 250 m coastline-perpendicular transect samples (see Fig. 3.1 for map). Each sample had five aliquots analyzed; aliquots presented with similar symbol and color are from the same sample.

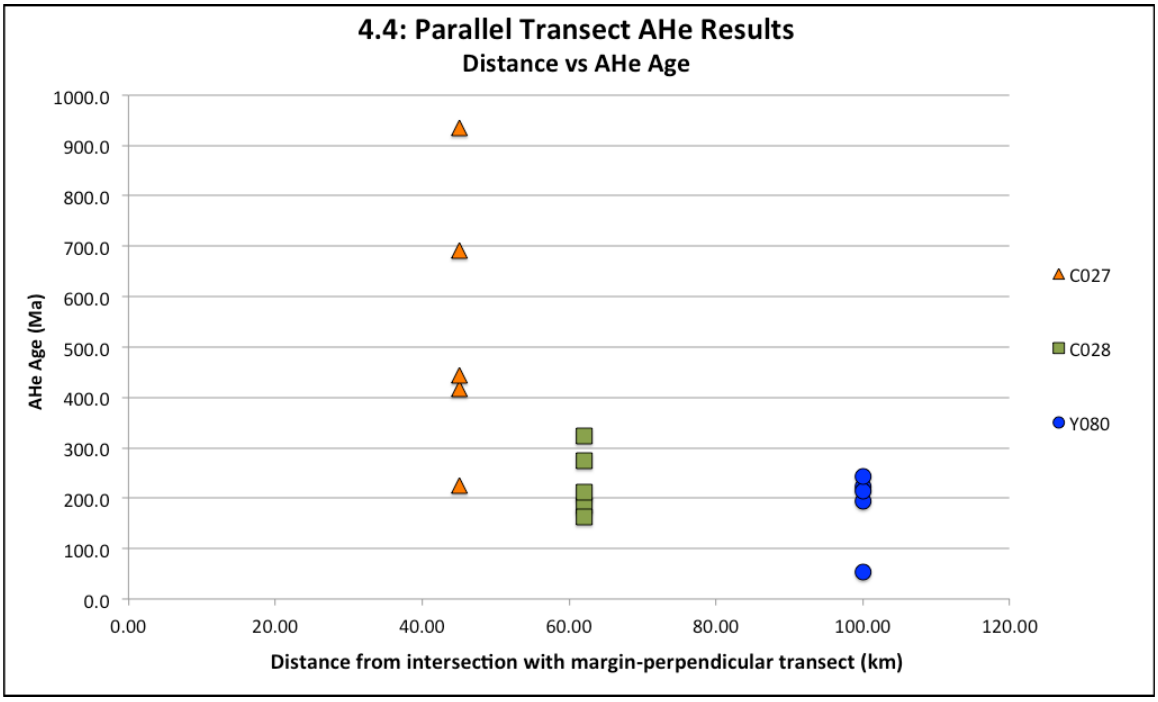

Figure 4.4. Results from AHe analyses on the sea-level coastline-parallel transect samples (see Fig. 3.1 for map). Each sample had five aliquots analyzed; aliquots presented with similar symbol and color are from the same sample.

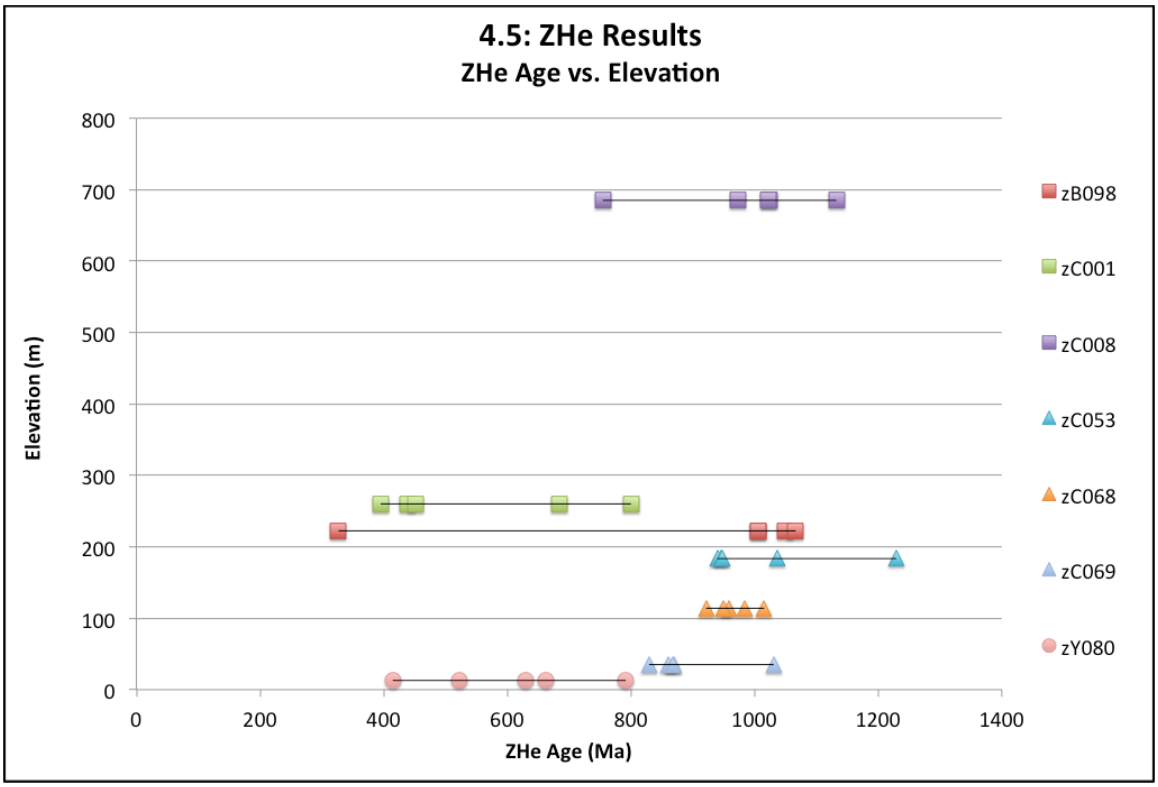

Figure 4.5. ZHe data from samples collected at various elevations from across Hall Peninsula. Samples zC008, zC053, zC068 and zC069 from vertical transect; zB098 and zC001 from the coastline-perpendicular transect; and zY080 from the coastline-parallel transect (see Fig. 3.1 for map). Each sample had five aliquots analyzed; aliquots presented with similar symbol and color are from the same sample.

4.2 Vertical Transect (AHe)

Samples from the vertical transect yield single-grain cooling ages ranging from 75–843 Ma (Fig 4.2). Many samples have highly dispersed aliquot ages, but not all samples display equal amounts of dispersion. Sample C015 has the highest range of measured grain ages, 173–843 Ma, while sample C016 (the highest elevation sample), has grain ages between 165–234 Ma (Fig. 4.2). All samples had low parent nuclide concentrations, or eU (the effective concentration of ^{4}He producers, where eU = U + .235*Th + .005*Sm), ranging from 1–8 ppm (with exception of sample C013, which ranged between 3–28 ppm) (Table 2a-b). No field relations or detectable differences between the samples were observed that would suggest a geological mechanism capable of producing the measured distribution of ages (e.g., a fault offsetting the transect, varying sample composition). Additionally, the vertical transect ages do not appear to include an exhumed apatite HePRZ, a characteristic feature of an episodic pulse of accelerated exhumation, which is in contrast to age data from the Torngat Mountains (see Centeno, 2005).

4.3 Perpendicular Transect (AHe)

Samples from the coastline-perpendicular transect have aliquot cooling ages between 141–1078 Ma (Fig 4.3; Table 2c-e). However, because sample C007 has the highest and lowest aliquot cooling ages, as well as other atypical qualities (discussed in Chapter 5), this sample was excluded from further data reduction/interpretation. By excluding C007, the range of AHe ages along the transect is 191–843 Ma, similar to that of the vertical transect. The range of measured eU concentrations from these samples span a much larger range than the other two transects, varying between 1–125 ppm, though several

samples have an eU range of 10–30 ppm (Table 2c-e). Particularly noteworthy is the lack of dispersion in samples B102, C003, and C005 (Fig. 4.3). In general, the mean ages provide no well-defined trend between cooling age and proximity to the coastline, precluding a simple characterization of the spatial variability of the exhumation across the peninsula and a straightforward connection to differential exhumation due to tilting of the Hall Peninsula half-graben.

4.4 Parallel transect (AHe)

Only 3 samples from the coastline-parallel transect were analyzed (Fig. 4.4; Table 2e-f). The aliquots in these samples exhibit different ranges of AHe ages (161 Ma in C028, versus 711 Ma in C027), despite having relatively similar, low eU concentrations (between 5–17 ppm). The goal of this transect was to detect a subtle difference among sample ages caused by topographic perturbations to the isotherms, and hence establish the timing of initial valley incision. However, considering the scattered results, it was decided the dispersion in the aliquot ages was too large to warrant further interpretation with regard to their intended purpose.

4.5 ZHe data

The 7 samples analyzed for ZHe were selected to be representative of the various transects; 4 are from the vertical transect, 2 from coast-perpendicular transect and 1 from the coast-parallel transect (Table 2f-g). Most samples displayed a substantial range of grain cooling ages, with the largest between 326–1067 Ma (sample zB098; Fig. 4.5). However, the single-grain ZHe ages in each sample scale directly with eU concentration, such that samples with large ranges of eU also yielded a large range of ZHe ages (e.g., zY080), and aliquots with similar eU values yielded comparable ZHe ages (e.g., zB098,

zC053). This prevents a simple interpretation of the data, because the highly scattered ZHe ages show no trend between cooling age and elevation (Fig. 4.5).

CHAPTER 5 – METHODOLOGICAL RESULTS: QUALITY ASSESSMENT AND INTERPRETATION OF (U-Th-Sm)/He DATA FROM RADIATION DAMAGED APATITE AND ZIRCON GRAINS

5.1 Factors that control a (U-Th-Sm)/He cooling age

As discussed in Chapter 3, the main factor controlling a (U-Th-Sm)/He age is the time the grain maintains a temperature below T_c, however many other factors can affect the measured age. Factors that control a ^{4}He age can be divided into two classes: first-order factors, which affect the entire sample, and second-order factors, which operate on individual grains. First-order factors relate to the thermal history of the entire rock sample (e.g., crystallization age, cooling rate, changes to geothermal gradient, elevation), as opposed to individual grains. On the other hand, second-order factors are variables that can introduce dispersion into the cooling ages of grain aliquots experiencing the same thermal history (e.g., grain geometry, eU concentration, grain chemistry). In particular, there are four second-order factors that are capable of introducing substantial dispersion in apatite and zircon (U-Th-Sm)/He data: 1) The presence of U- and Th-rich macro- and micro-scale fluid or mineral inclusions (Farley, 2002; Lippolt et al., 1994); 2) the validity of assumptions when correcting for alpha-particle ejection (Farley et al., 1996); 3) differences in grain size and geometry (Reiners and Farley, 2001); and 4) varying eU concentration (Shuster et al., 2006). In general, the influence of these factors on the measured AHe age tends to increase as cooling rate decreases. Similar effects are observed in ZHe cooling ages, and the relatively high U and Th concentrations in zircon (with respect to apatite) make the ZHe system especially vulnerable to these effects in a slowly cooling scenario. However, since AHe analyses comprise the majority of the data

in this study, this chapter focuses mainly on the influence of secondary controls on the AHe thermochronometer age data. The following sections describe the various tests implemented to assess the secondary controls on the individual cooling ages and weigh the contribution of each factor to the overall ^{4}He age dispersion (presented in increasing order of significance).

5.2 Fluid and mineral inclusions

The presence of U and Th rich macro- and micro-scale fluid or mineral inclusions (e.g., zircon and monazite) within apatite can result excess ^{4}He in the mineral grains. This 'parentless' ^{4}He is sourced from U and Th isotopes that may not dissolve completely and inhibit an accurate measurement of the parent isotope concentration, yielding an 'artificially' old ^{4}He age (Farley, 2002; Lippolt et al., 1994). To test for the presence of fluid and mineral inclusions, each grain was carefully inspected using a Nikon stereomicroscope with a rotating stage; grains were examined under both plane- and cross-polarized light, where the presence of any irregularity within the mineral (i.e., an inclusion) could be detected. All grains selected for analysis lacked any detectable irregularities, minimizing the probability that inclusions contributed to the scattered ^{4}He ages.

5.3 Alpha-ejection correction

Because the amount of ^{4}He present in the grain directly reflects its cooling history, any ^{4}He loss after the grain has cooled below T_c could lead to a misrepresentation of the cooling history. In instances where parent isotopes are located near a grain boundary, there is potential for ejection of alpha particles from the grain. This well-understood phenomenon is known as alpha-ejection, and its impact on the measured grain ages is a

function of the surface-to-volume (S/V) ratio of the grain (Farley et al., 1996). The alpha-ejection effect can be handled by applying a geometric correction to the total fraction of ^{4}He produced (i.e., an F_T correction) for each grain (Farley et al., 1996). Applying an F_T correction involves determining the probability that a parent isotope located within the alpha-stopping distance (~20 μm) of a grain boundary will emit an alpha particle in the direction of the boundary, and the likeliness that the particle will be ejected (Fig. 5.1A).

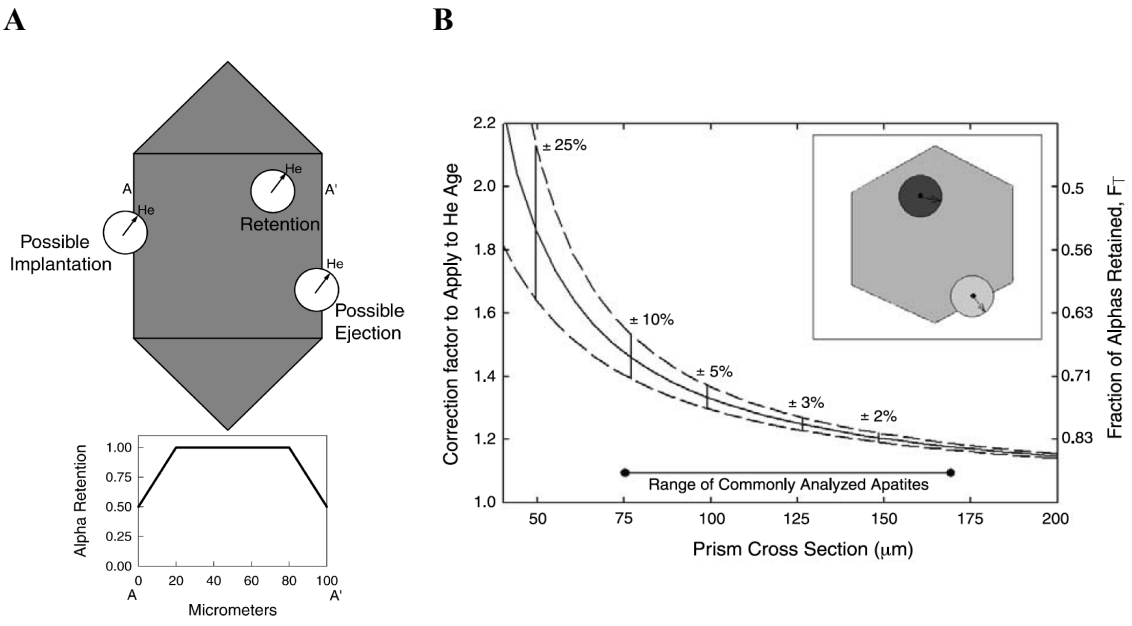

Figure 5.1. Alpha-ejection in apatite or zircon. (A) Three possible scenarios for production of an alpha particle: retention, ejection, and implantation. The center of the circle represents a U, Th or Sm nuclide, and the radius corresponds to the alpha-stopping distance, indicating the potential regions for the alpha particle to be emitted. Areas where the circle intersects the grain boundary indicate potential for alpha-ejection. Lower plot illustrates the change in likeliness of retention throughout the grain profile (from A to A'). From Farley (2002). (B) The relationship between grain size and FT correction, and the resultant correction factor applied to the measured He ages. Curve indicates the approximate factor multiplied by the raw He age to correct for ejected 4He, assuming an ideal grain geometry. Dashed curves show the 1σ uncertainty for the correction factor based on the grain measurement uncertainty and the suitability of the idealized grain geometry assumption for a typical grain. From Ehlers and Farley (2003).

The application of the F_T correction is widely accepted, however two key requirements must be satisfied to ensure a valid correction: the use of grains with a pristine (euhedral) geometry and minimum cross-section width greater than 60 μm, and a homogenous distribution of parent isotopes (Ehlers and Farley, 2003). For grains with a minimum dimension that is smaller than ~ 60μm, the F_T correction becomes increasingly large (Fig. 5.1B), and the associated uncertainty increases rapidly (Farley et al., 1996). This greatly increases the propensity for over-compensation of ejected ^{4}He in smaller grains. Similarly, an underlying assumption of the F_T-correction is the suitability of the surface-to-volume ratio of an idealized, euhedral grain (i.e., hexagonal dipyramidal or tetragonal dipyramidal for apatite or zircon, respectively) to represent that of subhedral measured grains. If this assumption is invalid, the F_T-correction will miscalculate the amount of ejected ^{4}He, resulting in erroneous, scattered aliquot ages. As previously indicated in Chapter 4 (Fig. 4.1), most of the samples analyzed in this study comprised large (min. dimension ≥ 80 μm), subhedral to euhedral grains, with many exhibiting dipyramidal crowns, thereby affirming the reliability of the F_T correction applied to the cooling ages.

A heterogeneous distribution of parent isotopes within the grain may also result in over- or under-compensation of ejected ^{4}He, depending on the relative distribution of isotopes within the core vs. grain boundary. The occurrence of a rim of highly concentrated U, Th and Sm near the grain boundary would result in a greater proportion of ^{4}He ejection, resulting in an underestimation of the required of F_T correction, while a U-Th-Sm poor outer rim in the grain would result in an overestimation of the F_T-corrected He age. To explore the possibility of chemical zonation affecting the F_T

correction, and potential spatial variations in ^{4}He diffusion character in the apatite grains (discussed further in section 5.5), a set of 12 samples were selected for electron microprobe (EMP) analysis (Robert Mackay EMP, Department of Earth Sciences, Dalhousie U.). Three grains from each sample were analyzed using 1) backscatter electron imaging, to create a relative compositional map; and 2) wavelength dispersive spectroscopy (WDS) point analyses, sampled as numerous transects across the a and c grain axes in order to qualitatively detect spatial variations in the trace-element abundance. The backscatter images revealed modest zonation in samples B105, C008, C053 and Y080 (Fig. 5.2), although no correlation between scattered AHe grain ages and zoning could be established. However, it should be noted that the extremely low eU concentrations (eU < 10 ppm) of several samples meant that many grains were near (or below) the detectable limit of U, Th, and Sm with the EMP, preventing a direct, quantitative comparison between the WDS results for each sample.

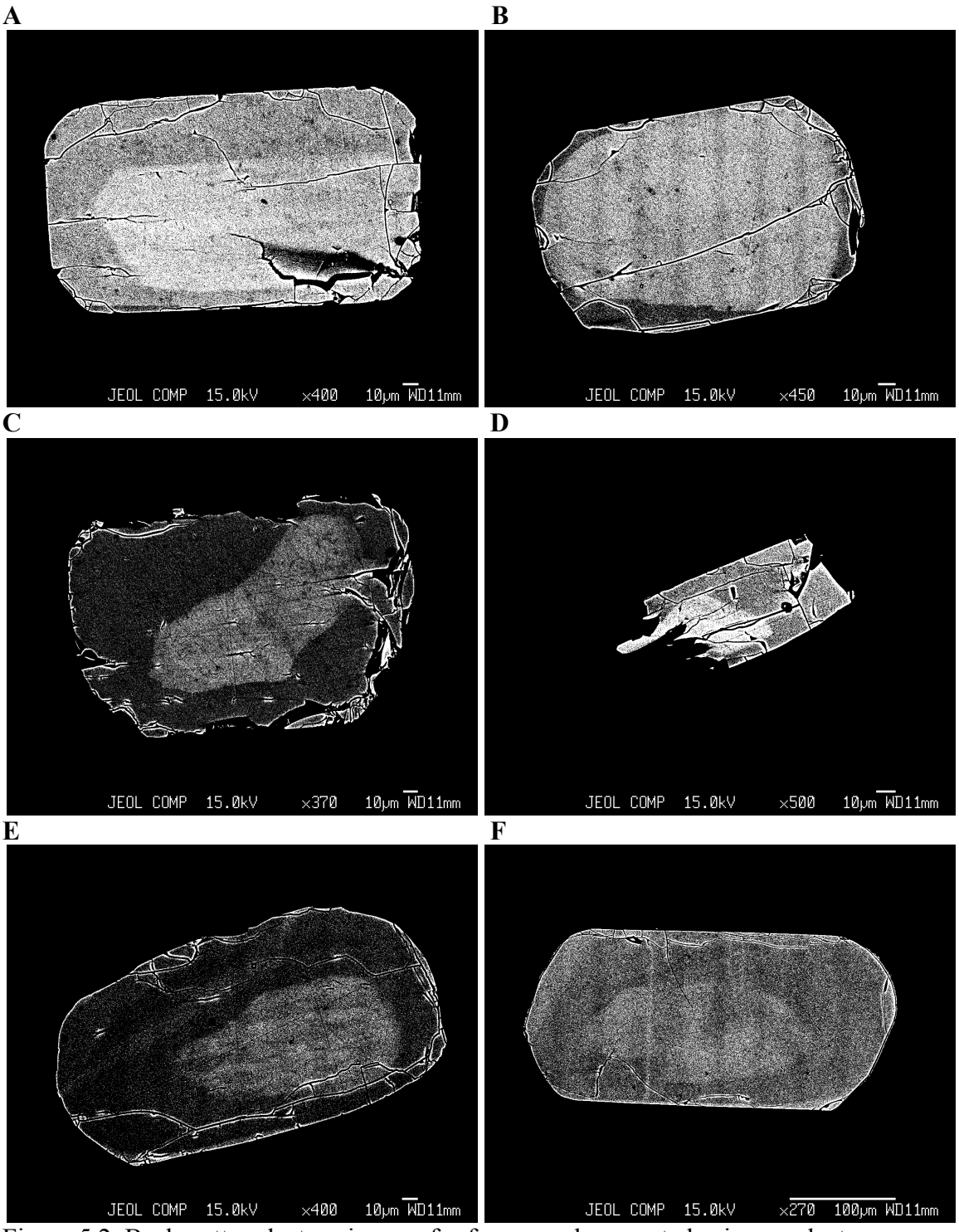

Figure 5.2. Backscatter electron images for four samples, created using an electron microprobe (EMP). The images reveal the distribution of the grains' chemical constituents based on their relative atomic masses (i.e., heavy vs. light elements). Samples shown are: B105 (A & B); C008 (C); C053 (D); and Y080 (E & F). The darker, greyish vertical patterns observed in B, E and F are artifacts of the EMP and do not reflect the zonation character.

5.4 Grain geometry

Grain radius has also been shown to affect the T_c of individual grains, dependent upon the cooling rate (Farley, 2000; Reiners and Farley, 2001). According to diffusion equation for standard Durango apatite, He diffusivity varies as a function of grain radius because the ^{4}He diffusion domain is the entire grain (Farley, 2002). The impact of grain size on diffusion is most apparent in scenarios of slow cooling, where the [He] approaches an equilibrium between alpha production and diffusive loss; the He age will be very sensitive to slight variances in diffusivity, resulting in a trend between He age and grain radius (Farley, 2002).

AHe ages of several samples from both coastline-perpendicular and vertically oriented transects exhibited correlations between grain radius and cooling age, suggesting a possible influence on He diffusion. This was most clearly demonstrated in the relationship between the ratio of {He} to eU (as a proxy for AHe age, where {He} is the F_T-corrected [He]) versus grain radius (Figs. 5.3–5.4). The {He}:eU ratio allows for consideration of differential ^{4}He retention (diffusion) among grains, while not considering the temporal component of the AHe age. Interestingly, {He}:eU in both the margin-perpendicular and vertical transects show positive and negative correlations with grain radius, in contrast with the observations by Reiners and Farley (2001) of AHe ages that were positively correlated with increasing radius. Moreover, similar correlations were also observed between {He}:eU and grain aspect ratio (length:width), which suggests that in addition to grain radius, grain geometry may control ^{4}He diffusion (Figs. 5.5–5.6). However, the majority of these samples also display correlations between grain geometry (i.e., radius and aspect ratio) and eU concentration (Figs. 5.7–5.10). Because this correspondence is independent of a sample's thermal history, it was decided that no

link could be established between grain geometry and AHe age based on the apparent correlations.

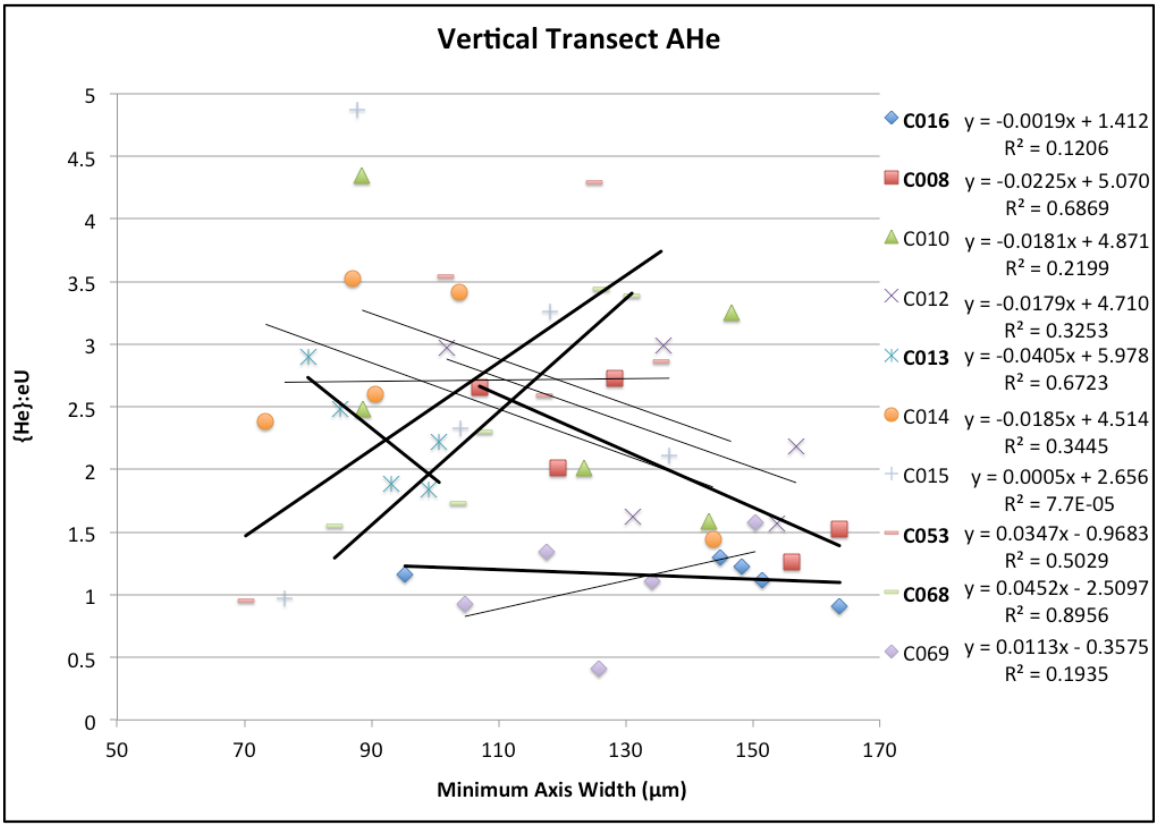

Figure 5.3. Influence of grain size on He diffusion in the individual aliquot AHe data from the vertical transect samples. Each sample had five aliquots analyzed; symbols of similar shape and color are aliquots from the same sample. {He}:eU is used as a proxy for AHe age (see text, and Fig. 5.14 for conversion from ratio to AHe age). Linear equations are provided for best-fit lines, along with the associated Pearson correlation-coefficient (R^2). Bold sample names and best fit lines highlight samples with higher correlation coefficients.

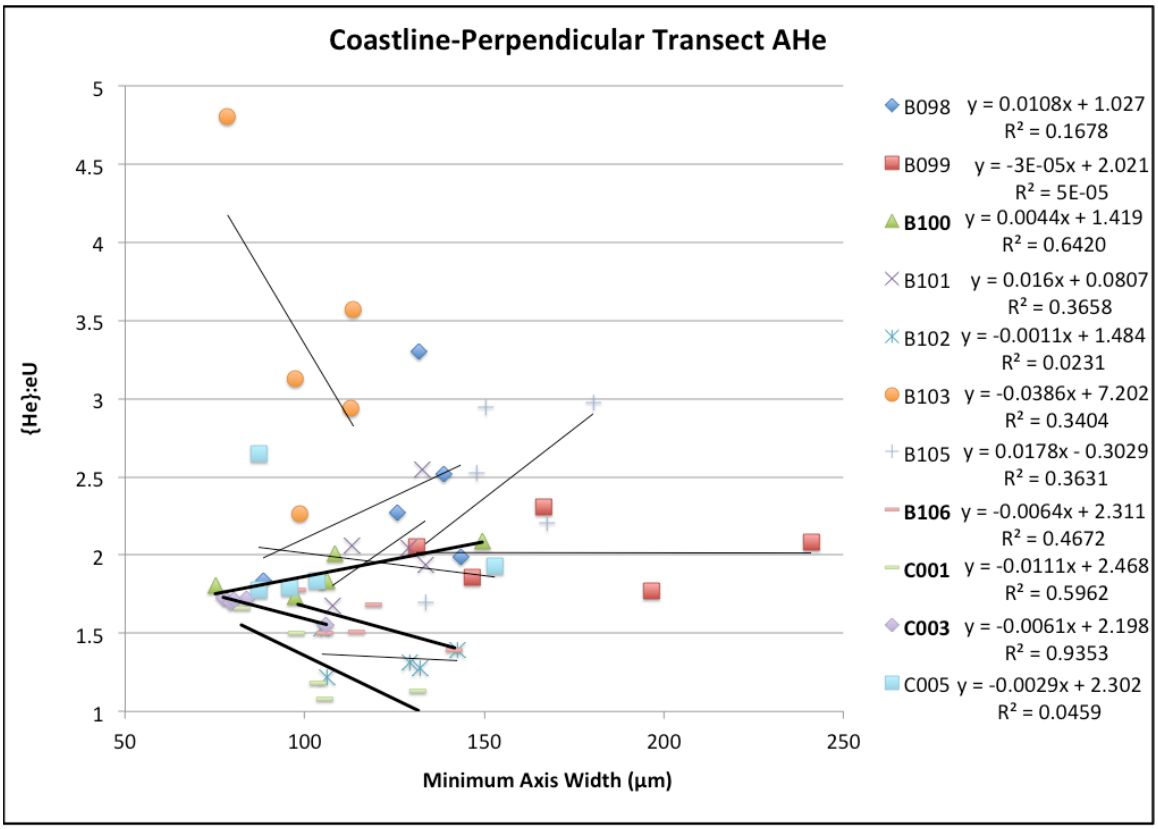

Figure 5.4. Influence of grain size on He diffusion in the individual aliquot AHe data from the coastline-perpendicular transect samples. Same legend as Figure 5.3.

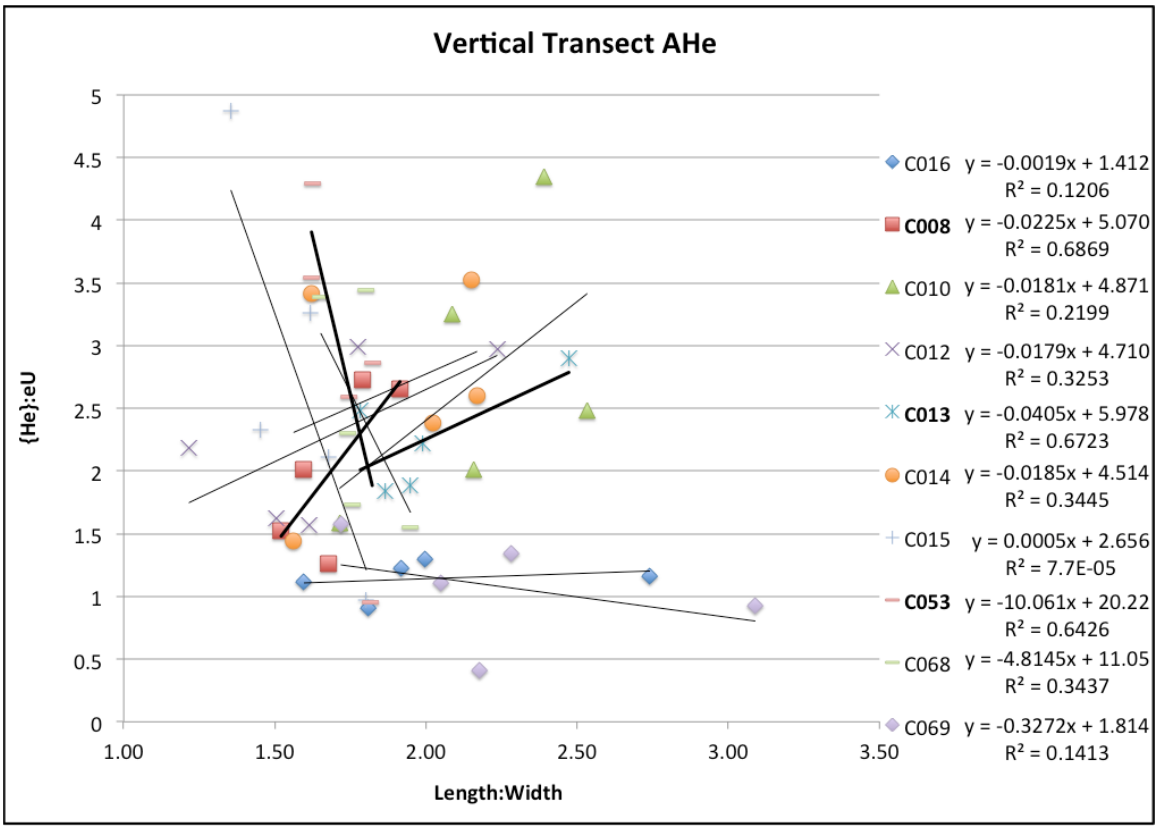

Figure 5.5. Effect of grain aspect ratio (length:width) on He diffusion in the individual aliquot AHe data from the vertical transect samples. Same legend as Figure 5.3.

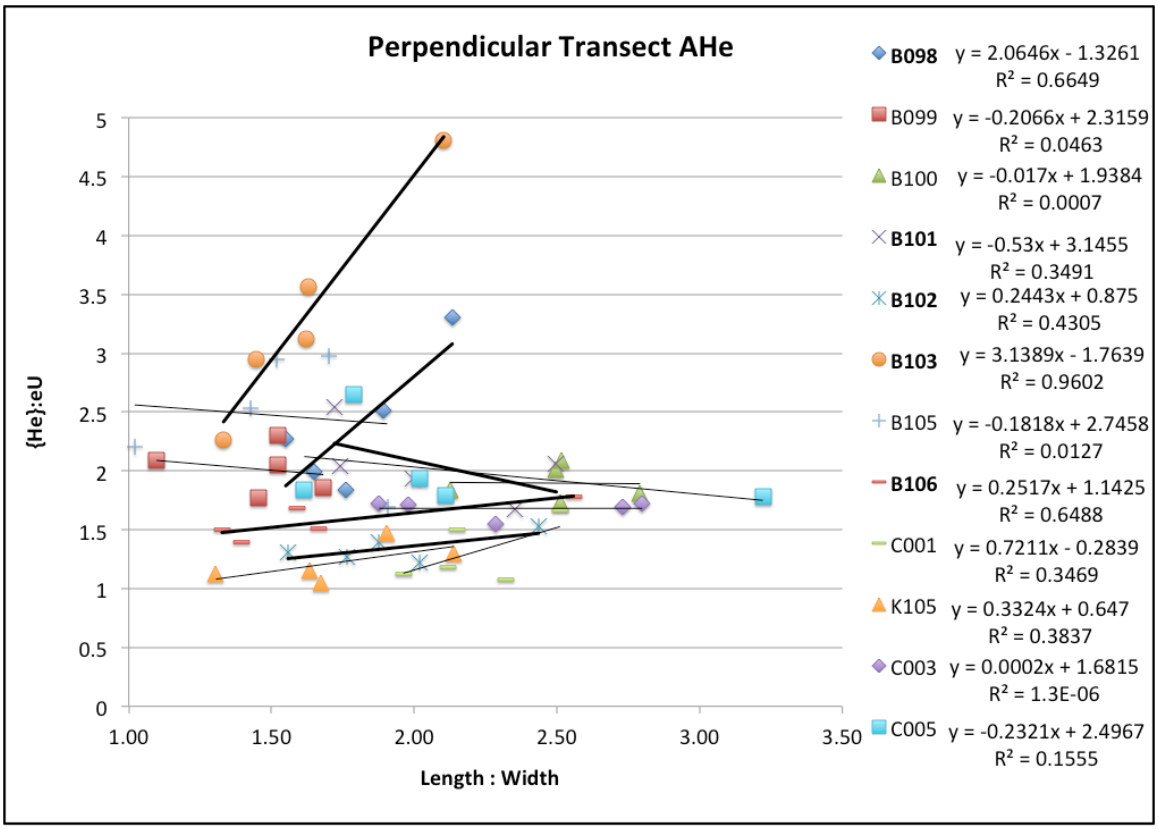

Figure 5.6. Effect of grain aspect ratio (length:width) on He diffusion in the individual aliquot AHe data from the coastline-perpendicular transect samples. Same legend as Figure 5.3.

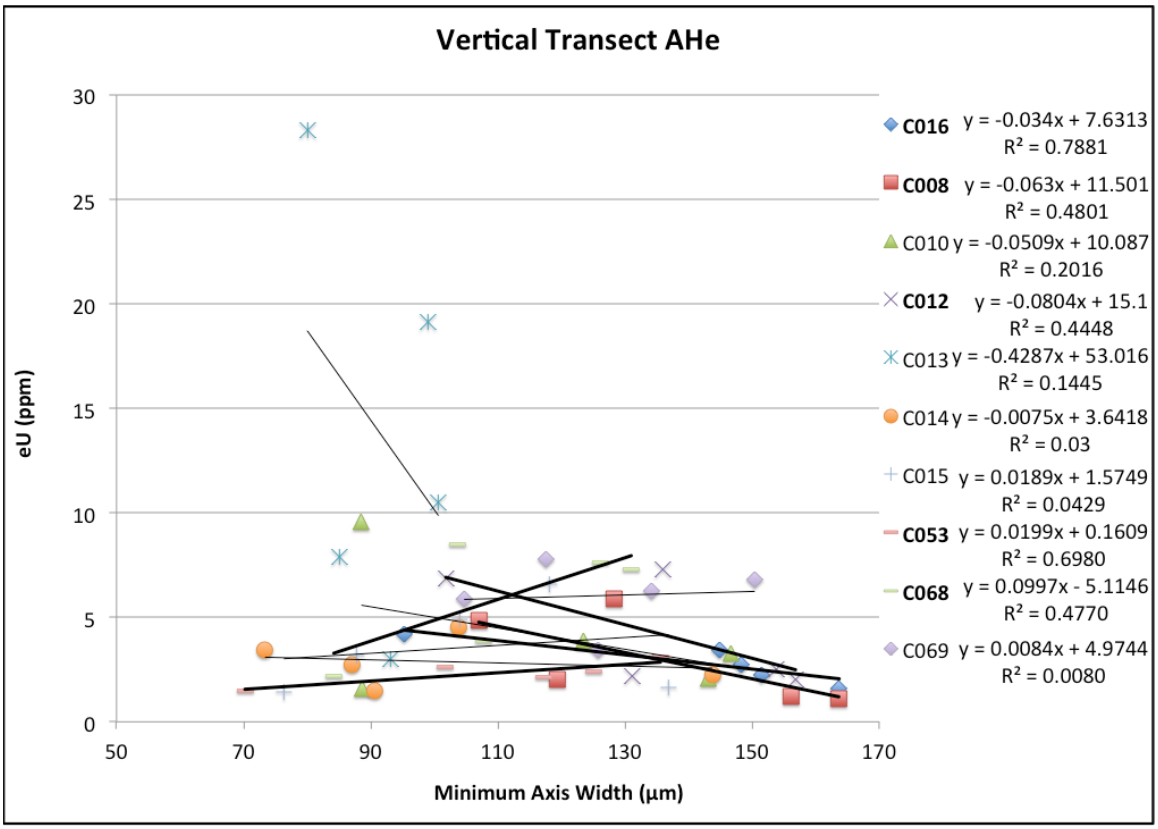

Figure 5.7. Correlation between grain size and parent nuclide concentration (eU) in the individual aliquot AHe data from the vertical transect samples. Same legend as Figure 5.3.

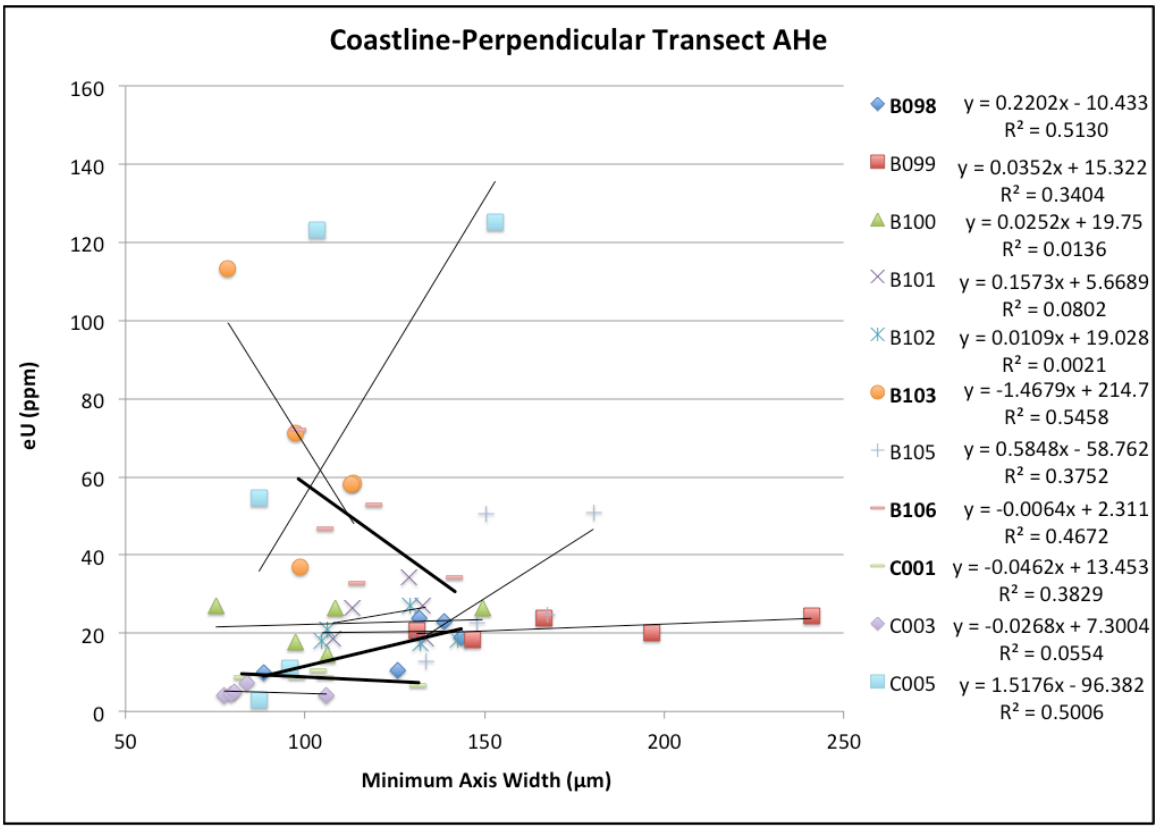

Figure 5.8. Correlation between grain size and eU in the individual aliquot AHe data from the coastline-perpendicular transect samples. Same legend as Figure 5.3.

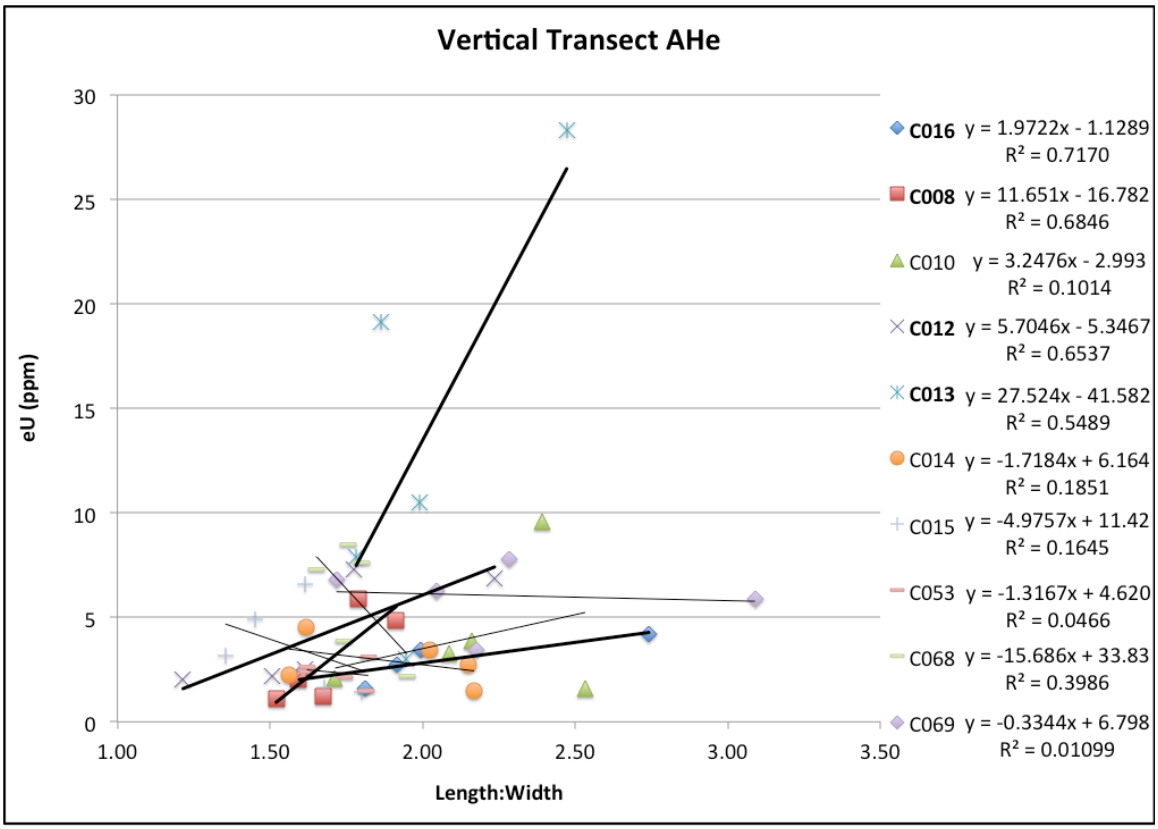

Figure 5.9. Correlation between grain aspect ratio (length:width) and effective U concentration (eU) in the individual aliquot AHe data from the vertical transect samples. Same legend as Figure 5.3.

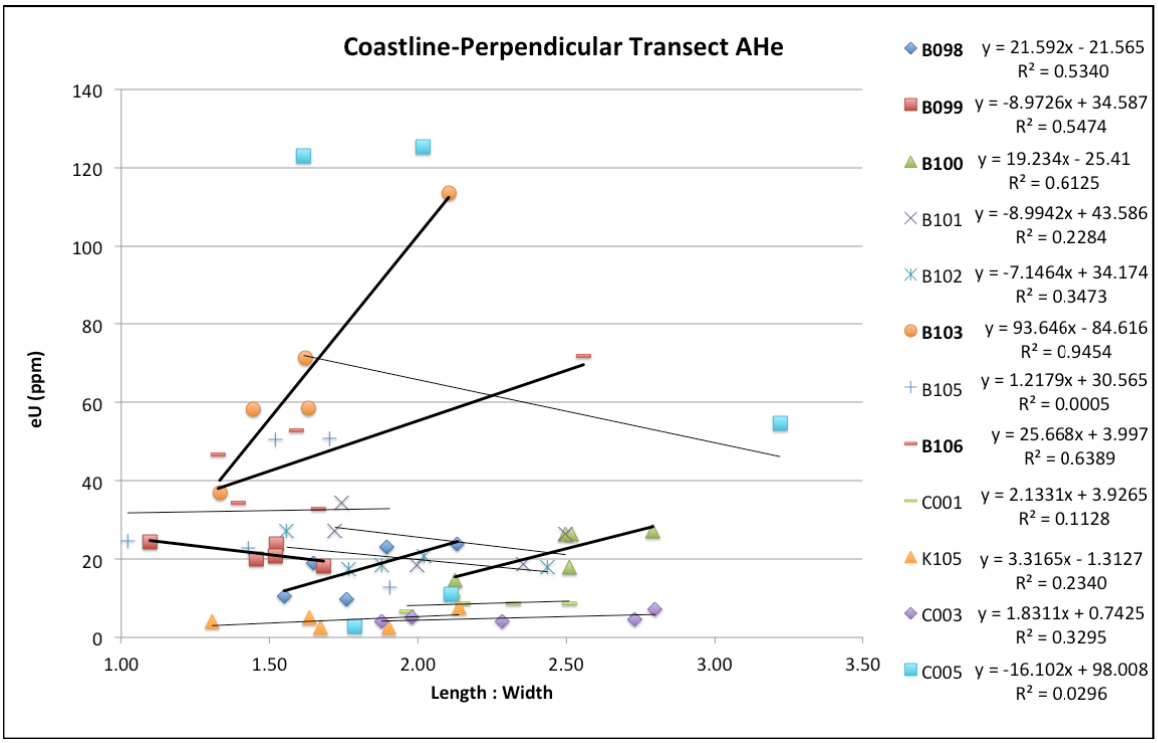

Figure 5.10. Correlation between grain aspect ratio (length:width) and eU in the individual aliquot AHe data from the coastline-perpendicular transect samples. Same legend as Figure 5.3.

5.5 Alpha-recoil damaged grains: altered 4He diffusion kinetics

Damage within a grain is thought to result from alpha decay of U, Th and Sm (Hurley, 1954; Shuster et al., 2006). As the nuclides undergo alpha decay, recoil from the alpha emission imparts kinetic energy into the crystal lattice, eventually displacing nearby ions and forming cavities within the crystal structure (Shuster et al., 2006). In apatite, theses damage sites act as 'He traps' by increasing the energy required to diffuse out of the traps. This increases the effective closure temperature and, in turn, yields older AHe ages. The theory for this was introduced by Shuster et al. (2006), in the form of the Helium

Trapping Model (HeTM). The HeTM constituted a modified equation for ^{4}He diffusion kinetics in apatite,

$$\frac{\mathbf{D}(T, {}^4He)}{a^2} = \frac{\frac{D_0}{a^2} * e^{\frac{-E_a}{RT}}}{\left[(k_0 v_{rd}) * e^{\frac{E_t}{RT}}\right] + 1}$$

where D is diffusivity, a is grain radius, ^4He is He concentration, D_0 is diffusivity through an undamaged crystal at an infinite temperature, E_a is the activation energy required for diffusion through an undamaged crystal, E_t is the required energy for a ^{4}He nuclide to move from a trap into the undamaged crystal lattice, R is the gas constant, T is temperature in Kelvins, and $k_0 v_{rd}$ is the product of the radiation damage density (v_{rd}) and a scaling factor (k_0). Because they were unable to directly measure the amount of radiation damage present in a grain, Shuster et al. (2006) proposed that the measured [^{4}He] could be used as a proxy for v_{rd} to estimate the total radiation damage dose. Their modified equation hence allowed ^{4}He diffusion to evolve with time as a function of alpha-recoil damage accumulation, thereby quantifying the decrease in diffusivity due to the formation of ^{4}He traps. Consequently, the modified HeTM kinetics can be used to calculate a higher effective closure temperatures (T_{ec}), and in turn, AHe ages older than those modeled using conventional Durango diffusion kinetics. As a result, the HeTM proved especially useful for interpreting ages from tT histories with periods of slow cooling, where grains are more susceptible to accumulating radiation damage and often exhibit individual AHe ages that correlate with increasing eU (Fig. 5.11).

A major limitation of the HeTM, however, is its inability to compensate for radiation damage annealing, and the fact that radiation damage accumulation and ^{4}He retention potentially occur at different rates (i.e., alpha-decay damage can occur above T_c for (U-

Th-Sm)/He in apatite) (Flowers et al., 2009; Gautheron et al., 2009). Subsequent work by Shuster and Farley (2009) was aimed specifically at addressing the limitations of the HeTM using artificially-produced radiation damage to model annealing of alpha-recoil damage, and suggests the annealing behavior of alpha-recoil damage is analogous to annealing of fission tracks. This led to the ensuing development of two independently formulated ^{4}He diffusion kinetic models (Flowers et al., 2009; and Gautheron et al., 2009) that consider the effects alpha-recoil damage accumulation and annealing. Both of these models directly incorporate the work of Shuster and Farley (2009) by utilizing AFT annealing behavior as the proxy for radiation damage annealing (Gautheron et al., 2009).

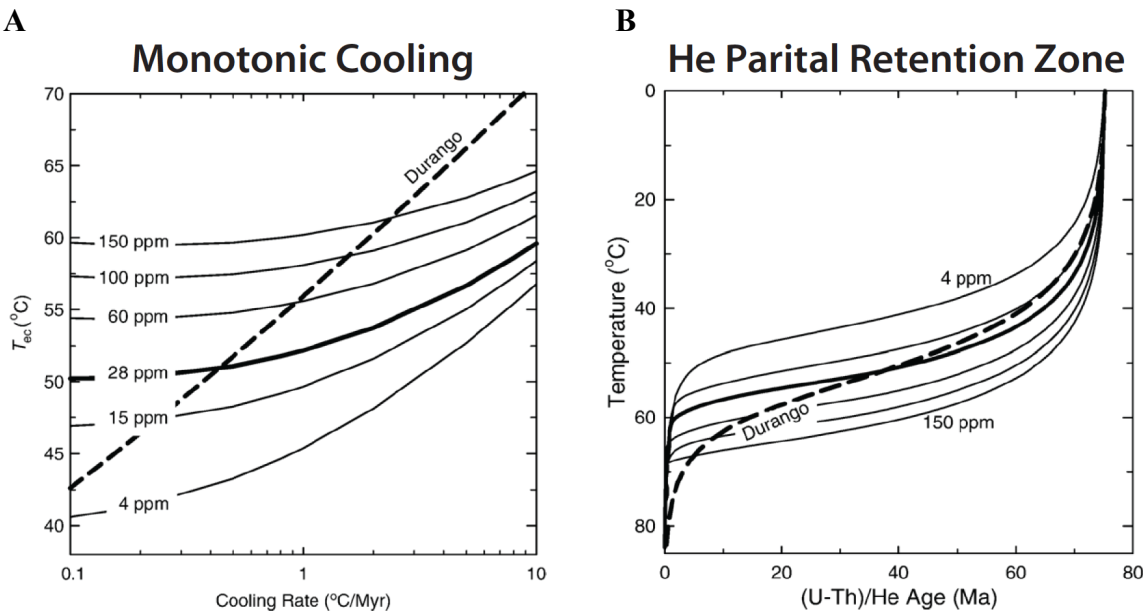

Figure 5.11. Effective closure temperature of the AHe thermochronometer, as defined by Helium-trapping Model (HeTM). (A) Variation of the effective closure temperature (T_{ec}) as a function of eU and cooling rate, as predicted by the damage-based apatite diffusion kinetics of the HeTM. Predicted T_{ec} using standard Durango apatite kinetics are also shown for comparison. All cooling paths started at 100 ºC at different times to produce the various rates. (B) Evolution of the apatite He partial retention zone (HePRZ) as a function of varying eU, according to the HeTM. Indicates measured AHe age for a grain held isothermally for 75 Myr at a given temperature. Unlabeled lines are 15, 28, 60, and 100 ppm eU (top to bottom, respectively). Both illustrations from Shuster et al. (2006).

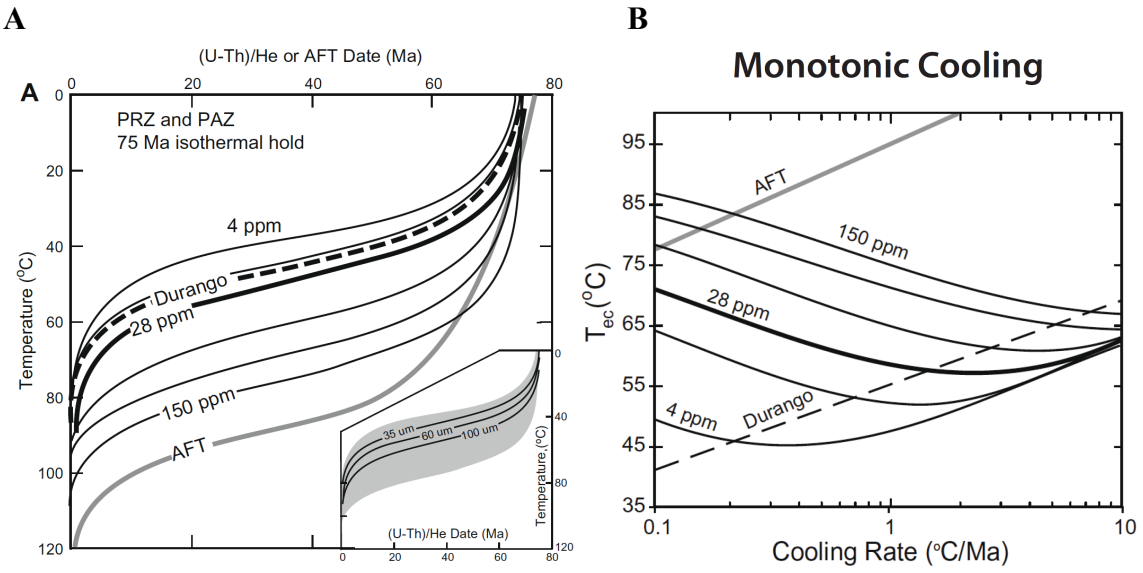

Figure 5.12. Effective closure temperature of the AHe thermochronometer, as defined by Radiation-Damage Accumulation and Annealing Model (RDAAM). (A) The helium partial retention zone (HePRZ) for apatite of a given eU, calculated using the RDAAM under isothermal conditions for 75 Myr. Unlabeled lines are 15, 28, 60, and 100 ppm eU (top to bottom, respectively); bold dashed line is for conventional Durango apatite kinetics; grey line is the partial annealing zone for the apatite fission-track thermochronometer, computed using the annealing kinetics of Ketcham et al. (2007). The inset compares the relative effect of grain radius versus eU on the HePRZ. Lines indicate the HePRZ for apatite grains with various radii (35, 60 and 100 µm), and grey area shows the extent of the HePRZ for grains ranging in eU from 4 to 150 ppm and a fixed radius of 60 µm. (B) Calculated Tec for different cooling rates and eU, using the RDAAM diffusion kinetics. Same legend as Fig. 5.4A. Note that the RDAAM predictions differ from the HeTM in that it predicts an inverse relationship between Tec and cooling rates in grains above 28 ppm eU or at rates below 1 ºC/Ma. Both illustrations from Flowers et al. (2009).

The two models are very similar in that they are based on the principle that buildup of alpha-recoil damage effectively increases T_c, as a function of the thermal history, notably the residence time in the HePRZ, and eU concentration (Fig. 5.12A). Moreover, the model predictions differ from the HeTM in that they predict an increase in T_{ec} with a decrease in cooling rate, and in the case of high eU and extreme scenarios of slow cooling with prolonged isothermal conditions, the potential for T_{ec} to become equal to or greater than that of the apatite fission-track thermochronometer (Fig. 5.12B). The main

difference between the two models resides in the relationship between damage accumulation and enhanced ^{4}He retention; Gautheron et al. (2009) used a physically-derived equation with a linear relationship, while the radiation damage accumulation and annealing model (RDAAM) of (Flowers et al., 2009) developed an empirically-based equation with a cubic relationship between diffusion and the number of crystal defects. The basis for this difference is that Gautheron et al (2009) could not impute non-linearity to any single physically based mechanism in their equation, and therefore maintained a linear relationship (Gautheron et al., 2009).

Following the development of these alpha-damage based models, several studies have provided insight into the assessment and interpretation of AHe data influenced by radiation damage (e.g., Flowers, 2009; Flowers and Kelley, 2011; Flowers et al., 2007; and others). For example, the most prominent indicator of an influence from alpha-recoil damage is a large inter-grain variation in the measured cooling ages, with a positive correlation between AHe age and eU. Because the dosage of alpha-recoil damage increases with eU, and increasing the damage dose acts to decrease diffusivity, grains with a high eU will retain more ^{4}He than those with lower eU, yielding 'older' He ages even if they experience the same thermal history. Because they spend only a short time in the HePRZ, samples that experience relatively rapid cooling are unaffected by alpha-recoil damage and therefore exhibit no relationship between AHe ages (effectively the ratio of ^{4}He to eU) and eU, as the ^{4}He:eU ratio should scale independently of the total eU (Fig. 5.13).

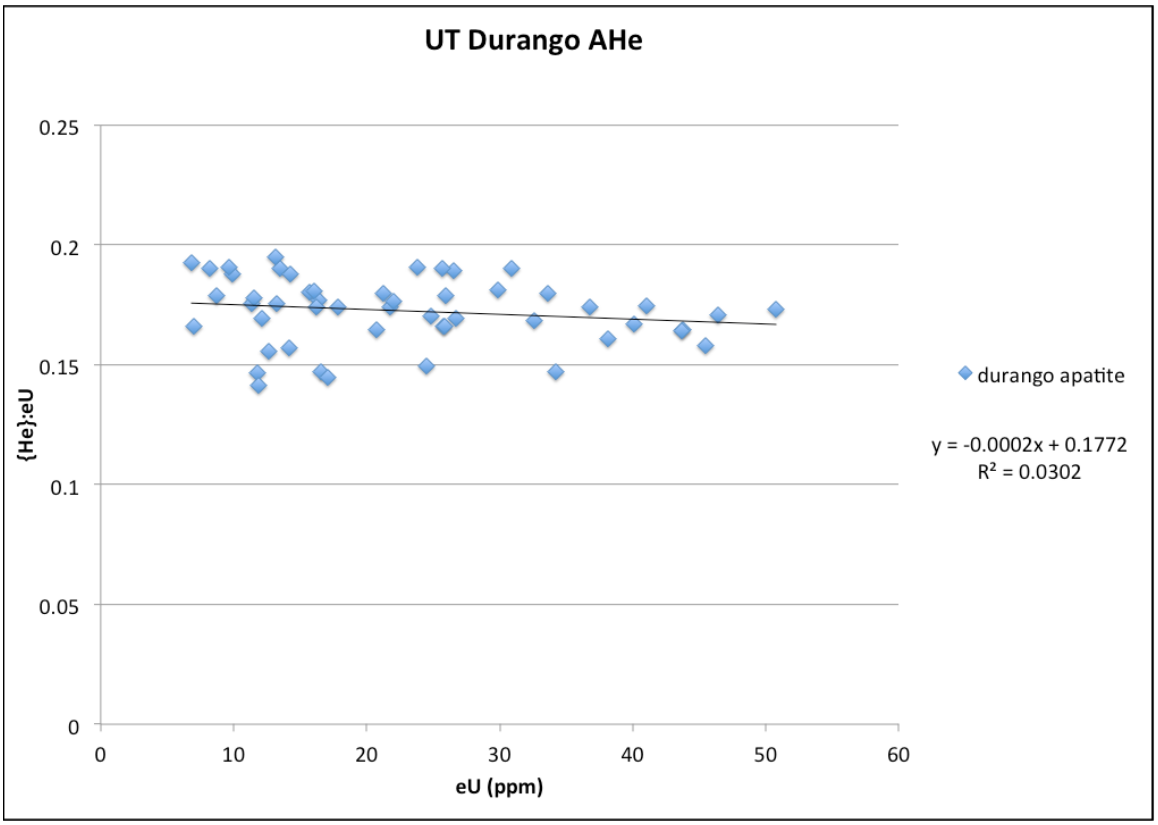

Figure 5.13. AHe data from the Durango apatite standard, analyzed at the University of Texas–Austin. The lack of a positive or negative trend advocates for no appreciable influence of radiation damage on the measured cooling ages. Data provided by R. Kislitsyn.

5.5.1 Contribution of alpha-recoil damage to dispersion in AHe data

To establish whether the large dispersion of He ages observed in the data was the result of alpha-recoil damage, the data were evaluated in two ways: 1) plotting eU versus {He}:eU to demonstrate the potential control of eU concentration on ^{4}He retention, and comparing this to the University of Texas–Austin (UT) Durango data (Fig. 5.13); and 2) plotting {He} vs. eU, to test for linearity and potentially identify outlier aliquots in the samples. Figure 5.14 depicts the relationship between the daughter/parent ratio and AHe age, demonstrating the linear relationship between increasing or decreasing the {He}:eU ratio and calculated AHe age.

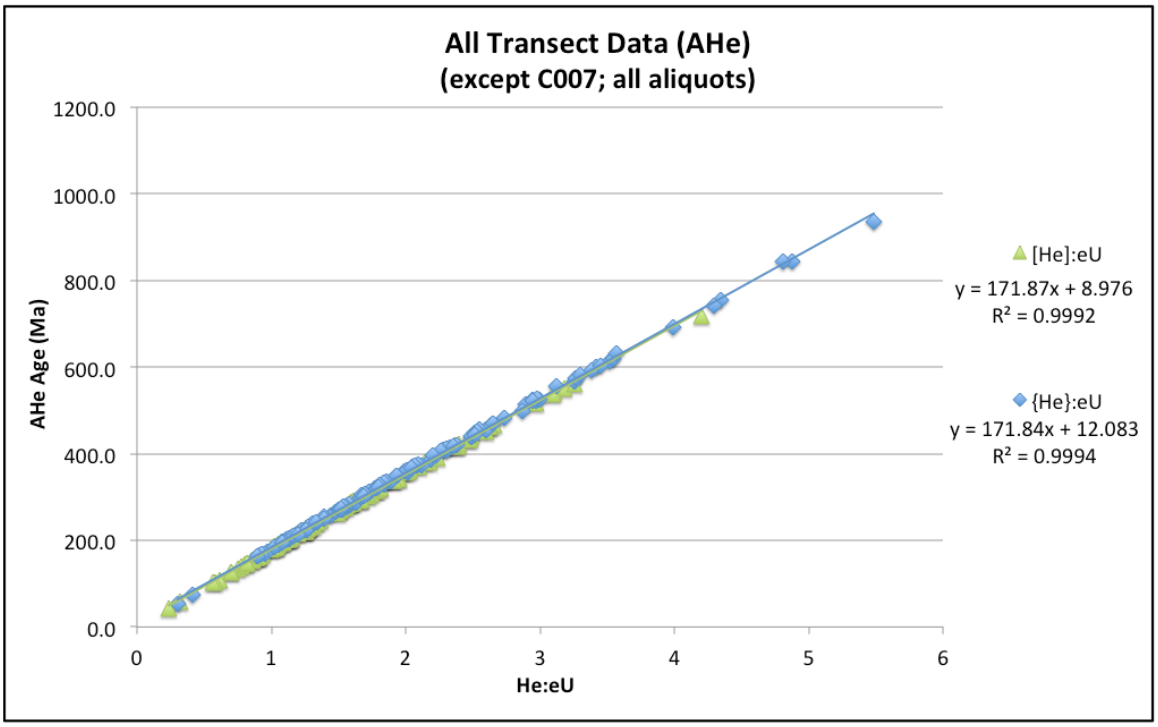

Figure 5.14. Relationship between ratio of [He] to eU and calculated AHe age. [He] is measured ^{4}He concentration; {He} is F_T-corrected ^{4}He concentration ({He} = [He]/F_T). Plot includes all aliquots from all samples (except sample C007).

Indeed, plotting {He}:eU versus eU confirmed that most of the measured AHe age dispersion was largely a function of eU concentration; this was especially evident in the vertical transect data (Fig. 5.15). Using the slope of the best-fit regression line for the relationships between {He}:eU versus eU as a proxy for the 'apparent dose' of radiation damage, such that a steeper slope reflects a increased sensitivity to higher eU, the vertical transect samples appear to have a higher 'apparent dose' of radiation damage than samples from the coastline-perpendicular transect (Figs. 5.16–5.17). This observation differs from the predictions by the RDAAM that grains with lower eU concentrations are less susceptible to the effects of radiation damage (e.g., Flowers et al., 2009; Shuster et al., 2006). In the perpendicular transect samples, the slope of the best-fit lines were

mostly an order of magnitude lower than the vertical transect samples, suggesting the possibility of a reduced influence of radiation damage on diffusivity, although eU still appears to assert a first-order control on AHe age. However, samples C005, C003 and Y080 exhibited minimal response/effect to eU, thus suggesting that they had little (if any) apparent radiation damage and a diffusion character similar to the UT Durango data (i.e., m = 0; Fig. 5.13).

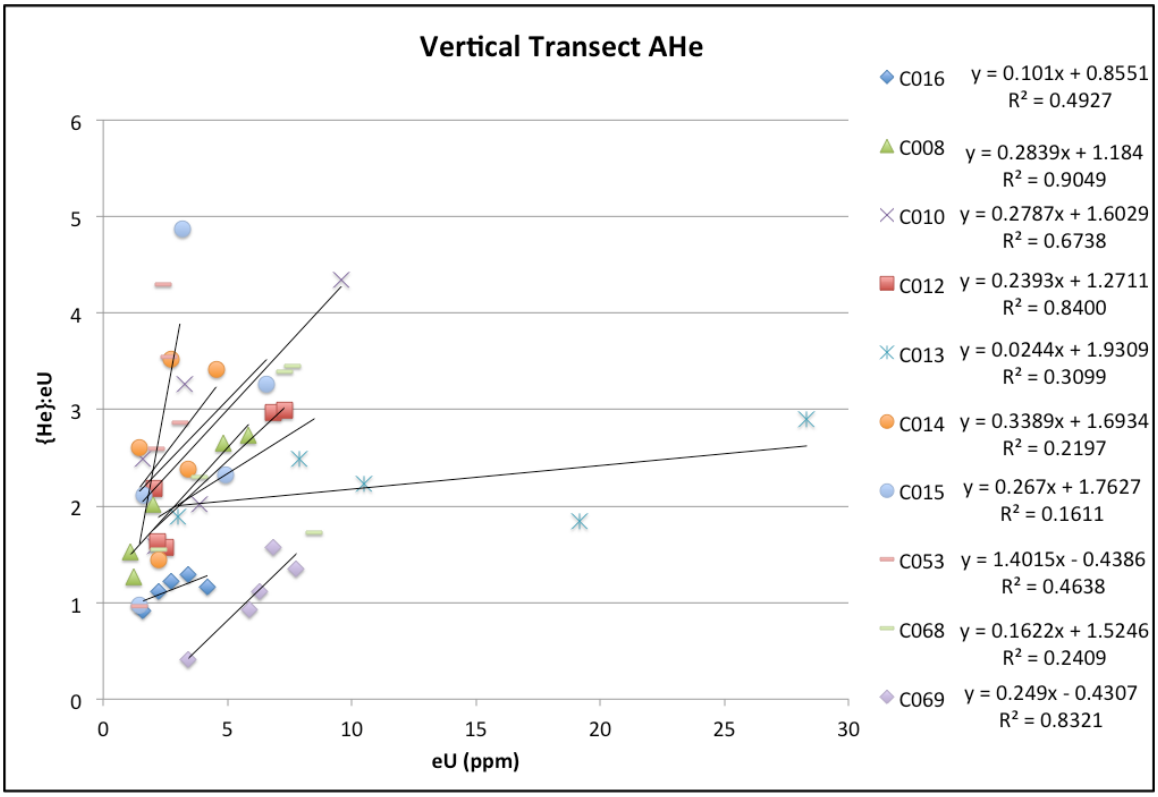

Figure 5.15. Manifestation of alpha-recoil damage affecting the vertical transect AHe data. Same legend as Fig. 5.3. See text for discussion.

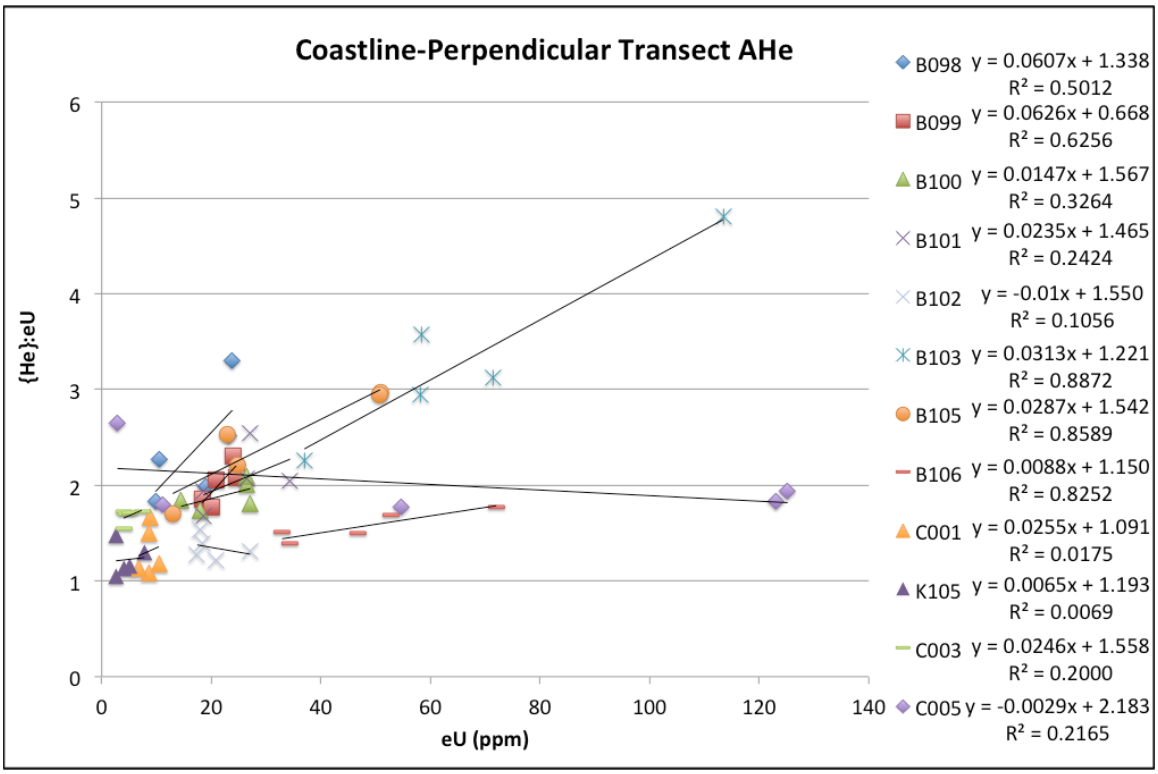

Figure 5.16. Manifestation of alpha-recoil damage affecting the coastline-perpendicular transect AHe data. Same legend as Fig. 5.3. See text for discussion.

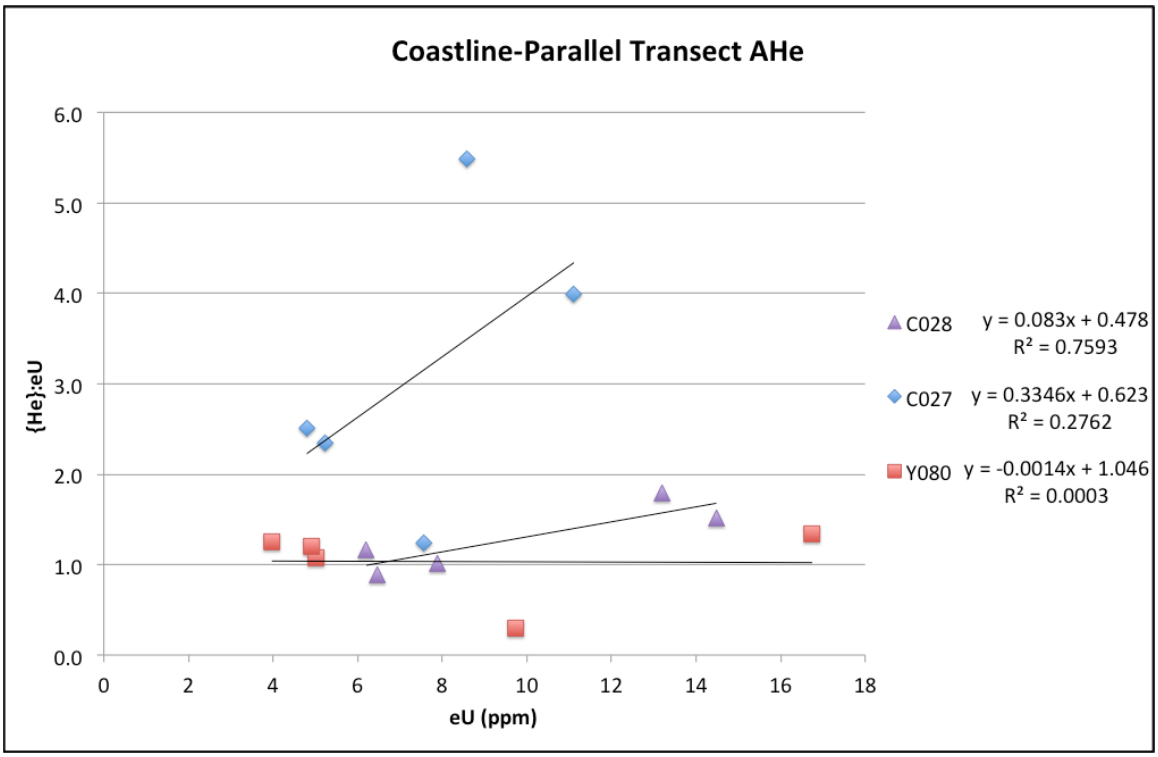

Figure 5.17. Manifestation of alpha-recoil damage affecting the coastline-parallel transect AHe data. Same legend as Fig. 5.3. See text for discussion.

The other method used to establish the data quality was plotting {He} versus eU for each sample. In grains with an absence of alpha-recoil damage, the amount of {He} should increase linearly with eU. For grains that have accumulated enough radiation damage to alter ^{4}He diffusion, those with higher eU are expected to retain a greater proportion of ^{4}He. In these circumstances, plots from samples with aliquots yielding a span of eU were expected to display a nonlinear trend at higher eU values owing to the retardation of diffusion; however this was not explicitly the case. All three transects yield some samples that plot linearly and some non-linearly, thus providing inconclusive evidence for assessing the radiation damage character of the dataset as a whole (Figs. 5.18–5.20). However, the plots proved useful for characterizing notably discordant

aliquots that were outliers in the trend of the other grains. Although it is difficult to directly determine the cause of these outliers, given the exclusion of other factors previously discussed in this chapter, the most likely cause for many of these outliers was alpha particle injection from nearby U-Th rich grains.

A

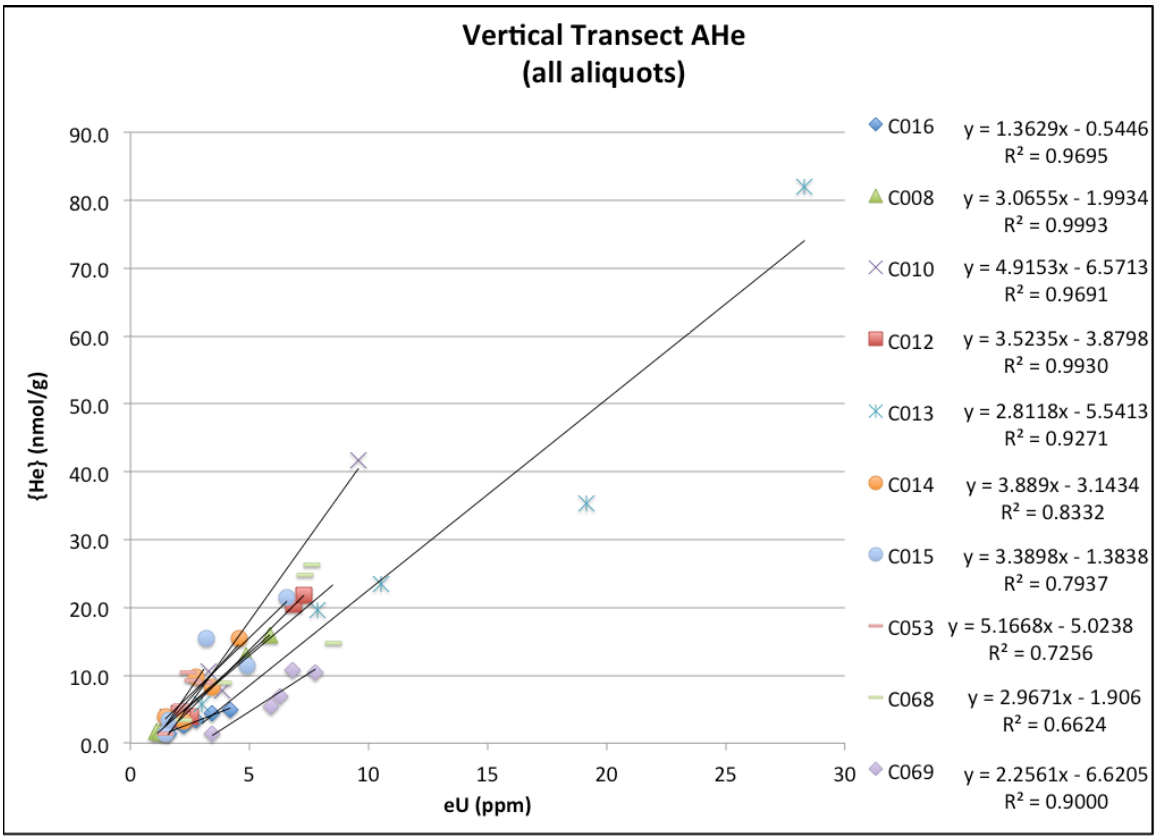

Figure 5.18. Raw data from AHe analyses from the vertical transect samples. {He} is F_T-corrected [He]. A linear trend in the sample is produced by aliquots which underwent standard diffusion, with an absence of any extraneous factors controlling the AHe age (e.g., ^{4}He-implantation from nearby grains). Accordingly, samples with a low Pearson correlation coefficient ($R^2 < 0.9$) contain a single outlier that significantly reduced the apparent correlation strength. If these single outlier aliquots were excluded, most samples yielded $R^2 \leq 0.9$. Samples with $R^2 > 0.9$ are rated higher; abide by diffusion kinetics as defined by RDAAM. (B) Same data as (A), with exclusion of sample C013 to enhance visibility (continued on next page).

B

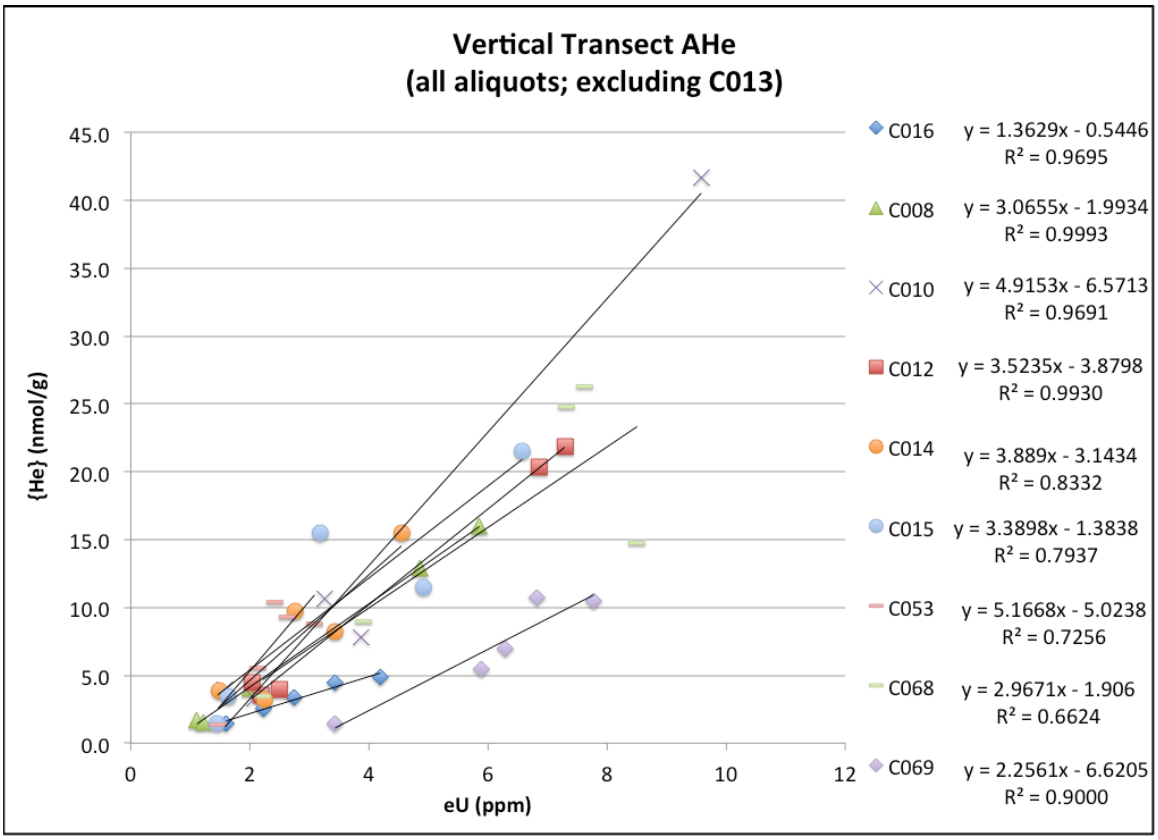
Vertical Transect AHe
(all aliquots; excluding C013)
{He} (nmol/g)
eU (ppm)
0.0
5.0
10.0
15.0
20.0
25.0
30.0
35.0
40.0
45.0
0
2
4
6
8
10
12
C016 y = 1.3629x - 0.5446 R² = 0.9695
C008 y = 3.0655x - 1.9934 R² = 0.9993
C010 y = 4.9153x - 6.5713 R² = 0.9691
C012 y = 3.5235x - 3.8798 R² = 0.9930
C014 y = 3.889x - 3.1434 R² = 0.8332
C015 y = 3.3898x - 1.3838 R² = 0.7937
C053 y = 5.1668x - 5.0238 R² = 0.7256
C068 y = 2.9671x - 1.906 R² = 0.6624
C069 y = 2.2561x - 6.6205 R² = 0.9000

A

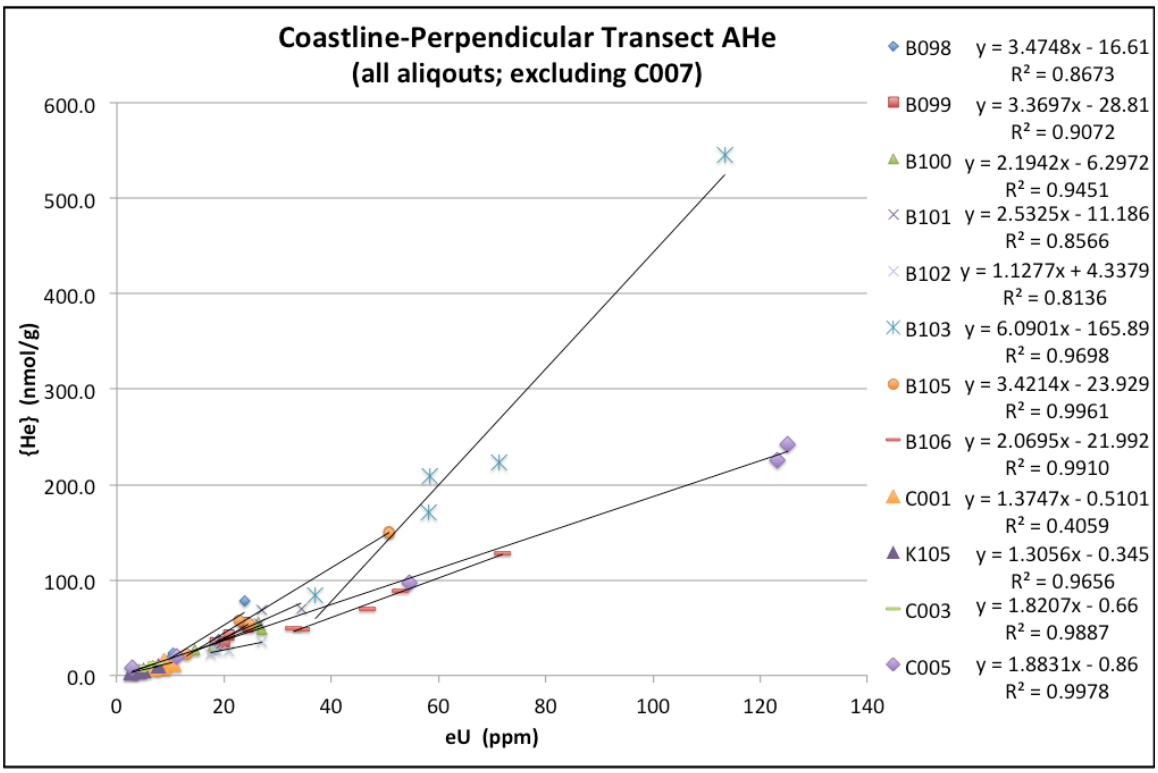

Figure 5.19. Raw data from AHe analyses on the coastline-perpendicular transect samples. Same legend as Figure 5.18. (B) Same data as (A), excluding the two high eU aliquots of C005 to improve visibility (continued on next page). Note the generally better fits of the data than that of the vertical transect data (Fig. 5.18).

B

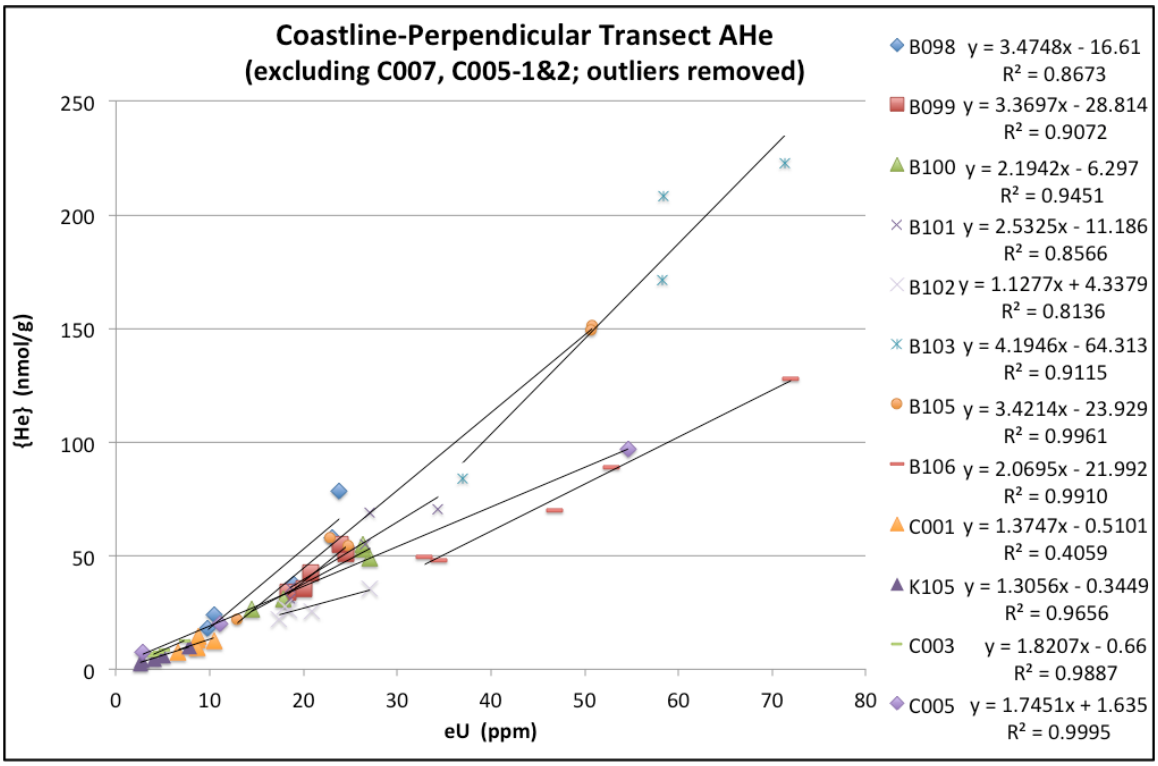

Figure 5.20. (Below) Raw data from AHe analyses on the coastline-parallel transect samples. Same legend as Figure 5.18.

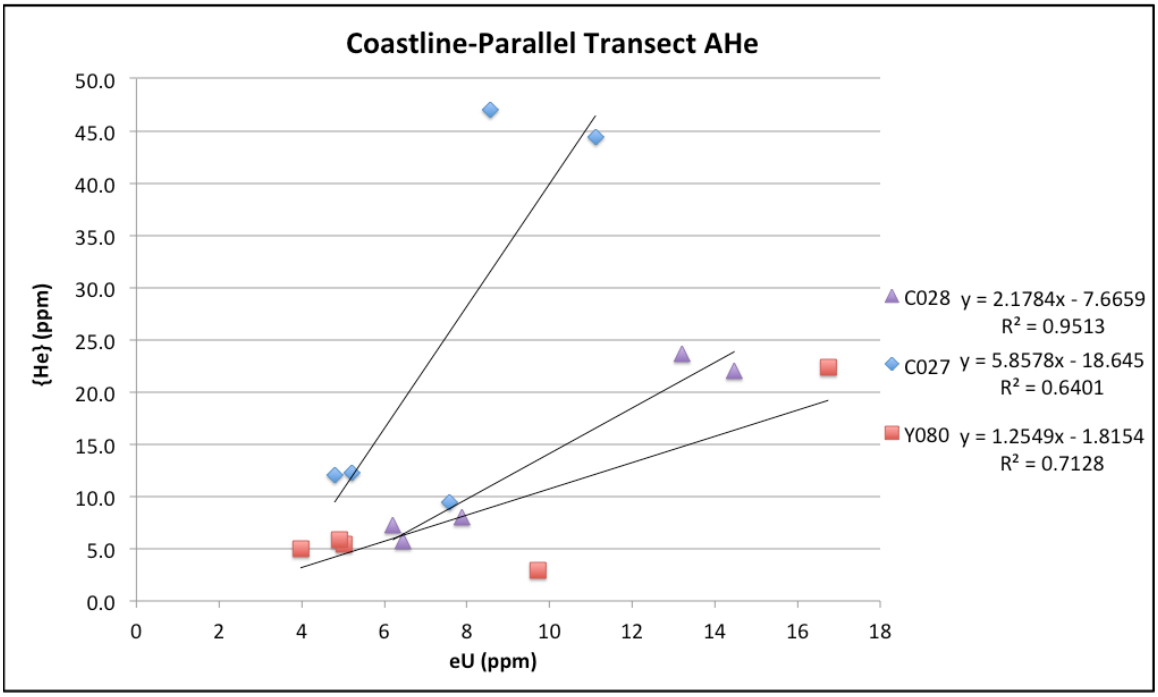

5.5.2 Radiation damage in the ZHe data

The effect of alpha-recoil damage on the ZHe thermochronometer has been the focus of much research, however a complete understanding of the damage-based He kinetics of zircon remains enigmatic (Goldsmith et al., 2014; Guenthner et al., 2013; Nasdala et al., 2004; review in Reiners, 2005). This is largely because the He diffusion kinetics in zircon appear much more complex than in apatite, partly due to the much higher concentrations of U and Th typically observed in zircon (1-2 orders of magnitude higher than apatite), as well as differences in the crystalline structure. For low doses of alpha recoil damage, He-retention in zircon is predicted to result in a decrease in diffusivity, similar to the behavior of apatite. However, at high doses of alpha damage, it is thought that the damage sites become interconnected, resulting in an overall increase in the diffusion of He. Recently, Guenthner et al. (2013) developed a zircon radiation damage accumulation and annealing model (ZRDAAM) to account for the time-varying diffusion due to alpha-recoil damage in the ZHe thermochronometer. The model is similar to the RDAAM of Flowers et al. (2009), as it also uses spontaneous fission-tracks as both a proxy for the dose of radiation damage and an analogue for its annealing behavior. Based on available data, the ZRDAAM predicts a 1-2 order of magnitude decrease in diffusivity for low dose radiation damage (i.e., low eU grains), and up to 8 orders of magnitude increase in diffusivity for grains with very high dose radiation damage (i.e., high eU grains) (Guenthner et al., 2013).

In a similar approach with the AHe data, the ZHe data in this study were plotted with {He}:eU versus eU, and {He} versus eU, to assess whether the scattered He ages were linked to recoil-damage altered diffusion. The {He}:eU versus eU plots clearly reveal a

strong influence from radiation damage (Fig. 5.21). As predicted by ZRDAAM, the low eU grains from samples zC008, zC068 and zC053 demonstrated increased ^{4}He retention with increasing eU, while samples with higher eU grains (> 150 ppm) yielded progressively lower cooling ages with increasing eU. Comparable trends were apparent in the {He} vs. eU plots, where the grains with eU > 150 ppm yielded non-linear trends, distinctly different from the lower eU grains (Fig. 5.22). Together, these plots suggest extremely high doses of alpha-recoil damage in the grains.

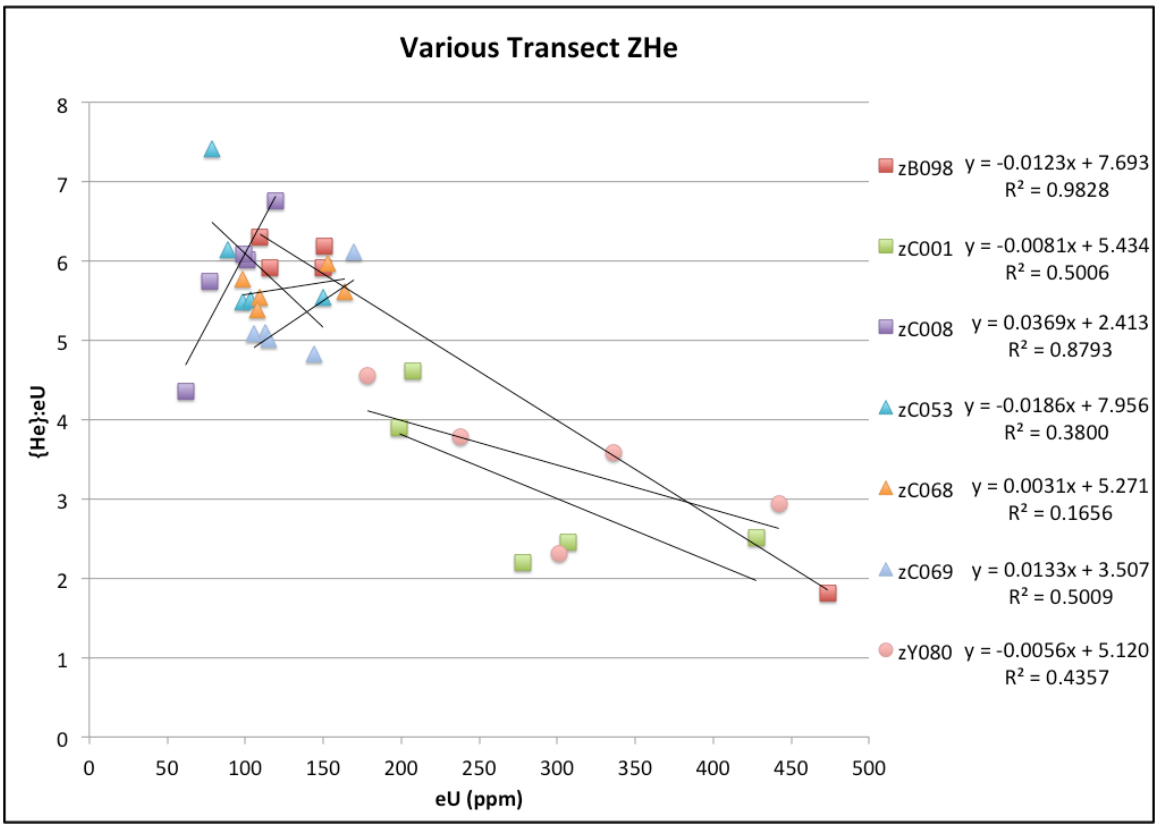

Figure 5.21. Strong influence of eU on the {He}:eU ratio (ZHe age) in the ZHe data from samples in the various transects. As predicted by the ZRDAAM for grains with high dosage of alpha-damage, low eU aliquots (here, <150 ppm) exhibit a positive correlation with eU, and higher eU (> 150 ppm) aliquots demonstrate a strong negative relationship with increasing eU.

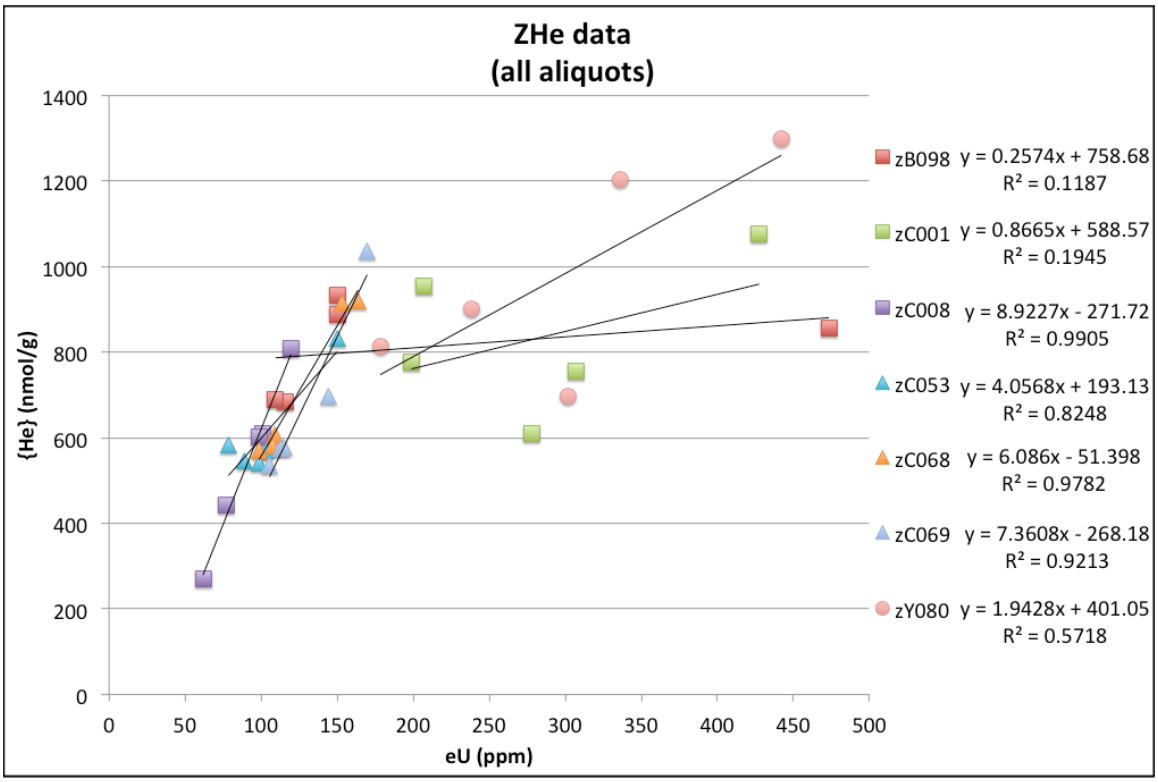

Figure 5.22. Raw data from ZHe analyses. Same legend as Figure 5.18. Note the abrupt change in slope at ~150 ppm eU, suggesting distinct diffusion character for grains of different eU.

5.6 Correction applied to measured He ages

Initially, several novel approaches were devised and implemented to correct the 'artificially old' He ages for the effects of alpha-recoil damage. These included interpreting only the minimum single-aliquot AHe age from each sample; calculating 'corrected' sample ages based on the {He}:eU ratio of the y-intercept of their best-fit line in the {He}:eU versus eU plots (Figs. 5.15–5.17); calculating 'corrected' grain ages for the coastline-perpendicular samples based on a linear regression using the slope of the best-fit line of sample C005 (Fig. 5.16); and, finally, using the samples own {He}:eU ratio at a given (low) eU value (Fig. 5.16) to calculate a 'corrected' ^{4}He concentration,

and in turn, a ‘corrected’ AHe age for each grain. However, after several attempts, none of these corrections were successful in providing geologically feasible results, and it was decided to forgo the corrections and instead employ thermal modeling programs to account for the effects of radiation damage and help further elucidate the measured data.

CHAPTER 6 – ONE-DIMENSIONAL THERMAL MODELING (HeFTy)

Because ^{4}He retention in apatite and zircon is dependent on a number of first and second order parameters (discussed in Chapter 5), it can often be difficult to link the cooling ages to any specific cooling events or interpret the long-term cooling history in a set of samples. This is particularly true in the case of complex, scattered grain ages, such as the data presented in this study. For these cases, thermal models based on a theoretical understanding of the thermochronometer's behavior can serve as a helpful tool, as the models can provide constraints for the range of tT histories suiting the measured data.

6.1 Overview of HeFTy

The thermal modeling program HeFTy (Ketcham, 2005) is used to aid in interpreting the various aliquot cooling ages in each sample. HeFTy is a one-dimensional forward and inverse thermal modeling and thermochronometer age prediction program used to define potential time-temperature (tT) paths for low-temperature thermochronometers (e.g., (U-Th)/He, fission track analysis, and vitrinite reflectance). The input used by HeFTy for (U-Th-Sm)/He thermochronometers includes mineral type, diffusion model (e.g., conventional Durango AHe, Farley, 2000; conventional ZHe, Reiners et al., 2004), and for each grain: radius, uncorrected measured He-age and 1σ error, U-Th-Sm composition, and chemical zoning information (if applicable). Although capable of simultaneously simulating tT paths for many different thermochronometers in the same sample, HeFTy is unable to evaluate a prescribed thermal history for several samples in a single model run. Hence, modeling samples on an individual basis remains a major limitation of the program.

Candidate thermal histories are evaluated in HeFTy in two ways: a forward model approach, with simulation of a single, user defined tT path; or an inverse model approach, in which various tT paths are simulated based on a set of boundary conditions. Forward modeled thermal histories are assessed in four steps. First, the user defines a tT path to test. HeFTy then calculates a theoretical ^{4}He-diffusion profile for each input aliquot based on the prescribed tT path. Next, theoretical He ages of the input aliquots are calculated based on the assigned ^{4}He-diffusion profiles. The new theoretical ages are then compared to the measured He ages by calculating their 'goodness of fit' (GOF). Comparisons with a GOF $\geq$ 0.05 are deemed statistically 'acceptable' and those with a GOF $\geq$ 0.5 are credited as statistically 'good' (Ketcham, 2005). To test the suitability of several different tT paths for yielding He ages similar to the measured data (i.e., perform model inversions), HeFTy uses a Monte Carlo simulation to generate points defining a tT path, with the total number of paths tried, number of points defining each path, and the general path shape set by the user (Ketcham, 2005).

Ideally, the inverse modeling in HeFTy provides a group of tT paths that are consistent with the measured He ages and thus helps to define the sample cooling history. However, HeFTy is not capable of calculating the exact tT path for measured data because cooling ages are non-unique. The inverse model output thus provides insight only into the range of potential thermal histories for each sample. Furthermore, in order to properly utilize the HeFTy model results, additional geological constraints should be incorporated where possible to ensure predicted cooling paths are viable. Supplementary data from a higher temperature thermochronometer (e.g., apatite fission track or zircon fission track analyses), minimum or maximum erosion estimates, grain crystallization age,

and evidence for sedimentation and potential reheating of the samples are all valuable constraints. Lastly, a distinction must be made between the HeFTy-derived thermal histories for the samples and their exhumation history. Thermal histories in HeFTy only account for sample cooling and apparent constant rates of cooling may represent variable rock exhumation rates owing to spatial and temporal variations in the local geothermal gradient.

6.2 Results

A forward model approach with HeFTy (version 1.8.2) was used to establish the principal shape of tT paths fitting the data, as well as provide boundary constraints for the subsequent model inversions. Because the forward model instantaneously calculates the results, this stage of modeling required relatively little time to complete.

Inverse models were run for all 26 samples, but only 14 of the 26 AHe models and five of the seven ZHe models yielded potential tT paths. Each model was configured with identical boundary constraints and simulation conditions. Because of the suggested influence of considerable alpha-decay damage on the measured cooling ages (as discussed in Chapter 5), the model setup required cogitation of the time and temperature conditions needed to account for the accumulation of lattice defects. Thus, an initial temperature above that of initial alpha-damage accumulation (~150 ºC) was used with sufficient time to yield the oldest observed AHe ages. Thus, each tT path was forced to initiate between 1800-400 Ma at 180-140 ºC (AHe) or 2000-800 Ma at 300-250 ºC (ZHe), and end at 0 Ma (present) between 20-10 ºC. To account for the effects of alpha-recoil damage on diffusion, all models used the Flowers et al. (2009) Radiation Damage Accumulation and Annealing Model (RDAAM) for ^{4}He diffusion kinetics in apatite, and

the Guenthner et al. (2013) Zircon Radiation-Damage Accumulation and Annealing Model (ZRDAAM) for diffusion kinetics in zircon. Under these conditions, HeFTy calculates a theoretical dose of radiation damage for the given tT paths, allowing the ^{4}He-diffusion kinetics to vary with time due to the accumulation of radiation damage within the grains (Flowers et al., 2009; Guenthner et al., 2013). With the aim of providing further tT constraints for the model boundary conditions, three samples were submitted to Apatite-to-Zircon Inc. in November 2013 for supplementary apatite fission-track analysis (AFT), however the results were unavailable at the time of writing.

In total, 14 of the 26 AHe samples yielded 'acceptable' tT paths, although only five of those yielded both 'acceptable' and 'good' fits (Table 3; Figs. 6.1–6.6 – AHe tT paths). ZHe model results yielded 'acceptable' fits for five of the seven samples attempted, three that also achieved 'good' fits (Table 3; Fig. 6.7 – ZHe tT paths). AHe models were conditioned to test 500,000 tT paths, with the exception of samples C008 and B099, which yielded few results after 500,000 attempts. Thus, to allow for comparison with the other model results, samples C008 and B099 were forced to run until 300 'acceptable' fits were achieved. ZHe models required much less attempts to yield fits for the data, with most samples testing between 10,000–100,000 paths; only sample zC008 required additional attempts, and was thereby conditioned to run until qualifying 200 'acceptable' fits.

SAMPLE	Outlier aliquot(s)		HeFTy: omitted grain	HeFTy: fit type
	{He}:eU	{He}:eU/ eU		
C016	–	–	none	acceptable
C008	–	–	mHe5	acceptable
C010	–	n/a	n/a	none
C012	–	mHe3	n/a	none
C013	mHe3	mHe3	mHe3	acceptable
C014	–	n/a	n/a	none
C015	–	n/a	n/a	none
C053	–	n/a	n/a	none
C068	mHe3	mHe3	mHe3	good
C069	–	–	n/a	none
B098	–	n/a	n/a	none
B099	–	–	mHe3	acceptable
B100	–	n/a	none	good
B101	–	n/a	mHe4	acceptable
B102	–	–	mHe3	acceptable
B103	–	–	n/a	none
B105	–	mHe2	mHe2	good
B106	–	–	none	acceptable
K105	–	mHe2	mHe2	good
C001	–	n/a	n/a	none
C003	–	mHe5	none	acceptable
C005	–	mHe4	mHe4	good
C027	n/a	n/a	n/a	none
C028	–	–	n/a	none
Y080	mHe3	mHe3	mHe3	acceptable
zC008	–	–	mHe2	acceptable
zC053	–	n/a	mHe1	acceptable
zC068	–	–	none	good
zC069	–	–	mHe1	good
zB098	mHe3	mHe3	mHe3	good
zC001	–	-	n/a	none
zY080	mHe3	mHe3	n/a	none

Table 3. Summary of aliquot outliers and HeFTy results. Outliers were determined using data reduction plots (see text for discussion). "–" denotes sample with no outliers; "n/a" indicates no distinguishable trend between aliquots, or no HeFTy fits established; mHe# is the aliquot # from the respective sample; "acceptable" vs. "good" represents the statistical quality of the best-fit tT path.

In all AHe model runs, the potential tT paths required relatively slow cooling, though the range of suitable tT paths differed between each sample. Only samples with a range of He cooling ages less than 300 Ma could be modeled. This was attributed to a limited capacity of the RDAAM (AHe) and ZRDAAM (ZHe) to replicate the measured data based on the controlling parameters (e.g., eU, grain size, cooling rate). Because these diffusion models are empirical, and given the apparently extremely high dose of alpha-decay damage in the Hall Peninsula samples, it may be the case that these diffusion models are not suited to explain the end-member scenario of > 300 Ma dispersion observed in the samples. Ergo, to maximize the number of suitable tT paths derived for each sample, it was determined that the most effective strategy was to cull the farthest outlying aliquot age from samples with aliquot ages differing greater than 300 Ma (Ketcham, *pers. comm.*). This strategy assumes that eliminating a single aliquot would only increase the number of potential tT paths, allowing for a greater number of possible tT paths without reducing the capacity of HeFTy to derive tT paths capable of yielding the measured cooling ages. However, because aliquots with large dispersion (i.e., AHe age ∝ eU) can provide valuable information regarding the thermal history (e.g., Flowers, 2009; Flowers et al., 2009), in each sample modeled only one aliquot was removed to avoid obfuscating the relationship between He age and eU. In virtually all cases, the aliquot ages removed in the HeFTy models exhibit anomalous character in the {He}:eU/eU or {He}:eU plots (or both) (Table 3; Figs. 5.15–5.21), suggesting these grains have unidentified secondary controls on their He age (e.g., ^{4}He implantation, chemical composition) and prevent HeFTy from finding suitable cooling paths.

6.2.1 Coastline-perpendicular transect

Model results from the coastline-perpendicular samples provided a range of candidate tT paths. The model results fell between two end-member trends: (1) a cooling history with a well-constrained episode of relatively rapid cooling, followed by prolonged temperatures below 40 ºC (e.g., sample C005), and (2) a monotonic, slowly cooled thermal history with an absence of accelerated cooling and extremely long residence time in the HePRZ (e.g., sample B099). A direct comparison of these two end-member cooling histories suggests they are conflicting, at best, if not entirely incompatible. However, these samples are located at opposite ends of the transect, and, when the results from samples collected in close proximity to one another (Fig. 1.2) are compared, a gradual transition between the two conflicting end member results is observed. To highlight this relationship, nearby samples were divided into four groups based on similarly shaped tT envelopes. Each group (numbered from SW to NE) comprised a single sample with statistically 'good' fits and one or two other samples with 'acceptable' fits, which encompassed the constraints provided by the 'good' fits. Group 1 (samples C005 and C003; Fig. 6.1) yielded constraints supporting rapid cooling from ~80–40 ºC between ca. 360–290 Ma. Group 2 (samples K105 and Y080; Fig. 6.2) produced nearly identical

Figure 6.1. (Next page) HeFTy-derived potential tT envelopes for AHe samples from group 1 from the constant elevation, coastline-perpendicular transect. The results constrain a similar thermal history, with a single, rapid cooling event at ca. 360–290 Ma. Models were conditioned with similar tT constraints. Time-temperature envelopes were established from 500,000 simulated tT paths; the number of "acceptable" and "good" paths are indicated, respectively, by numbers in subtitle. Green colored area indicates area with statistically 'acceptable' tT path determined; magenta colored area indicates statistically 'good' tT path. Black line is best-fit tT path; blue line is weighted-mean path of all 'acceptable' and 'good' fits. All tT paths were required to start between 1800 – 400 Ma and 180 – 140 ºC, indicated by the blue box (bold lines). Results are presented from only 1200 Ma to maintain a discernable scale at relevant times (i.e., 500 Ma – present). See §6.2 for discussion.

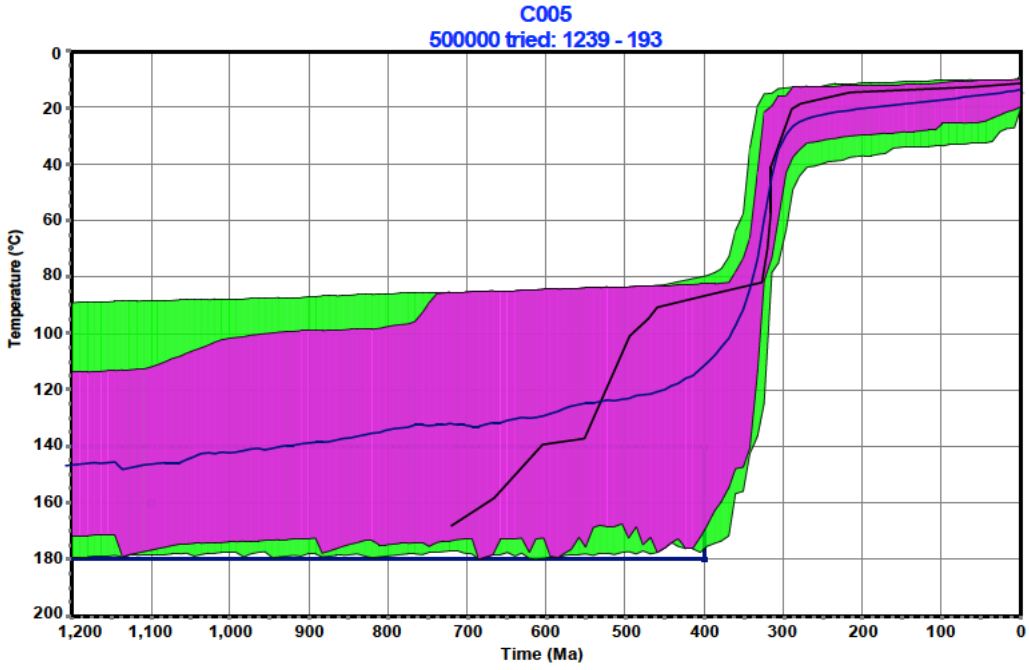

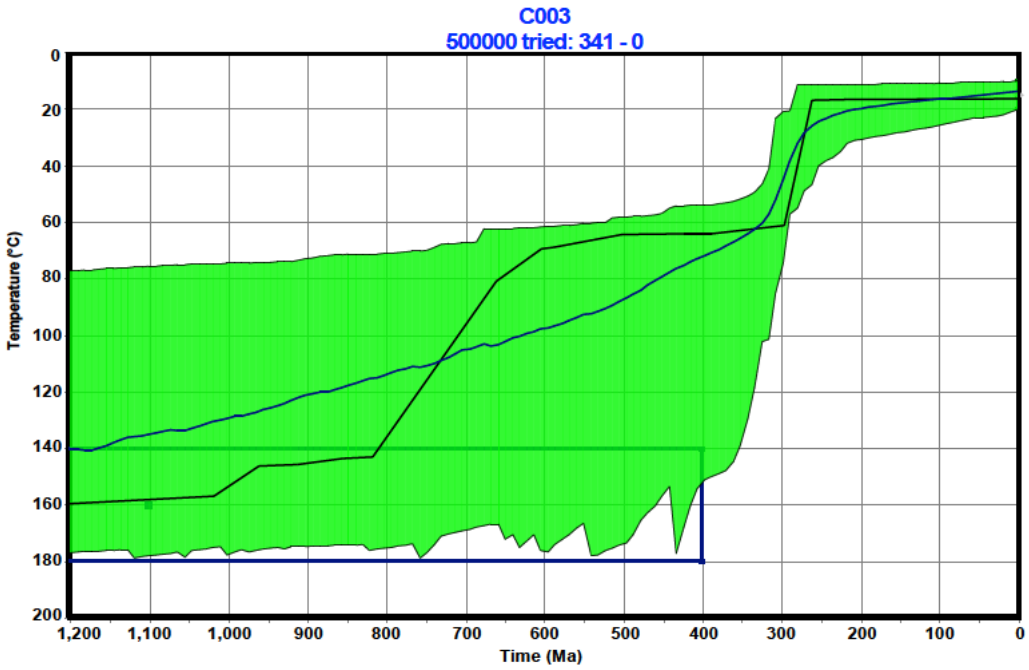

'acceptable' envelopes, and, although poorly constrained before ca. 330 Ma, the low-T history of these samples was more constrained than the others. Since Y080 was the only sample from the coastline-parallel transect to yield suitable tT paths, and the sampled

location is approximately perpendicular to that of K105's position along the transect, it was included in the interpretation of the perpendicular transect results. The samples in group 3 (B102, and B106; Fig. 6.3) yielded comparable constraint envelopes, yet, because these two samples each achieved only 'acceptable' fits, little could be inferred from these results alone. Group 4 **(**samples B101, B100 and B099; Fig. 6.4) yielded nearly identical potential tT envelopes which bottleneck between ca. 450–400 Ma and remain well constrained through ca. 300–250 Ma. The results from sample B105 (Fig. 6.5) were very well-constrained between ca. 600–300 Ma, but these constraints did not entirely overlap with the nearby samples, therefore this sample was not included in group 3 or 4. However, because the grouping of similarly constrained envelopes also coincided with sample proximity for the majority of the samples, it was assumed that the constraints correspond to the actual thermal history, as opposed to being artifacts of the radiation damage.

Figure 6.2. HeFTy-derived potential tT envelopes for AHe samples from group 2 from the constant elevation, coastline-perpendicular transect. The results exhibit nearly identical constraints from ca. 300 Ma to present. Same legend as Fig. 6.1.

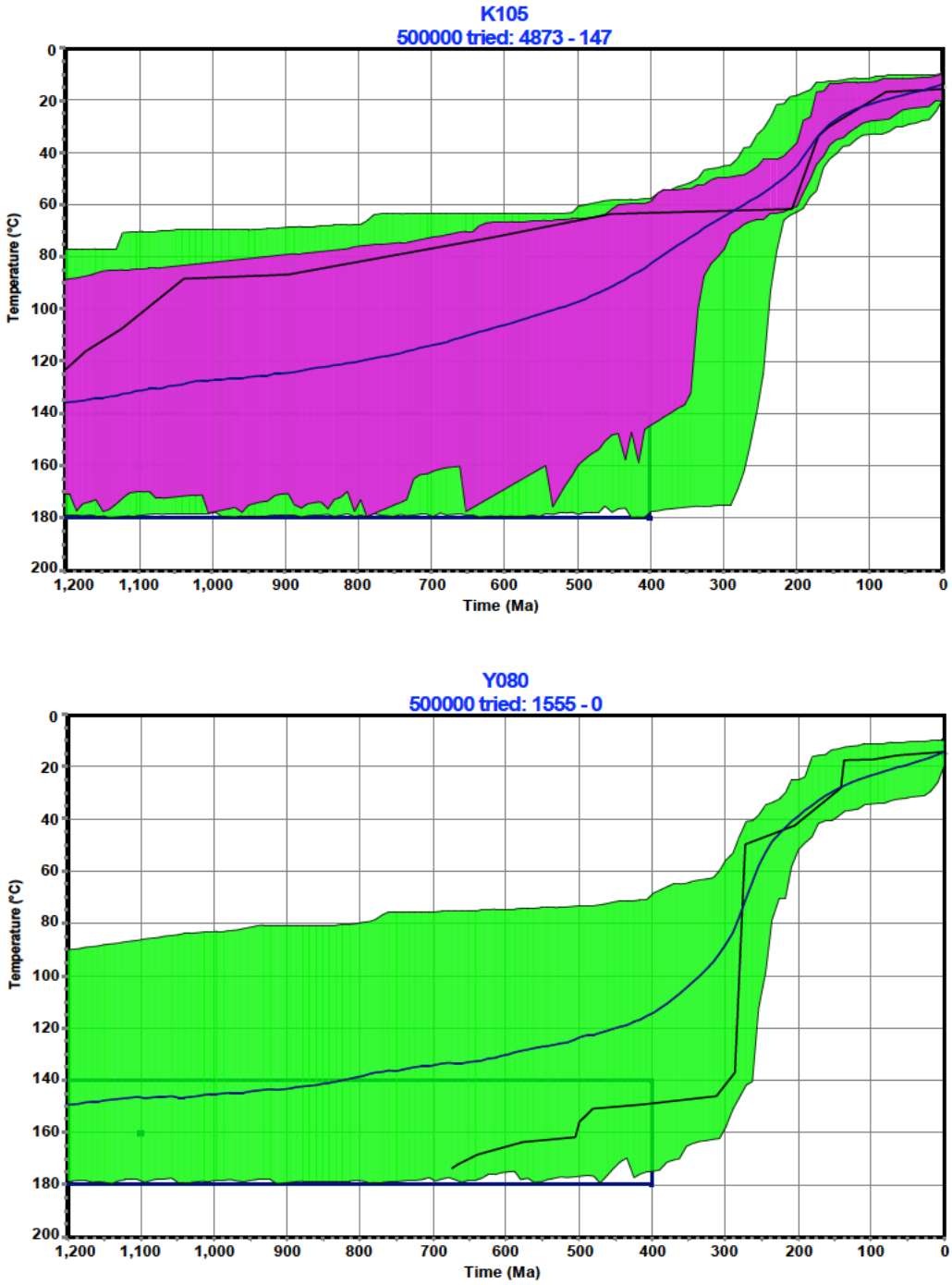

Figure 6.3. HeFTy-derived potential tT envelopes for AHe samples from group 3 from the constant elevation, coastline-perpendicular transect. Samples yielded similar tT envelopes, although no 'good' fits were achieved. Same legend as Fig. 6.1.

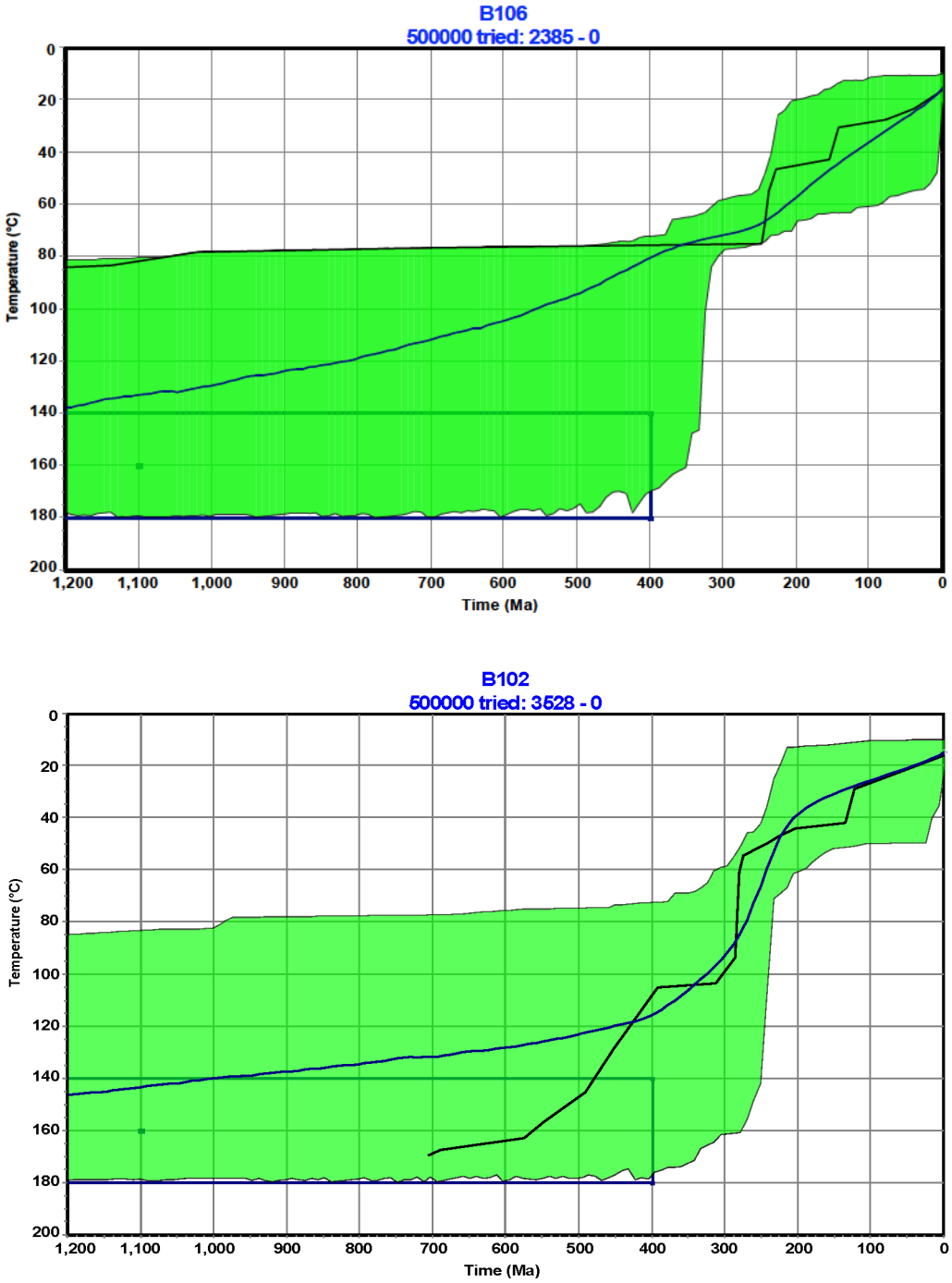

Figure 6.4. HeFTy-derived potential tT envelopes for AHe samples from group 4 from the constant elevation, coastline-perpendicular transect. The tT envelopes indicate Same legend as Fig. 6.1. Sample B099 required a greater number of tT simulations to yield adequate results, and was therefore conditioned to test tT paths until 300 'acceptable' fits were established; subtitle indicates number of paths tried and number of 'good' fits. (Fig. continues on next page).

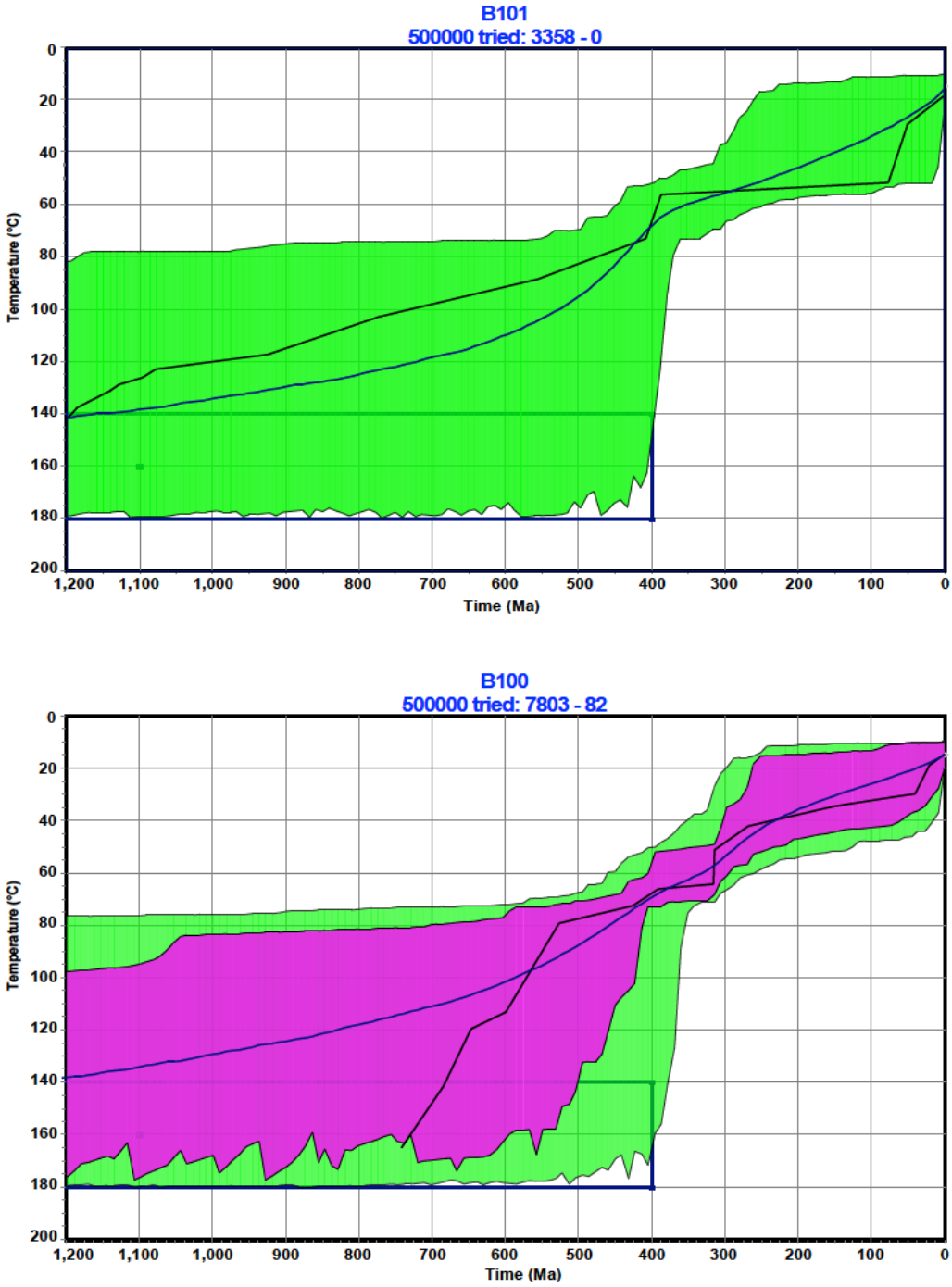

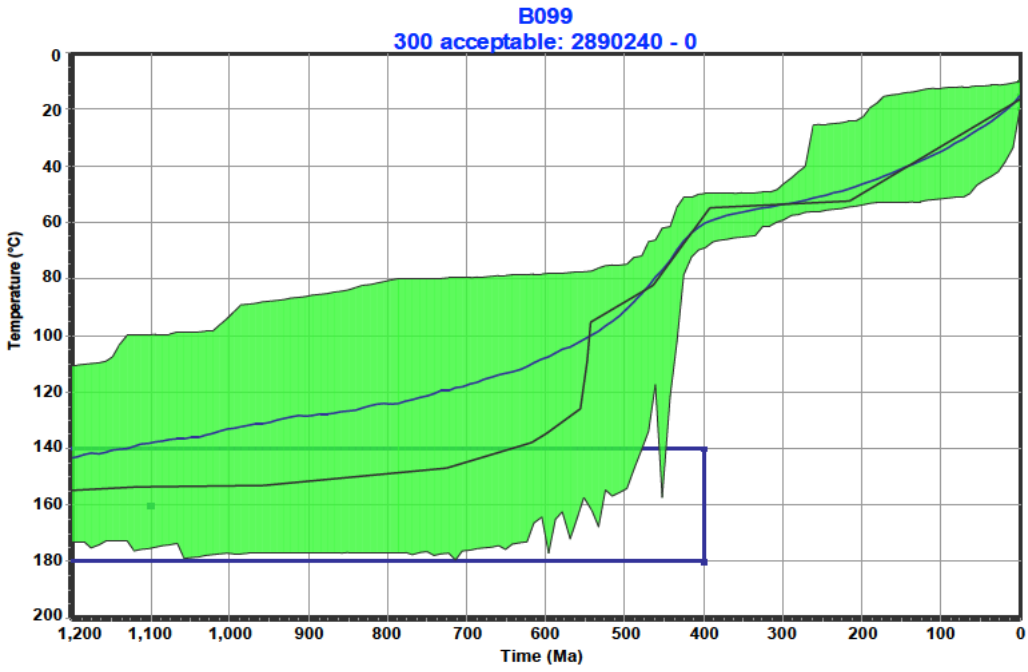

Figure 6.5. (Below) HeFTy-derived potential tT envelopes for AHe sample B105 from the constant elevation, coastline-perpendicular transect. Same legend as Fig. 6.1.

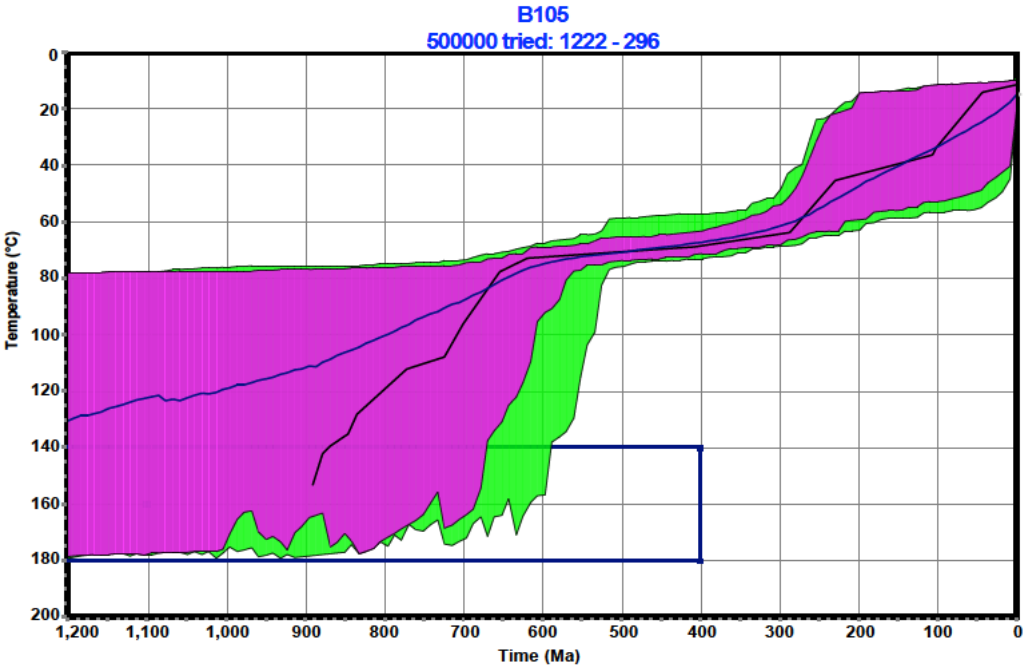

6.2.2 Vertical transect

Few samples from the vertical transect achieved satisfactory fits, and those that did were notably disparate (Fig. 6.6). The inability of HeFTy to determine potential tT paths for most of these samples was likely due to their large range of aliquot cooling ages (many greater than 300 Ma), coupled with the low eU values, which is not a predicted behavior in the RDAAM. For example, according to the RDAAM, the measured AHe age will increase non-linearly with eU; grains with old ages and to equivalent age grains with a high eU, even for similar grain dimensions and thermal histories. With these limitations, a robust cooling age–elevation relationship or exhumed HePRZ (e.g., Centeno, 2005) could not be established.

Figure 6.6. Model results for AHe samples from the vertical transect. All samples yielded tT envelopes consistent with a history of slow cooling. Presented from highest to lowest elevation (Table 2a-c). Same legend as Fig. 6.1. Sample C008 required a increased number of tT simulations to yield adequate results, and was therefore conditioned to test tT paths until 300 'acceptable' fits were established; subtitle indicates number of paths tried and number of 'good' fits. (Fig. continues on next page).

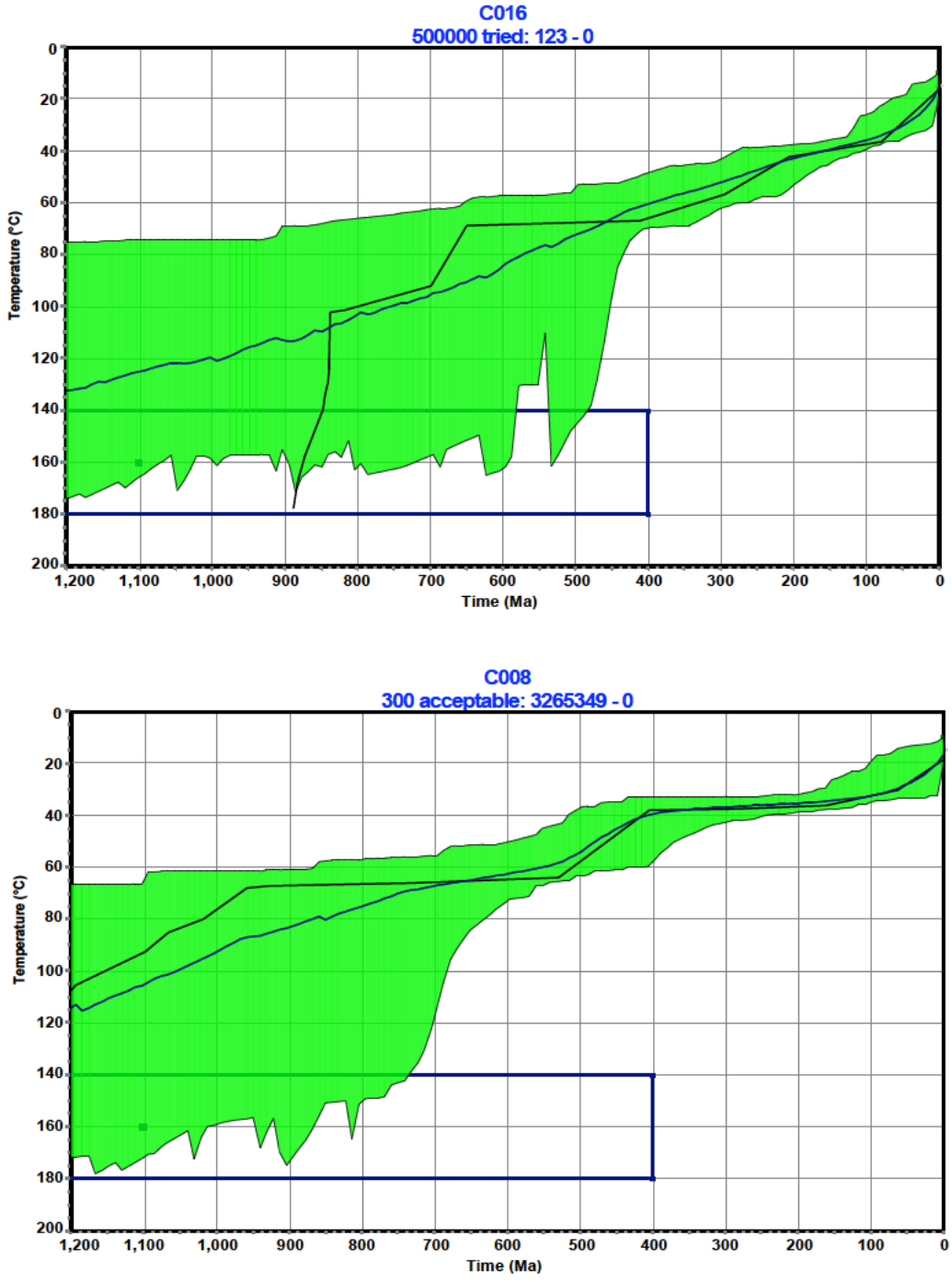

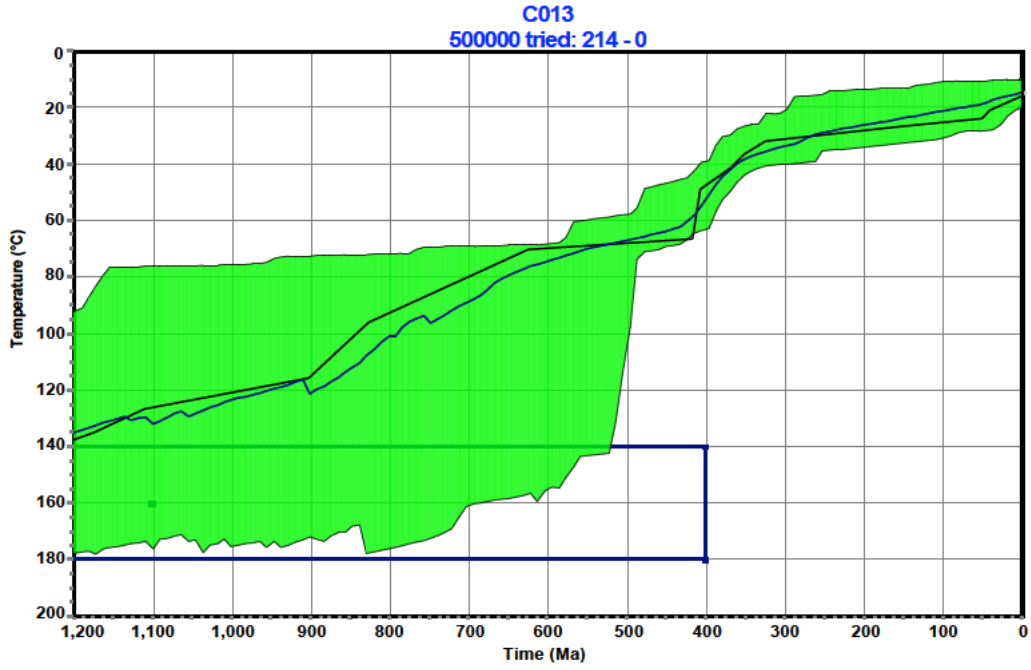
C013
500000 tried: 214 - 0
Temperature (°C)
0
20
40
60
80
100
120
140
160
180
200
1,200
1,100
1,000
900
800
700
600
500
400
300
200
100
0
Time (Ma)

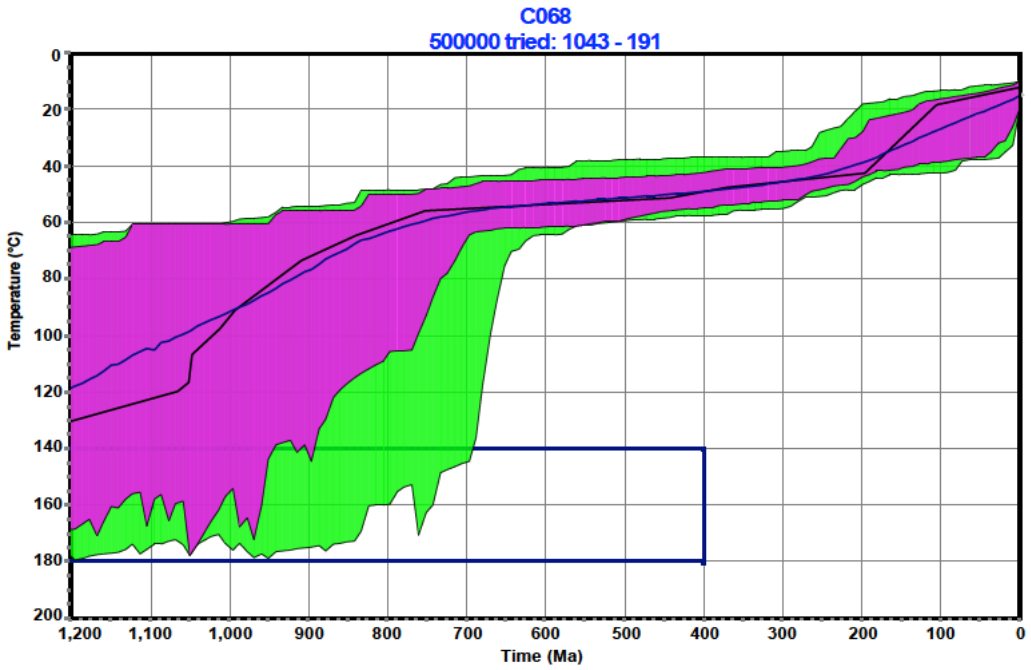
C068
500000 tried: 1043 - 191
Temperature (°C)
0
20
40
60
80
100
120
140
160
180
200
1,200
1,100
1,000
900
800
700
600
500
400
300
200
100
0
Time (Ma)

6.3.3 ZHe data

In contrast to the AHe data, the ZHe data yielded HeFTy models with compatible results from both the perpendicular and vertical transects. All model results exhibited a relatively well-constrained, relatively rapid cooling event (up to 10's of ºC/Ma) involving the samples passing between 140-160 ºC at ~1100-1000 Ma, followed by (and apparently preceded by) exceptionally slow cooling during the Phanerozoic (Fig. 6.7). These results are compatible with that of the AHe models, supporting a scenario with accelerated cooling in the Neoproterozoic, succeeded by a prolonged period of exceptionally slow cooling.

Figure 6.7. HeFTy results for ZHe samples from both the coastline perpendicular transect (zB098) and vertical transect (zC008 – zC069, presented in order of decreasing elevation). Legend same as Fig. 6.1. Time-temperature paths for all samples (except zC008) were forced to initiate between 2000 – 800 Ma and 300 – 250 ºC. Initial starting constraints for sample zC008 were reduced to 1500 – 100 Ma to minimize the time required by HeFTy to establish suitable tT paths. Sample zC008 required a greater number of tT simulations to yield results, and was therefore conditioned to test tT paths until 200 'acceptable' fits were established. However, sample zC069 yielded an abundance of fits, as thus only required 10,000 tT simulations to achieve an adequate number of fits. (Fig. on next two pages).

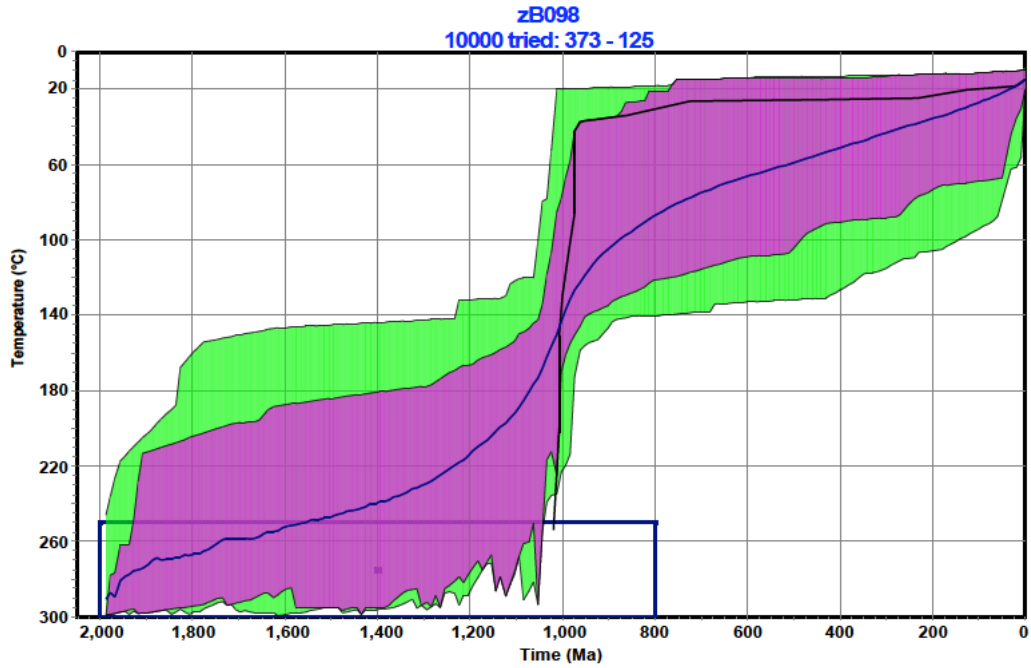

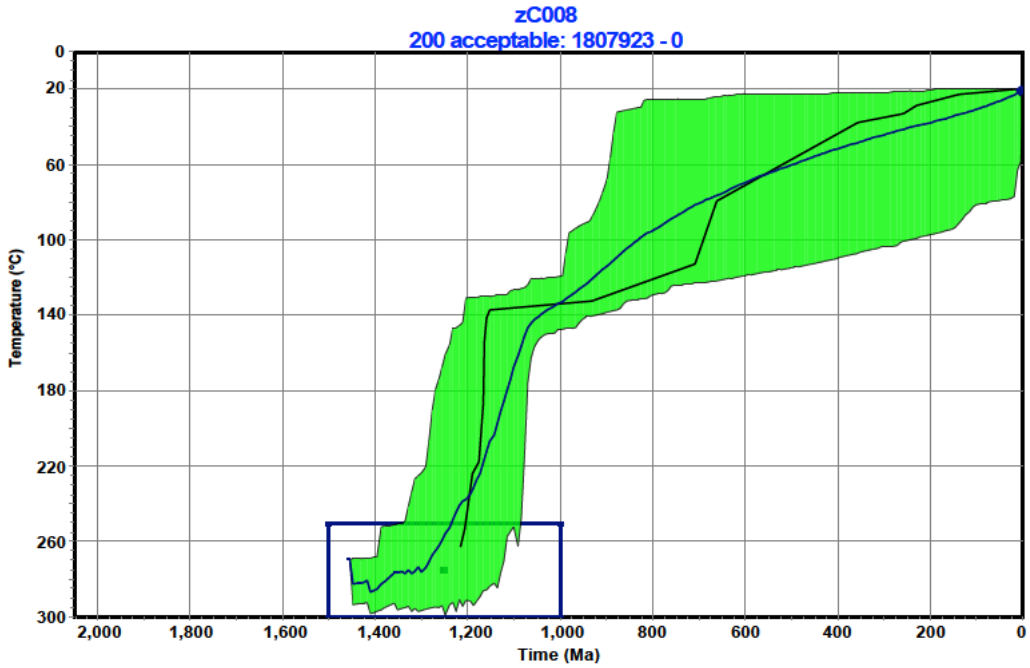
zC008
200 acceptable: 1807923 - 0
Temperature (°C)
0
20
60
100
140
180
220
260
300
2,000
1,800
1,600
1,400
1,200
1,000
800
600
400
200
0
Time (Ma)

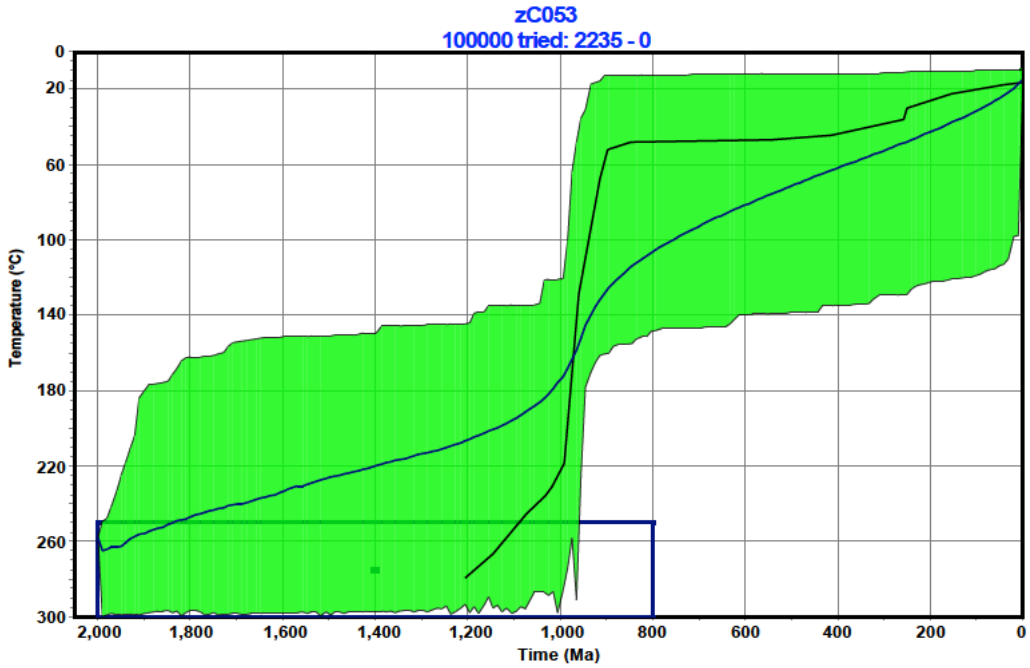
zC053
100000 tried: 2235 - 0
Temperature (°C)
0
20
60
100
140
180
220
260
300
2,000
1,800
1,600
1,400
1,200
1,000
800
600
400
200
0
Time (Ma)

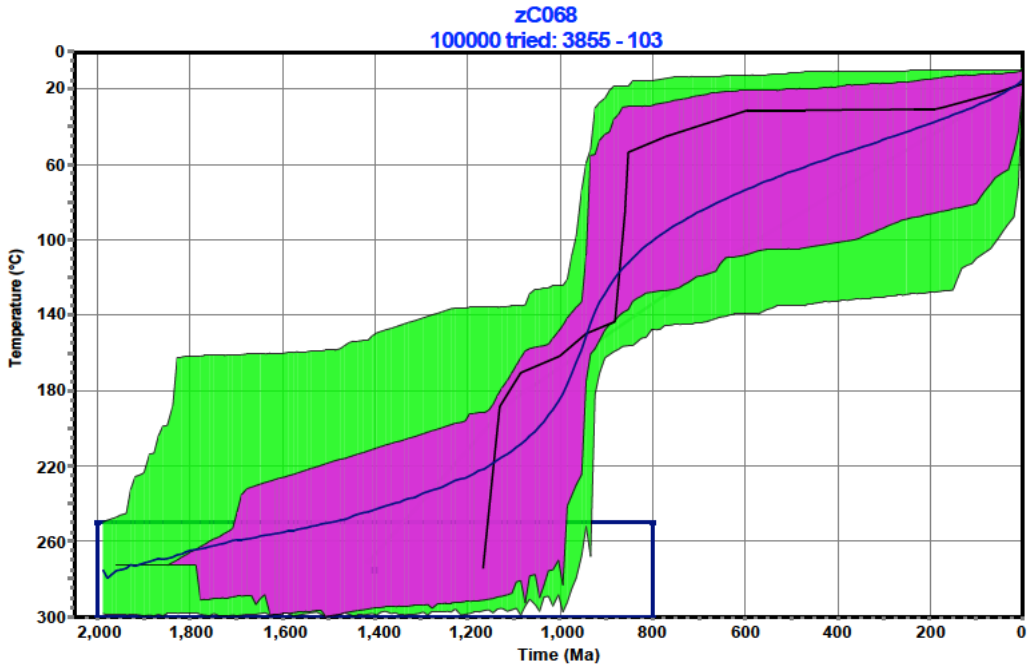
zC068
100000 tried: 3855 - 103
Temperature (°C)
0
20
60
100
140
180
220
260
300
2,000
1,800
1,600
1,400
1,200
1,000
800
600
400
200
0
Time (Ma)

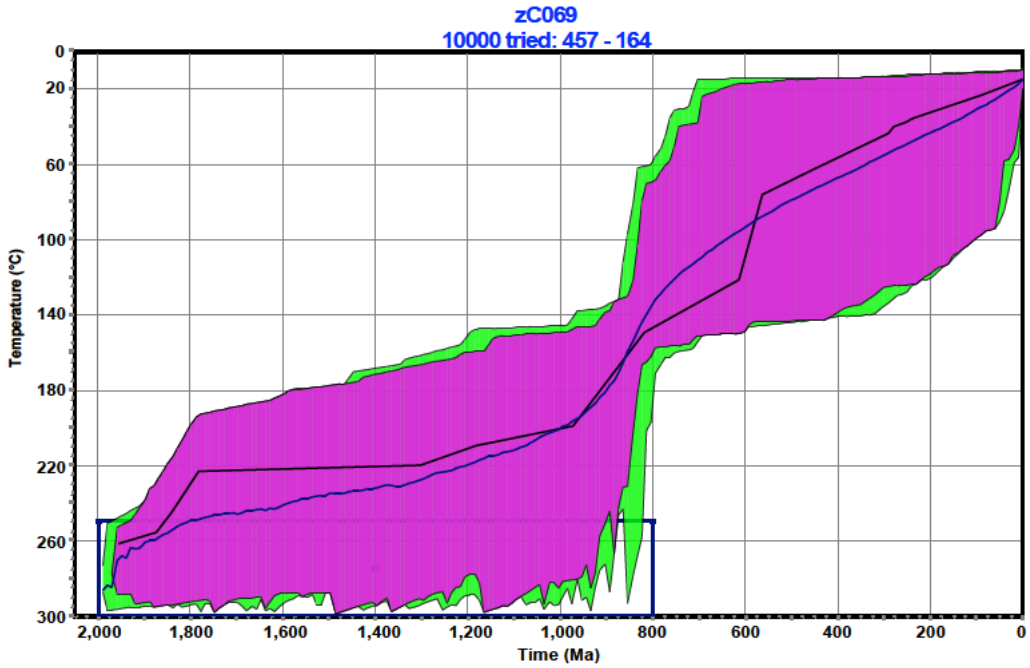
zC069
10000 tried: 457 - 164
Temperature (°C)
0
20
60
100
140
180
220
260
300
2,000
1,800
1,600
1,400
1,200
1,000
800
600
400
200
0
Time (Ma)

6.4 Summary

While the HeFTy results from the vertical transect samples were marginally incompatible with each other, samples from the perpendicular transect yielded a range of constraint envelopes that, when grouped on the basis of proximity to one another, have comparable shapes. In particular, results from the perpendicular transect displayed an E-W progression of the overall trend from slow, consistent cooling paths (e.g., B099, B100, B101) near the NE margin, to a more prominent, relatively rapid cooling in the interior of Hall Peninsula (e.g., C005, C003). By successfully establishing a range of potential tT paths for several samples, the HeFTy output from the samples demonstrated the merit of employing a ^{4}He diffusion model that considers the effects of radiation damage (i.e., Flowers et al., 2009; Gautheron et al., 2009) in order to obtain geologically meaningful thermal and exhumation histories from the data.

CHAPTER 7 – THREE-DIMENSIONAL THERMOKINEMATIC MODELING (PECUBE)

Objective two of this thesis is to reconstruct the three-dimensional (3D) exhumation history of Hall Peninsula to establish potential controls on its landscape evolution. While this can be partially completed with a traditional interpretation of the data and HeFTy output, a more rigorous approach has been developed over the past decade, 3D thermokinematic modeling. This type of modeling involves computing predicted thermochronometric cooling ages for a user-defined tectono-geomorphic scenario in a fully 3D thermal model. It further benefits from the ability to define and test specific scenarios in individual models for an entire dataset, rather than just for individual samples. Furthermore, it inherently allows for testing of three-dimensional problems, such as perturbations geothermal response of time-varying topography. The challenge of this approach is establishing the model constraints, as these models require greater understanding of a sample's cooling history than, for example, a 1D thermal model. Like most models, the output from a thermokinematic approach is not meant to be an exact simulation of the geodynamics and surface processes over the time recorded by the thermochronometers. Instead it allows testing of specific hypotheses and can provide constraints on possible timing and rates of processes and evaluate the relative sensitivity of the thermochronometer data to the various controls considered.

In the eastern Arctic, there are several processes that can control or influence the rate and timing of regional heat transfer. These include (i) crystal cooling resulting from exhumation and upward advection of rock by erosion (note that there is no evidence of widespread low angle detachment faulting or thrusting in the Phanerozoic, so tectonic

exhumation or burial is unlikely); (ii) differential heating or cooling by the flux of hot (e.g., Icelandic plume-related) or cold (meteoric) fluids; (iii) heating by burial under, for example, a thick package of late Paleozoic or Mesozoic sediments; and (iv) vertical displacement caused by slip along new or reactivated faults. To explore the sensitivity of our data to these hypothetical controls, a modified version of the 3D thermokinematic model PECUBE (Braun, 2003) was used.

7.1 Overview of PECUBE

Once potential tT paths were established for the samples, the 3D thermokinematic modeling program PECUBE (version 3; Braun, 2003; Braun et al., 2012) was used to simulate various 3D exhumation scenarios for Hall Peninsula and test their compatibility with the measured data. PECUBE is a finite-element code that is used to solve the heat transport equation. It allows the user to resolve the effects of time-varying topography on the subsurface thermal field, and link together geomorphic and tectonic evolution with the subsurface thermal history (Braun, 2003). Solving the heat transport equation enables the code to 1) define the thermal conditions of the rock particles as they are exhumed to the sample locations at the surface, and 2) calculate the resultant cooling ages for the sample's prescribed exhumation scenario (Braun et al., 2012). As a result, the final output is a spatial distribution of predicted cooling ages for rocks at the surface, as a result of their thermal history (Fig 7.1). Upon comparison to the measured data, the spatial patterns of the modeled cooling ages provide insight into the timing and relative contribution of each exhumation mechanism (i.e., geomorphic versus tectonic factors) in the overall exhumation history. Additionally, PECUBE also calculates

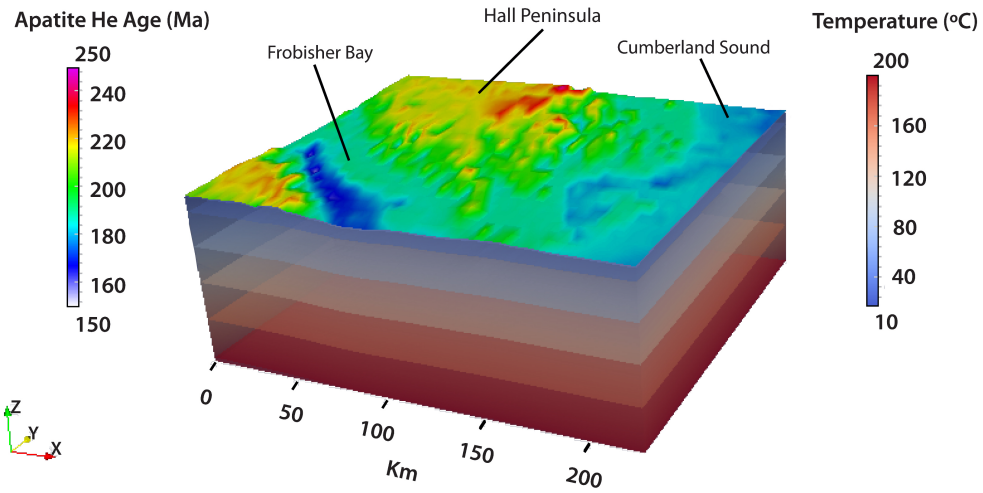

Figure 7.1. Semi-schematic PECUBE model of Hall Peninsula, as viewed in the 3-D visualization program ParaView (Henderson, 2007). Colors at the surface reflect modeled AHe ages, calculated using conventional Durango diffusion kinetics, from a simple exhumation scenario of uniform rock uplift and steady-state topography. Subsurface layers represent planes of equal temperature. Vertical exaggeration (i.e., z-axis) is 5 times, to visibly enhance topography. From Creason and Gosse (2014).

a misfit value for each model, which represents the goodness-of-fit between the modeled ages and measured data. The misfit value is expressed as

$$\boldsymbol{\phi} = \sum_{\boldsymbol{i=1}}^{\boldsymbol{N}} \left(\frac{\boldsymbol{\alpha_{i,mod}} - \boldsymbol{\alpha_{i,dat}}}{\boldsymbol{\sigma_i}} \right)^{\boldsymbol{2}}$$

where ϕ is the misfit value, N is the number of data points (i.e., thermochronological ages), $\alpha_{i,mod}$ and $\alpha_{i,dat}$ are the predicted and observed ages for data point i, respectively, and σ_i is the uncertainty on the data. Ergo, this provides a quantitative supplement for comparing the results of different models.

The PECUBE program is capable of calculating cooling ages for eight different thermochronometers: (U-Th-Sm)/He in apatite and zircon, fission track in apatite and zircon, K-Ar in K-feldspar, and $^{40}Ar/^{39}Ar$ in biotite, muscovite and hornblende. This enables the user to model both the high- and low-temperature thermal evolution of hypothetical geo- and tectono-morphic scenarios, and quantitatively compare the results to measured data.

7.2 Forward versus inverse modeling

Exhumation scenarios are tested in PECUBE through either a forward or inverse modeling approach. Both approaches require the user to define a set of input parameters, variables, and model run time (Table 4), with the models starting at a specified time in the past and evolving to present time according to prescribed variables. For the results, the models provide an output at each user-defined output time step.

When executing a forward model, the program first advects surface sample location points backward in time according to the input velocity field, thereby calculating the 3D position of these rock particles at all times (Braun et al., 2012). PECUBE is then run forward in time while solving the heat equation to calculate the thermal conditions for the particles as they travel to the surface, and outputting the distribution of cooling ages at the surface at the end of each time-step (Braun et al., 2012). Once the model has finished running, the code compares the modeled ages with the measured data using a misfit function and reports the output value. It is then up to the user to assess the model results and manually manipulate the starting conditions or model parameter in the succeeding model runs in order to reduce the misfit value. Because forward models require relatively

Table 4. PECUBE input parameters. Variable parameters were adjusted between model runs, with different combinations of variables present based on the complexity of the scenario; shown here are the input for a model from scenario one. Fault #0 refers to the vertical advection component, as defined at the four corners of the model; in all scenarios, corner velocities were equivalently scaled (i.e., 1, 1, 1, 1 at the corners).
* Thermal conductivity (k) = 1 x 10^{-6} m^2s^{-1}; from Rey et al. (2003).
** Crustal heat production (A) = 5.5 x 10^{-7}; crustal density (ρ) = 2700 kg/km^3; heat capacity (p_c) = 1000; from Perry et al. (2006).

CONSTANT PARAMETERS	
model thickness (km)	25
number of points in z direction	26
thermal diffusivity (km^2/Ma)*	32
temp. at base of model (ºC)	500
temp. at z=0 (ºC)	15
atmospheric lapse rate (ºC/km)	5.4
heat prodcution (ºC/Ma)**	4
spatial resolution (km)	37

VARIABLE PARAMETERS			
Topography input file	start time	topographic amplification	offset factor
	1200	1	1
	750	1	1
	500	1	1
scenario time steps	390	1	1
	375	1	0.5
	360	1	0
	340	1	0
	0	1	0
Fault input file	start	end time	rate
fault timing and velocity	time	(Ma)	(km/Ma
fault #0 (vertical advection)	1200	900	0.1
	900	600	0.1
	600	400	0.005
	400	350	0
fault #1 (Frobisher Bay)	400	370	0.2
fault #2 (Cumberland Sound)	380	350	0.2
number of faults	3		

little processing time (i.e., minutes to hours), this approach is particularly useful for an overall assessment of the first-order controls of the measured distribution of cooling ages, or testing specific exhumation scenarios. Results from the forward models also provide valuable information for the viable range of boundary conditions in the subsequent model inversions.

Inverse modeling is carried out using the Neighborhood Algorithm (NA; Sambridge, 1999a, b) to establish the ranges of parameters that yield a good fit to the measured data. With this approach, the user first defines a range of values for each variable parameter. The modeled scenario is then run repeatedly (as many as 10,000+ times), with each new model involving permutations of all model parameters by selection of values "close" to those that previously fit the data well. At the end of each run, the NA assesses the previous misfit results and uses this information as a guide for optimizing parameter selection in the subsequent runs. The final product is an output set of probability density functions for the model parameters defining the ranges that yield cooling ages similar to the measured data.

7.3 Model design

When designing a PECUBE model, the user must define the spatial extent of the model (which should be sufficiently large to avoid any effects from the model boundaries), how topography evolves (e.g., steady-state vs. evolving), variations in rock exhumation rate, timing and total offset of any faults, as well as the rock thermo-physical properties (e.g., density, thermal conductivity or diffusivity, and heat production). Once defined, the model parameters are input using two different files: a topographic parameter file, and a fault parameter file (Table 4). The topography parameter file comprises

definition of the digital elevation model, evolution of topography, thermochronometer data, model (crustal) thickness, and rock thermo-physical properties. The topography for the PECUBE models presented below was taken from Canvec 50K topographic data (provided by the CNGO during the summer of 2102) using the Spatial Analyst Tool in ArcGIS. In all models the thermo-physical properties and model dimensions were assumed to be constant (Table 4). Owing to the deficiency of published data from Baffin Island, values for the thermal diffusivity and heat production were based on observed values from the Superior Province (Perry et al., 2006; Rey et al., 2003). The geothermal gradient at the model start (t = 0) was set conservatively at 20 ºC/km, similar to what has been used for cratonic settings elsewhere (e.g., Ault et al., 2009). However, since almost any change in the physical model (e.g., change in exhumation rate, incision, change in heat advection associated with faulting, or local heat flow changes owing to hydrothermal events and rifting) can perturb this gradient at different regions of the modeled crustal block, this initial condition evolves during the model run. The fault parameter file defines the exhumation velocity field, and, if faults are present, the timing and kinematics of fault motion. Given the slow cooling histories established by the HeFTy modeling, relatively slow average exhumation rates were tested in the PECUBE models, with most average exhumation rates between 10–20 m/Ma during the Phanerozoic.

7.3.1 Modification to incorporate alpha-recoil damage in predicted apatite (U-Th-Sm)/He ages

To account for the effects of time-varying diffusion in the AHe thermochronometer, the Gautheron et al. (2009) model for radiation-damaged diffusion was incorporated into Pecube, using code that was previously developed and employed by Valla et al. (2012). This modified version of PECUBE maintains a workflow similar to that of the

unmodified version (Ver. 3), as it still calculates 'preliminary' AHe ages for the each tT path using conventional Durango apatite kinetics (Farley, 2000). However, once the model is finished, the modified code re-calculates 'corrected' AHe ages for the sample points that include the effects of the accumulation of alpha-recoil damage on ^{4}He diffusion as outlined by Gautheron et al. (2009). Since the alpha-decay dose is proportional to the eU concentration, and hence requires input of the eU, U/Th ratio and effective spherical grain radius (ESR) for each age calculation, AHe ages that incorporate this effect are recalculated only for the sampled locations; all other AHe ages are calculated with conventional Durango apatite kinetics. Therefore, it is not possible to assess the model quality based on the distribution of cooling ages across the entire surface of the model. Instead, the misfit value and trends observed the predicted ages serve as the primary means to evaluate the fit of a given set of model parameters to the data.

7.3.2 Modeling approach for Hall Peninsula

The PECUBE models included the same samples (grains) that yielded good and/or acceptable fits in the HeFTy models, which totaled 60 grains (Table 3). Each grain age was input as an individual rock particle. Apatite fission-track ages were also modeled to compare the results of two different low-temperature thermochronometers.

Although the effects of recoil-damage were considered in the AHe age calculations, it was difficult to produce a set of predicted cooling ages with comparable variability in the observed ages owing to the large range of cooling ages among aliquots in a given sample. It was thus foreseen that inversion of the age data with PECUBE would not have provided further insight into the range of physical parameters that have controlled cooling of the observed age data. It was presumed that, had model inversions been performed, the

complex nature of the data (i.e., scattered aliquot ages) likely would have yielded a range of (non-unique) solutions, rendering the NA ineffective in characterizing the good-fitting regions of parameter space, and, thus, unsuccessful at establishing robust, clear parameter ranges. Therefore, given the time-intensive nature of running inverse models (days to weeks), the use of PECUBE in this study was limited to only forward modeling.

After running a series of preliminary models to test the functionality of the modified diffusion kinetics in predicting dispersed AHe ages, it became clear that several different hypotheses could be considered in the scope of this thesis. The most straightforward of these hypotheses was that Hall Peninsula experienced increased rates of exhumation in the Late Cretaceous to Paleocene as a result of transtension and separation from Greenland, or extension from Cumberland Peninsula. Likewise, exhumation scenarios modeled after studies from the West Greenland margin, which involve more recent episodes of exhumation (e.g., Neogene uplift; Japsen et al., 2006), were deemed testable. However, given the time constraints of the project, and the HeFTy results that indicate slow cooling throughout the Cenozoic, the most appropriate first-order question that can be addressed is whether the measured data contain evidence of the reactivation of faults, which may have caused Hall Peninsula to evolve as a half graben (with a southward dip) sometime during the Mesozoic or Paleozoic.

All models were initiated at 1200 Ma and evolved with present day topography. The 1200 Ma start was chosen because this was the earliest tT constraint provided by the ZHe HeFTy models (Fig. 6.3), and thus the earliest constraint on the thermal history.

7.4 PECUBE Results

In order to justify inclusion of the various exhumational constraints in the models (i.e., presence of faults, change in surface elevation, episodes of accelerated exhumation), five tectonomorphic scenarios of different complexity were tested (Table 5). Multiple models were tested for each scenario, with select input parameters adjusted incrementally between runs to determine their influence on the misfit. Model adjustments were aimed at minimizing the misfit value, such that if an adjustment resulted in increasing the misfit value, the adjustment was deemed as reducing the model 'goodness-of-fit' for the particular scenario, and subsequent adjustments were made accordingly. Testing of each scenario ceased once adjustment of the select parameters no longer reduced the misfit (i.e., misfits converged on a minimum value).

Forty-six models were used to test various parameter configurations for the five different scenarios. The configurations are summarized in Table 5. The most complex scenario (1) involved a highly variable exhumation rate, with a phase of particularly accelerated exhumation, vertical offset of topography, and fault motion along two normal faults located within Frobisher Bay (F1) and Cumberland Sound (F2) (Fig. 7.2). The models for this scenario tested different permutations of the timing and amount of fault offset, timing of changes in the exhumation rate, and total exhumation. Misfit values for these models range between 4448–5777. Scenario 2 maintained a similar features to

Table 5. (Next page) Summary of different scenarios tested in PECUBE. The scenarios differ by their complexity (e.g., presence of faults, timing of changes in exhumation rate), as well as number of models simulated, the ranges in which the parameters were varied, and the corresponding range of misfits. F_1 and F_2 are normal faults in Frobisher Bay and Cumberland Sound, respectively. Individual modeled AHe ages from the lowest misfit model from each scenario are presented in Tables 6a–6e.

	Scenario 1	Scenario 2	Scenario 3	Scenario 4	Scenario 5
Features:	decrease in surface elevation, faulting, period of accelerated exhumation	decrease in surface elevation, faulting, period of accelerated exhumation	decrease in elevation, period of extremely rapid exhumation	period of rapid vertical exhumation, otherwise slow exhumation	slow, vertical exhumation
Number of models:	15	6	5	13	7
Parameters varied between models:	exhumation rate, timing and duration of faulting,	exhumation rate, timing of accelerated exhumation, surface elevation	exhumation rate, surface elevation	exhumation rate, timing of period of accelerated exhumation	exhumation rate
F_1:	0 – 200 m/Ma between 400 – 370 Ma;	none	none	none	none
F_2:	0 – 500 m/Ma between 365 – 355 Ma	0 – 100 m/Ma between 440 – 430 Ma	none	none	none
Topographic offset:	from 1000 m offset, decrease by 33.3 m/Ma during 390 – 360 Ma	from 1000 m offset, decrease by 33.3 m/Ma during 390 – 360 Ma	from 1000 m offset, decrease by 0 – 33.3 m/Ma during 390 – 360 Ma	none	none
Vertical rock advection:	1200 – 900 Ma: 50 – 100 m/Ma	1200 – 900 Ma: 50 m/Ma	1200 – 900 Ma: 50 m/Ma	1200 – 900 Ma: 50 m/Ma	1200 – 900 Ma: 50 m/Ma
	900 – 600 Ma: 20 – 50 m/Ma	900 – 600 Ma: 20 m/Ma	900 – 600 Ma: 20 m/Ma	900 – 600 Ma: 20 m/Ma	900 – 600 Ma: 20 m/Ma
	600 – 400 Ma: 10 – 20 m/Ma	600 – 400 Ma: 10 – 20 m/Ma	600 – 450 Ma: 15 m/Ma	15 m/Ma: between 600 – 450 / 350 / 300 / 250 / 200 Ma	600 – 0 Ma: 8 – 10 m/Ma
	400 – 350 Ma: 20 – 100 m/Ma	400 – 350 Ma: 20 – 100 m/Ma	450 – 400 Ma: 50 – 700 m/Ma	50 m/Ma: between 450-400 / 400-350 / 350-300 / 300-250 / 250-200 / 200-150 Ma (respectively)	–
	350 – 0 Ma: 7 – 9 m/Ma	350 – 0 Ma: 7 – 9 m/Ma	400 – 0 Ma: 7 – 9 m/Ma	6-8 m/Ma: between 400-350 / 350-300 / 300-250 / 250-200 / 200-150 / 150-100 Ma (respectively)	–
Misfits:	4448 – 5777	4526 – 6160	4764 – 6554	4432 – 6222	4355 – 5128
Mean modeled AHe age (Ma):	264.53 – 318.86	297.19 – 324.63	300.09 – 330.76	246.97 – 328.15	251.65 – 311.86

scenario 1, although only a single fault (in Cumberland Sound) was simulated. Adjustments in the models of scenario 2 involved modification of both the rate of fault offset and timing of changes in the exhumation rate, yielding model misfit values between 4526–6160. The less complex scenarios (3 and 4) entailed less variation in the exhumation rate and no faulting or decrease in the vertical offset of topography, while retaining an episode of accelerated exhumation. Only two parameters were adjusted in the scenario 3 models; the rate of exhumation during the accelerated phase, which ranged between 50–700 m/Ma from 450–400 Ma, and the exhumation rate during the final time step, which ranged between 7–9 m/Ma. The scenario 4 models featured similar complexity, but instead the exhumation rate during this accelerated phase was held constant (at 50 m/Ma) and the timing of the 50 Myr phase varied between 450–400 to 200–150 Ma. The models from scenarios 3 and 4 yielded misfit values between 4764–6554 and 4432–6222, respectively. Finally, the most basic scenario (5) involved steady state topography with simple (vertical) exhumation and no faulting. The only adjustment parameter adjusted in these models was the exhumation rate during the final time step (600–0 Ma), which ranged between 7–9 m/Ma. Models from this scenario yielded misfits between 4355 – 5128.

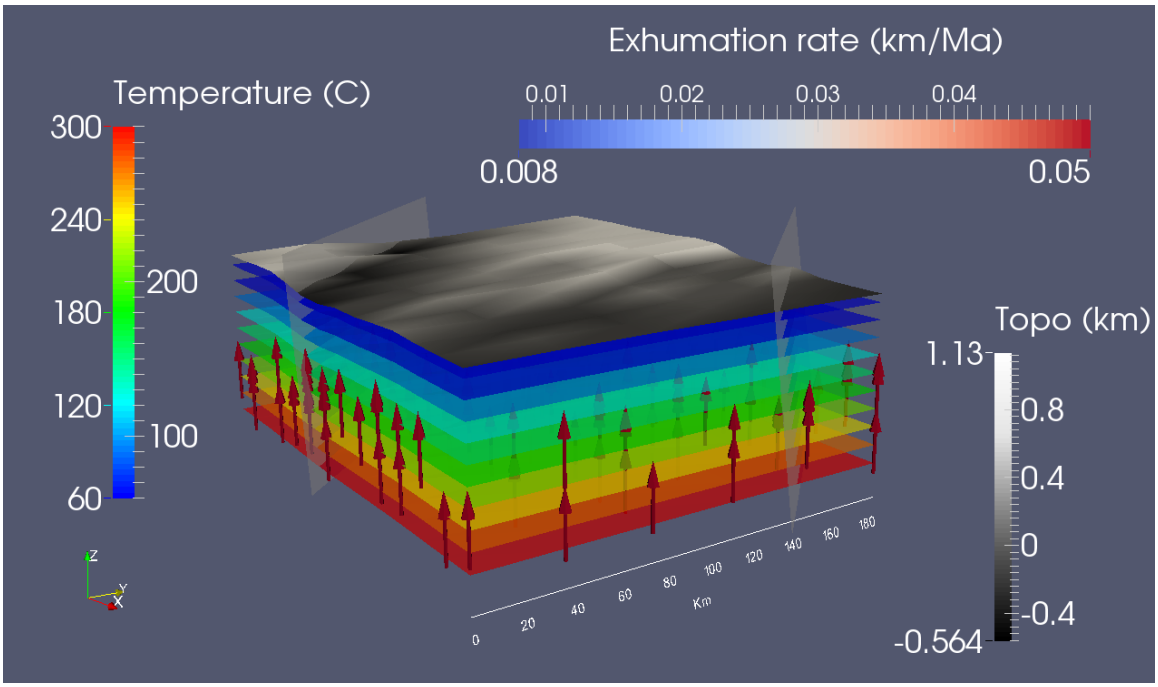

Figure 7.2. PECUBE model output at time step 5 (360 Ma) from scenario 1. Vertical exaggeration is 5 times. Colors at the surface indicate elevation above modern sea level. To minimize processing time, the scenarios were run at a topographic skipping factor of 20, meaning that only one of every 20 points were calculated. Location and orientation of fault planes in Frobisher Bay (left) and Cumberland Sound (right) shown for reference; faults are inactive during this time step.

7.4.1 Summary of scenario results

In general, the models display a high sensitivity to adjustments in the exhumation rate during the final time step (e.g., 350-0 Ma, 250-0 Ma, or 450-0 Ma), yielding markedly higher misfits for exhumation rates ≤ 0.007 km/Ma (scenarios 2, 3 and 4). Interestingly, models with a presence of faulting activity (scenarios 1 and 2) or periods of accelerated exhumation (50 m/Ma) prior to ~ 400 Ma (scenario 4) yield similar misfits to the other, less complex models. In fact, the lowest overall misfit of 4355 was achieved in scenario 5 (model RD023_BL; Table 6a), by a model that simulated a fixed exhumation rate of 0.0088 km/Ma from 600-0 Ma with no faulting. Scenario 5 also achieved the next three

lowest misfits, however the minimum misfits from the other scenarios only differed from the overall lowest by less than 10%. Notably, the modeled AFT ages do not coincide with the AHe ages in all of the scenarios (Table 6a-e). Unlike the similar range of AHe ages found in all scenarios, the AFT ages differ between the various exhumation scenarios, yielding younger ages in the rapidly exhumed scenarios (1 and 2) and older ages in the more slowly exhumed scenarios (4 and 5).

Table 6a. Lowest misfit model results from scenario 1 (model RD023_06), with a misfit of 4448.

Sample	Sample elevation (m)	Interpolated elevation (m)	Exhumation rate (km/Ma)	Measured AHe age (Ma)	Modeled AHe age (Ma)	Age difference (Ma)	Modeled AFT age (Ma)	eU (ppm)	ESR (μm)	U:Th
B099-1	252.0	21.7	0.008	373.7	322.5	51.2	46.1	24.52	112.18	12.29
B099-2	252.0	21.7	0.008	334.8	298.5	36.3	46.1	18.30	75.77	13.15
B099-4	252.0	21.7	0.008	412.5	323.7	88.8	46.1	23.92	84.16	10.64
B099-5	252.0	21.7	0.008	369.2	293.6	75.6	46.1	20.82	68.93	8.78
B100-1	244.3	15.0	0.008	332.5	277.7	54.8	46.1	14.52	57.21	4.03
B100-2	244.3	15.0	0.008	327.8	275.4	52.4	46.1	27.12	42.21	5.46
B100-3	244.3	15.0	0.008	362.8	309.1	53.7	46.1	26.36	60.01	5.28
B100-4	244.3	15.0	0.008	375.7	318.3	57.4	46.1	26.36	82.76	4.51
B100-5	244.3	15.0	0.008	313.5	295.7	17.8	46.1	17.90	54.34	5.15
B101-1	269.9	14.5	0.008	371.4	312.1	59.4	46.1	26.54	62.57	6.37
B101-2	269.9	14.5	0.008	367.8	320.3	47.6	46.1	34.38	67.04	4.14
B101-3	269.9	14.5	0.008	303.4	296.3	7.1	46.1	18.63	59.03	5.16
B101-5	269.9	14.5	0.008	348.7	293.3	55.4	46.1	18.56	68.83	5.75
B102-1	246.6	19.8	0.008	238.8	301.5	-62.6	46.1	27.09	65.62	26.07
B102-2	246.6	19.8	0.008	222.4	293.5	-71.0	46.1	20.91	56.81	12.54
B102-4	246.6	19.8	0.008	232.1	301.8	-69.7	46.1	17.43	68.95	10.26
B102-5	246.6	19.8	0.008	253.6	304.1	-50.5	46.1	18.47	72.83	13.20
B105-1	236.0	24.5	0.008	307.3	297.7	9.6	46.1	12.95	70.66	5.88
B105-3	236.0	24.5	0.008	526.8	343.3	183.5	46.1	50.81	93.32	2.52
B105-4	236.0	24.5	0.008	395.8	313.2	82.6	46.1	24.74	76.32	5.04
B105-5	236.0	24.5	0.008	522.8	328.8	194.0	46.1	50.70	76.22	3.16
B106-1	249.8	71.8	0.008	250.7	310.9	-60.2	46.1	34.41	70.20	0.53
B106-2	249.8	71.8	0.008	302.9	314.4	-11.6	46.1	52.84	60.85	0.47
B106-3	249.8	71.8	0.008	269.9	307.5	-37.6	46.1	46.82	51.73	0.42
B106-4	249.8	71.8	0.008	319.5	320.3	-0.8	46.1	72.01	72.01	0.02
B106-5	249.8	71.8	0.008	270.9	308.4	-37.5	46.1	32.93	57.26	0.38
C003-1	326.5	445.4	0.008	309.7	271.8	37.9	46.1	7.29	47.15	7.67
C003-2	326.5	445.4	0.008	312.3	250.2	62.1	46.1	4.12	40.79	3.79
C003-3	326.5	445.4	0.008	305.8	265.6	40.2	46.1	4.56	44.39	2.18
C003-4	326.5	445.4	0.008	308.0	254.7	53.3	46.1	5.12	42.70	5.87
C003-5	326.5	445.4	0.008	278.1	266.6	11.5	46.1	4.00	56.77	6.72
C005-1	397.0	491.8	0.008	331.8	328.7	3.1	46.1	123.11	52.85	6.76
C005-2	397.0	491.8	0.008	348.0	341.8	6.2	46.1	125.18	81.75	13.71
C005-3	397.0	491.8	0.008	321.6	337.6	-16.0	46.1	54.63	50.02	16.64
C005-5	397.0	491.8	0.008	322.8	280.5	42.3	46.1	11.13	50.71	13.70
K105-1	266.9	335.3	0.008	206.6	276.2	-69.6	46.1	5.01	63.99	13.13
K105-3	266.9	335.3	0.008	235.4	280.4	-45.0	46.1	7.80	51.99	4.90
K105-4	266.9	335.3	0.008	203.6	272.3	-68.7	46.1	4.05	61.04	10.00
K105-5	266.9	335.3	0.008	190.7	248.9	-58.2	46.1	2.58	55.85	3.20
Y080-1	12.9	43.8	0.008	193.4	261.0	-67.6	46.1	5.02	62.22	5.63
Y080-2	12.9	43.8	0.008	223.0	279.5	-56.5	46.1	3.97	84.57	8.40
Y080-4	12.9	43.8	0.008	214.0	273.1	-59.1	46.1	4.91	60.75	6.29
Y080-5	12.9	43.8	0.008	243.0	295.8	-52.9	46.1	16.74	69.95	35.68
C008-1	685.1	263.6	0.008	482.1	282.4	199.7	46.1	5.86	67.05	0.89
C008-2	685.1	263.6	0.008	356.3	247.1	109.2	46.1	2.00	60.98	1.54
C008-3	685.1	263.6	0.008	269.5	249.2	20.2	46.1	1.11	82.72	2.42
C008-4	685.1	263.6	0.008	469.6	269.6	200.0	46.1	4.85	56.67	1.43
C013-1	375.0	245.2	0.008	395.2	276.6	118.6	46.1	10.52	53.69	2.29
C013-2	375.0	245.2	0.008	513.7	293.9	219.8	46.1	28.32	44.21	0.61
C013-4	375.0	245.2	0.008	439.6	268.3	171.2	46.1	7.87	44.42	2.08
C013-5	375.0	245.2	0.008	335.7	243.4	92.3	46.1	3.01	47.74	1.57
C016-1	794.2	322.6	0.008	201.6	267.5	-65.9	46.1	2.23	77.35	12.59
C016-2	794.2	322.6	0.008	164.6	257.4	-92.8	46.1	1.60	85.80	2.78
C016-3	794.2	322.6	0.008	210.7	256.0	-45.3	46.1	4.19	53.44	8.71
C016-4	794.2	322.6	0.008	221.3	278.3	-57.0	46.1	2.74	78.58	10.37
C016-5	794.2	322.6	0.008	233.9	276.0	-42.1	46.1	3.43	76.68	13.52
C068-1	114.0	335.3	0.008	593.1	287.5	305.7	46.1	7.32	67.40	2.28
C068-2	114.0	335.3	0.008	603.5	283.6	319.9	46.1	7.62	66.00	2.19
C068-4	114.0	335.3	0.008	276.7	238.5	38.2	46.1	2.21	44.74	1.23
C068-5	114.0	335.3	0.008	407.2	257.9	149.4	46.1	3.90	54.62	1.63

Table 6b. Lowest misfit model results from scenario 2 (model RD023_M), with a calculated misfit of 4526.

Sample	Sample elevation (m)	Interpolated elevation (m)	Exhumation rate (km/Ma)	Measured AHe age (Ma)	Modeled AHe age (Ma)	Age difference (Ma)	Modeled AFT age (Ma)	eU (ppm)	ESR (µm)	U:Th
B099-1	252.0	21.7	0.008	373.7	340.2	33.5	139.4	24.52	112.18	12.29
B099-2	252.0	21.7	0.008	334.8	324.3	10.5	139.4	18.30	75.77	13.15
B099-4	252.0	21.7	0.008	412.5	327.0	85.6	139.4	23.92	84.16	10.64
B099-5	252.0	21.7	0.008	369.2	310.6	58.6	139.4	20.82	68.93	8.78
B100-1	244.3	15.0	0.008	332.5	290.3	42.2	139.4	14.52	57.21	4.03
B100-2	244.3	15.0	0.008	327.8	294.0	33.8	139.4	27.12	42.21	5.46
B100-3	244.3	15.0	0.008	362.8	315.5	47.3	139.4	26.36	60.01	5.28
B100-4	244.3	15.0	0.008	375.7	322.8	52.9	139.4	26.36	82.76	4.51
B100-5	244.3	15.0	0.008	313.5	301.0	12.4	139.4	17.90	54.34	5.15
B101-1	269.9	14.5	0.008	371.4	319.0	52.5	139.4	26.54	62.57	6.37
B101-2	269.9	14.5	0.008	367.8	328.7	39.1	139.4	34.38	67.04	4.14
B101-3	269.9	14.5	0.008	303.4	297.6	5.8	139.4	18.63	59.03	5.16
B101-5	269.9	14.5	0.008	348.7	317.4	31.4	139.4	18.56	68.83	5.75
B102-1	246.6	19.8	0.008	238.8	320.0	-81.1	139.4	27.09	65.62	26.07
B102-2	246.6	19.8	0.008	222.4	308.0	-85.6	139.4	20.91	56.81	12.54
B102-4	246.6	19.8	0.008	232.1	310.4	-78.3	139.4	17.43	68.95	10.26
B102-5	246.6	19.8	0.008	253.6	314.8	-61.2	139.4	18.47	72.83	13.20
B105-1	236.0	24.5	0.008	307.3	306.3	1.0	139.4	12.95	70.66	5.88
B105-3	236.0	24.5	0.008	526.8	340.9	186.0	139.4	50.81	93.32	2.52
B105-4	236.0	24.5	0.008	395.8	329.8	66.0	139.4	24.74	76.32	5.04
B105-5	236.0	24.5	0.008	522.8	347.4	175.5	139.4	50.70	76.22	3.16
B106-1	249.8	71.8	0.008	250.7	317.6	-67.0	139.4	34.41	70.20	0.53
B106-2	249.8	71.8	0.008	302.9	334.4	-31.5	139.4	52.84	60.85	0.47
B106-3	249.8	71.8	0.008	269.9	319.6	-49.7	139.4	46.82	51.73	0.42
B106-4	249.8	71.8	0.008	319.5	334.3	-14.8	139.4	72.01	54.48	0.02
B106-5	249.8	71.8	0.008	270.9	312.4	-41.5	139.4	32.93	57.26	0.38
C003-1	326.5	445.4	0.008	309.7	285.6	24.1	139.4	7.29	47.15	7.67
C003-2	326.5	445.4	0.008	312.3	265.2	47.1	139.4	4.12	40.79	3.79
C003-3	326.5	445.4	0.008	305.8	266.4	39.4	139.4	4.56	44.39	2.18
C003-4	326.5	445.4	0.008	308.0	255.7	52.3	139.4	5.12	42.70	5.87
C003-5	326.5	445.4	0.008	278.1	272.1	6.1	139.4	4.00	56.77	6.72
C005-1	397.0	491.8	0.008	331.8	346.8	-15.1	139.4	123.11	52.85	6.76
C005-2	397.0	491.8	0.008	348.0	364.2	-16.2	139.4	125.18	81.75	13.71
C005-3	397.0	491.8	0.008	321.6	344.9	-23.4	139.4	54.63	50.02	16.64
C005-5	397.0	491.8	0.008	322.8	295.4	27.3	139.4	11.13	50.71	13.70
K105-1	266.9	335.3	0.008	206.6	283.6	-77.0	139.4	5.01	63.99	13.13
K105-3	266.9	335.3	0.008	235.4	286.0	-50.6	139.4	7.80	51.99	4.90
K105-4	266.9	335.3	0.008	203.6	273.2	-69.5	139.4	4.05	61.04	10.00
K105-5	266.9	335.3	0.008	190.7	247.5	-56.9	139.4	2.58	55.85	3.20
Y080-1	12.9	43.8	0.008	193.4	268.7	-75.3	139.4	5.02	62.22	5.63
Y080-2	12.9	43.8	0.008	223.0	281.0	-58.0	139.4	3.97	84.57	8.40
Y080-4	12.9	43.8	0.008	214.0	273.2	-59.2	139.4	4.91	60.75	6.29
Y080-5	12.9	43.8	0.008	243.0	311.1	-68.1	139.4	16.74	69.95	35.68
C008-1	685.1	263.6	0.008	482.1	296.9	185.2	139.4	5.86	67.05	0.89
C008-2	685.1	263.6	0.008	356.3	259.2	97.1	139.4	2.00	60.98	1.54
C008-3	685.1	263.6	0.008	269.5	253.8	15.7	139.4	1.11	82.72	2.42
C008-4	685.1	263.6	0.008	469.6	263.5	206.0	139.4	4.85	56.67	1.43
C013-1	375.0	245.2	0.008	395.2	287.9	107.3	139.4	10.52	53.69	2.29
C013-2	375.0	245.2	0.008	513.7	298.3	215.4	139.4	28.32	44.21	0.61
C013-4	375.0	245.2	0.008	439.6	269.1	170.5	139.4	7.87	44.42	2.08
C013-5	375.0	245.2	0.008	335.7	243.7	92.0	139.4	3.01	47.74	1.57
C016-1	794.2	322.6	0.008	201.6	268.8	-67.2	139.4	2.23	77.35	12.59
C016-2	794.2	322.6	0.008	164.6	263.4	-98.8	139.4	1.60	85.80	2.78
C016-3	794.2	322.6	0.008	210.7	268.5	-57.8	139.4	4.19	53.44	8.71
C016-4	794.2	322.6	0.008	221.3	282.8	-61.5	139.4	2.74	78.58	10.37
C016-5	794.2	322.6	0.008	233.9	281.8	-47.9	139.4	3.43	76.68	13.52
C068-1	114.0	335.3	0.008	593.1	303.8	289.3	139.4	7.32	67.40	2.28
C068-2	114.0	335.3	0.008	603.5	304.7	298.8	139.4	7.62	66.00	2.19
C068-4	114.0	335.3	0.008	276.7	236.7	40.1	139.4	2.21	44.74	1.23
C068-5	114.0	335.3	0.008	407.2	260.2	147.0	139.4	3.90	54.62	1.63

Table 6c. Lowest misfit model results from scenario 3 (model RD023_Q), with a calculated misfit of 4764.

Sample	Sample elevation (m)	Interpolated elevation (m)	Exhumation rate (km/Ma)	Measured AHe age (Ma)	Modeled AHe age (Ma)	Age difference (Ma)	Modeled AFT age (Ma)	eU (ppm)	ESR (µm)	U:Th
B099-1	252.0	21.7	0.008	373.7	351.9	21.8	189.9	24.52	112.18	12.29
B099-2	252.0	21.7	0.008	334.8	313.7	21.1	189.9	18.30	75.77	13.15
B099-4	252.0	21.7	0.008	412.5	330.0	82.5	189.9	23.92	84.16	10.64
B099-5	252.0	21.7	0.008	369.2	313.5	55.8	189.9	20.82	68.93	8.78
B100-1	244.3	15.0	0.008	332.5	304.4	28.1	189.9	14.52	57.21	4.03
B100-2	244.3	15.0	0.008	327.8	291.9	35.9	189.9	27.12	42.21	5.46
B100-3	244.3	15.0	0.008	362.8	308.3	54.6	189.9	26.36	60.01	5.28
B100-4	244.3	15.0	0.008	375.7	331.5	44.2	189.9	26.36	82.76	4.51
B100-5	244.3	15.0	0.008	313.5	301.1	12.3	189.9	17.90	54.34	5.15
B101-1	269.9	14.5	0.008	371.4	325.1	46.3	189.9	26.54	62.57	6.37
B101-2	269.9	14.5	0.008	367.8	334.7	33.2	189.9	34.38	67.04	4.14
B101-3	269.9	14.5	0.008	303.4	296.1	7.3	189.9	18.63	59.03	5.16
B101-5	269.9	14.5	0.008	348.7	319.8	28.9	189.9	18.56	68.83	5.75
B102-1	246.6	19.8	0.008	238.8	319.7	-80.9	189.9	27.09	65.62	26.07
B102-2	246.6	19.8	0.008	222.4	301.5	-79.1	189.9	20.91	56.81	12.54
B102-4	246.6	19.8	0.008	232.1	311.5	-79.5	189.9	17.43	68.95	10.26
B102-5	246.6	19.8	0.008	253.6	315.3	-61.7	189.9	18.47	72.83	13.20
B105-1	236.0	24.5	0.008	307.3	306.2	1.1	189.9	12.95	70.66	5.88
B105-3	236.0	24.5	0.008	526.8	347.5	179.3	189.9	50.81	93.32	2.52
B105-4	236.0	24.5	0.008	395.8	333.4	62.4	189.9	24.74	76.32	5.04
B105-5	236.0	24.5	0.008	522.8	352.6	170.2	189.9	50.70	76.22	3.16
B106-1	249.8	71.8	0.008	250.7	336.2	-85.6	189.9	34.41	70.20	0.53
B106-2	249.8	71.8	0.008	302.9	348.0	-45.1	189.9	52.84	60.85	0.47
B106-3	249.8	71.8	0.008	269.9	318.2	-48.3	189.9	46.82	51.73	0.42
B106-4	249.8	71.8	0.008	319.5	329.9	-10.4	189.9	72.01	54.48	0.02
B106-5	249.8	71.8	0.008	270.9	319.6	-48.7	189.9	32.93	57.26	0.38
C003-1	326.5	445.4	0.008	309.7	278.2	31.5	189.9	7.29	47.15	7.67
C003-2	326.5	445.4	0.008	312.3	256.2	56.1	189.9	4.12	40.79	3.79
C003-3	326.5	445.4	0.008	305.8	257.8	47.9	189.9	4.56	44.39	2.18
C003-4	326.5	445.4	0.008	308.0	265.1	42.9	189.9	5.12	42.70	5.87
C003-5	326.5	445.4	0.008	278.1	265.1	13.0	189.9	4.00	56.77	6.72
C005-1	397.0	491.8	0.008	331.8	364.7	-32.9	189.9	123.11	52.85	6.76
C005-2	397.0	491.8	0.008	348.0	366.0	-18.0	189.9	125.18	81.75	13.71
C005-3	397.0	491.8	0.008	321.6	340.9	-19.4	189.9	54.63	50.02	16.64
C005-5	397.0	491.8	0.008	322.8	302.9	19.8	189.9	11.13	50.71	13.70
K105-1	266.9	335.3	0.008	206.6	288.6	-82.0	189.9	5.01	63.99	13.13
K105-3	266.9	335.3	0.008	235.4	293.3	-57.9	189.9	7.80	51.99	4.90
K105-4	266.9	335.3	0.008	203.6	282.3	-78.6	189.9	4.05	61.04	10.00
K105-5	266.9	335.3	0.008	190.7	254.9	-64.3	189.9	2.58	55.85	3.20
Y080-1	12.9	43.8	0.008	193.4	267.7	-74.3	189.9	5.02	62.22	5.63
Y080-2	12.9	43.8	0.008	223.0	283.7	-60.7	189.9	3.97	84.57	8.40
Y080-4	12.9	43.8	0.008	214.0	278.6	-64.6	189.9	4.91	60.75	6.29
Y080-5	12.9	43.8	0.008	243.0	318.2	-75.2	189.9	16.74	69.95	35.68
C008-1	685.1	263.6	0.008	482.1	290.6	191.6	189.9	5.86	67.05	0.89
C008-2	685.1	263.6	0.008	356.3	256.3	100.0	189.9	2.00	60.98	1.54
C008-3	685.1	263.6	0.008	269.5	261.4	8.1	189.9	1.11	82.72	2.42
C008-4	685.1	263.6	0.008	469.6	270.4	199.2	189.9	4.85	56.67	1.43
C013-1	375.0	245.2	0.008	395.2	298.5	96.7	189.9	10.52	53.69	2.29
C013-2	375.0	245.2	0.008	513.7	293.6	220.1	189.9	28.32	44.21	0.61
C013-4	375.0	245.2	0.008	439.6	271.6	168.0	189.9	7.87	44.42	2.08
C013-5	375.0	245.2	0.008	335.7	249.2	86.5	189.9	3.01	47.74	1.57
C016-1	794.2	322.6	0.008	201.6	269.8	-68.2	189.9	2.23	77.35	12.59
C016-2	794.2	322.6	0.008	164.6	275.5	-110.9	189.9	1.60	85.80	2.78
C016-3	794.2	322.6	0.008	210.7	266.6	-55.9	189.9	4.19	53.44	8.71
C016-4	794.2	322.6	0.008	221.3	280.3	-59.0	189.9	2.74	78.58	10.37
C016-5	794.2	322.6	0.008	233.9	284.9	-51.0	189.9	3.43	76.68	13.52
C068-1	114.0	335.3	0.008	593.1	304.5	288.6	189.9	7.32	67.40	2.28
C068-2	114.0	335.3	0.008	603.5	289.0	314.5	189.9	7.62	66.00	2.19
C068-4	114.0	335.3	0.008	276.7	244.8	32.0	189.9	2.21	44.74	1.23
C068-5	114.0	335.3	0.008	407.2	272.5	134.7	189.9	3.90	54.62	1.63

Table 6d. Lowest misfit model results from scenario 4 (model RD023_BD), with a calculated misfit of 4432.

Sample	Sample elevation (m)	Interpolated elevation (m)	Exhumation rate (km/Ma)	Measured AHe age (Ma)	Modeled AHe age (Ma)	Age difference (Ma)	Modeled AFT age (Ma)	eU (ppm)	ESR (µm)	U:Th
B099-1	252.0	21.7	0.008	373.7	314.6	59.1	258.0	24.52	112.18	12.29
B099-2	252.0	21.7	0.008	334.8	284.6	50.2	258.0	18.30	75.77	13.15
B099-4	252.0	21.7	0.008	412.5	287.4	125.2	258.0	23.92	84.16	10.64
B099-5	252.0	21.7	0.008	369.2	277.9	91.3	258.0	20.82	68.93	8.78
B100-1	244.3	15.0	0.008	332.5	267.1	65.4	258.0	14.52	57.21	4.03
B100-2	244.3	15.0	0.008	327.8	272.0	55.8	258.0	27.12	42.21	5.46
B100-3	244.3	15.0	0.008	362.8	288.6	74.2	258.0	26.36	60.01	5.28
B100-4	244.3	15.0	0.008	375.7	299.6	76.1	258.0	26.36	82.76	4.51
B100-5	244.3	15.0	0.008	313.5	270.2	43.3	258.0	17.90	54.34	5.15
B101-1	269.9	14.5	0.008	371.4	287.1	84.4	258.0	26.54	62.57	6.37
B101-2	269.9	14.5	0.008	367.8	303.3	64.5	258.0	34.38	67.04	4.14
B101-3	269.9	14.5	0.008	303.4	273.3	30.1	258.0	18.63	59.03	5.16
B101-5	269.9	14.5	0.008	348.7	281.0	67.8	258.0	18.56	68.83	5.75
B102-1	246.6	19.8	0.008	238.8	293.2	-54.4	258.0	27.09	65.62	26.07
B102-2	246.6	19.8	0.008	222.4	279.1	-56.7	258.0	20.91	56.81	12.54
B102-4	246.6	19.8	0.008	232.1	276.4	-44.4	258.0	17.43	68.95	10.26
B102-5	246.6	19.8	0.008	253.6	275.9	-22.2	258.0	18.47	72.83	13.20
B105-1	236.0	24.5	0.008	307.3	279.6	27.8	258.0	12.95	70.66	5.88
B105-3	236.0	24.5	0.008	526.8	313.7	213.2	258.0	50.81	93.32	2.52
B105-4	236.0	24.5	0.008	395.8	297.9	97.9	258.0	24.74	76.32	5.04
B105-5	236.0	24.5	0.008	522.8	302.8	220.0	258.0	50.70	76.22	3.16
B106-1	249.8	71.8	0.008	250.7	297.6	-47.0	258.0	34.41	70.20	0.53
B106-2	249.8	71.8	0.008	302.9	297.6	5.3	258.0	52.84	60.85	0.47
B106-3	249.8	71.8	0.008	269.9	299.4	-29.5	258.0	46.82	51.73	0.42
B106-4	249.8	71.8	0.008	319.5	296.5	23.0	258.0	72.01	72.01	0.02
B106-5	249.8	71.8	0.008	270.9	273.0	-2.1	258.0	32.93	57.26	0.38
C003-1	326.5	445.4	0.008	309.7	262.4	47.3	258.0	7.29	47.15	7.67
C003-2	326.5	445.4	0.008	312.3	248.2	64.1	258.0	4.12	40.79	3.79
C003-3	326.5	445.4	0.008	305.8	238.8	67.0	258.0	4.56	44.39	2.18
C003-4	326.5	445.4	0.008	308.0	243.8	64.2	258.0	5.12	42.70	5.87
C003-5	326.5	445.4	0.008	278.1	256.0	22.1	258.0	4.00	56.77	6.72
C005-1	397.0	491.8	0.008	331.8	331.0	0.8	258.0	123.11	52.85	6.76
C005-2	397.0	491.8	0.008	348.0	350.3	-2.3	258.0	125.18	81.75	13.71
C005-3	397.0	491.8	0.008	321.6	305.5	16.1	258.0	54.63	50.02	16.64
C005-5	397.0	491.8	0.008	322.8	261.7	61.0	258.0	11.13	50.71	13.70
K105-1	266.9	335.3	0.008	206.6	253.9	-47.3	258.0	5.01	63.99	13.13
K105-3	266.9	335.3	0.008	235.4	259.1	-23.7	258.0	7.80	51.99	4.90
K105-4	266.9	335.3	0.008	203.6	254.1	-50.4	258.0	4.05	61.04	10.00
K105-5	266.9	335.3	0.008	190.7	241.9	-51.2	258.0	2.58	55.85	3.20
Y080-1	12.9	43.8	0.008	193.4	242.9	-49.6	258.0	5.02	62.22	5.63
Y080-2	12.9	43.8	0.008	223.0	251.4	-28.4	258.0	3.97	84.57	8.40
Y080-4	12.9	43.8	0.008	214.0	240.2	-26.2	258.0	4.91	60.75	6.29
Y080-5	12.9	43.8	0.008	243.0	284.1	-41.1	258.0	16.74	69.95	35.68
C008-1	685.1	263.6	0.008	482.1	257.6	224.6	258.0	5.86	67.05	0.89
C008-2	685.1	263.6	0.008	356.3	237.1	119.2	258.0	2.00	60.98	1.54
C008-3	685.1	263.6	0.008	269.5	235.6	33.8	258.0	1.11	82.72	2.42
C008-4	685.1	263.6	0.008	469.6	249.5	220.1	258.0	4.85	56.67	1.43
C013-1	375.0	245.2	0.008	395.2	258.3	136.9	258.0	10.52	53.69	2.29
C013-2	375.0	245.2	0.008	513.7	281.5	232.2	258.0	28.32	44.21	0.61
C013-4	375.0	245.2	0.008	439.6	248.4	191.2	258.0	7.87	44.42	2.08
C013-5	375.0	245.2	0.008	335.7	222.4	113.3	258.0	3.01	47.74	1.57
C016-1	794.2	322.6	0.008	201.6	244.4	-42.8	258.0	2.23	77.35	12.59
C016-2	794.2	322.6	0.008	164.6	252.5	-87.9	258.0	1.60	85.80	2.78
C016-3	794.2	322.6	0.008	210.7	234.6	-23.9	258.0	4.19	53.44	8.71
C016-4	794.2	322.6	0.008	221.3	250.9	-29.6	258.0	2.74	78.58	10.37
C016-5	794.2	322.6	0.008	233.9	258.5	-24.7	258.0	3.43	76.68	13.52
C068-1	114.0	335.3	0.008	593.1	268.3	324.8	258.0	7.32	67.40	2.28
C068-2	114.0	335.3	0.008	603.5	271.1	332.5	258.0	7.62	66.00	2.19
C068-4	114.0	335.3	0.008	276.7	235.8	40.9	258.0	2.21	44.74	1.23
C068-5	114.0	335.3	0.008	407.2	247.9	159.3	258.0	3.90	54.62	1.63

Table 6e. Lowest misfit model results from scenario 5 (model RD023_BL), with a calculated misfit of 4355.

Sample	Sample elevation (m)	Interpolated elevation (m)	Exhumation rate (km/Ma)	Measured AHe age (Ma)	Modeled AHe age (Ma)	Age difference (Ma)	Modeled AFT age (Ma)	eU (ppm)	ESR (µm)	U:Th
B099-1	252.0	21.7	0.0088	373.7	332.8	40.9	315.3	24.52	112.18	12.29
B099-2	252.0	21.7	0.0088	334.8	298.5	36.3	315.3	18.30	75.77	13.15
B099-4	252.0	21.7	0.0088	412.5	317.7	94.8	315.3	23.92	84.16	10.64
B099-5	252.0	21.7	0.0088	369.2	303.2	66.0	315.3	20.82	68.93	8.78
B100-1	244.3	15.0	0.0088	332.5	281.2	51.3	315.3	14.52	57.21	4.03
B100-2	244.3	15.0	0.0088	327.8	287.4	40.4	315.3	27.12	42.21	5.46
B100-3	244.3	15.0	0.0088	362.8	307.9	55.0	315.3	26.36	60.01	5.28
B100-4	244.3	15.0	0.0088	375.7	323.5	52.2	315.3	26.36	82.76	4.51
B100-5	244.3	15.0	0.0088	313.5	289.0	24.5	315.3	17.90	54.34	5.15
B101-1	269.9	14.5	0.0088	371.4	305.9	65.6	315.3	26.54	62.57	6.37
B101-2	269.9	14.5	0.0088	367.8	309.9	58.0	315.3	34.38	67.04	4.14
B101-3	269.9	14.5	0.0088	303.4	279.3	24.1	315.3	18.63	59.03	5.16
B101-5	269.9	14.5	0.0088	348.7	303.1	45.6	315.3	18.56	68.83	5.75
B102-1	246.6	19.8	0.0088	238.8	305.4	-66.5	315.3	27.09	65.62	26.07
B102-2	246.6	19.8	0.0088	222.4	291.8	-69.3	315.3	20.91	56.81	12.54
B102-4	246.6	19.8	0.0088	232.1	291.3	-59.2	315.3	17.43	68.95	10.26
B102-5	246.6	19.8	0.0088	253.6	294.1	-40.5	315.3	18.47	72.83	13.20
B105-1	236.0	24.5	0.0088	307.3	283.6	23.7	315.3	12.95	70.66	5.88
B105-3	236.0	24.5	0.0088	526.8	338.2	188.6	315.3	50.81	93.32	2.52
B105-4	236.0	24.5	0.0088	395.8	315.2	80.6	315.3	24.74	76.32	5.04
B105-5	236.0	24.5	0.0088	522.8	335.6	187.3	315.3	50.70	76.22	3.16
B106-1	249.8	71.8	0.0088	250.7	316.6	-65.9	315.3	34.41	70.20	0.53
B106-2	249.8	71.8	0.0088	302.9	320.9	-18.0	315.3	52.84	60.85	0.47
B106-3	249.8	71.8	0.0088	269.9	304.3	-34.4	315.3	46.82	51.73	0.42
B106-4	249.8	71.8	0.0088	319.5	310.7	8.9	315.3	72.01	72.01	0.02
B106-5	249.8	71.8	0.0088	270.9	304.9	-34.0	315.3	32.93	57.26	0.38
C003-1	326.5	445.4	0.0088	309.7	267.0	42.7	315.3	7.29	47.15	7.67
C003-2	326.5	445.4	0.0088	312.3	247.9	64.4	315.3	4.12	40.79	3.79
C003-3	326.5	445.4	0.0088	305.8	237.9	67.8	315.3	4.56	44.39	2.18
C003-4	326.5	445.4	0.0088	308.0	253.4	54.6	315.3	5.12	42.70	5.87
C003-5	326.5	445.4	0.0088	278.1	251.6	26.5	315.3	4.00	56.77	6.72
C005-1	397.0	491.8	0.0088	331.8	355.0	-23.2	315.3	123.11	52.85	6.76
C005-2	397.0	491.8	0.0088	348.0	378.1	-30.1	315.3	125.18	81.75	13.71
C005-3	397.0	491.8	0.0088	321.6	322.7	-1.1	315.3	54.63	50.02	16.64
C005-5	397.0	491.8	0.0088	322.8	274.9	47.8	315.3	11.13	50.71	13.70
K105-1	266.9	335.3	0.0088	206.6	269.9	-63.2	315.3	5.01	63.99	13.13
K105-3	266.9	335.3	0.0088	235.4	266.7	-31.3	315.3	7.80	51.99	4.90
K105-4	266.9	335.3	0.0088	203.6	257.7	-54.0	315.3	4.05	61.04	10.00
K105-5	266.9	335.3	0.0088	190.7	248.9	-58.3	315.3	2.58	55.85	3.20
Y080-1	12.9	43.8	0.0088	193.4	260.5	-67.2	315.3	5.02	62.22	5.63
Y080-2	12.9	43.8	0.0088	223.0	270.3	-47.3	315.3	3.97	84.57	8.40
Y080-4	12.9	43.8	0.0088	214.0	253.1	-39.1	315.3	4.91	60.75	6.29
Y080-5	12.9	43.8	0.0088	243.0	295.3	-52.4	315.3	16.74	69.95	35.68
C008-1	685.1	263.6	0.0088	482.1	278.2	203.9	315.3	5.86	67.05	0.89
C008-2	685.1	263.6	0.0088	356.3	242.5	113.8	315.3	2.00	60.98	1.54
C008-3	685.1	263.6	0.0088	269.5	239.1	30.3	315.3	1.11	82.72	2.42
C008-4	685.1	263.6	0.0088	469.6	255.2	214.3	315.3	4.85	56.67	1.43
C013-1	375.0	245.2	0.0088	395.2	267.2	128.0	315.3	10.52	53.69	2.29
C013-2	375.0	245.2	0.0088	513.7	296.8	216.9	315.3	28.32	44.21	0.61
C013-4	375.0	245.2	0.0088	439.6	262.8	176.8	315.3	7.87	44.42	2.08
C013-5	375.0	245.2	0.0088	335.7	236.3	99.4	315.3	3.01	47.74	1.57
C016-1	794.2	322.6	0.0088	201.6	264.7	-63.1	315.3	2.23	77.35	12.59
C016-2	794.2	322.6	0.0088	164.6	255.5	-90.9	315.3	1.60	85.80	2.78
C016-3	794.2	322.6	0.0088	210.7	253.0	-42.3	315.3	4.19	53.44	8.71
C016-4	794.2	322.6	0.0088	221.3	261.1	-39.8	315.3	2.74	78.58	10.37
C016-5	794.2	322.6	0.0088	233.9	267.7	-33.8	315.3	3.43	76.68	13.52
C068-1	114.0	335.3	0.0088	593.1	286.5	306.7	315.3	7.32	67.40	2.28
C068-2	114.0	335.3	0.0088	603.5	287.5	316.1	315.3	7.62	66.00	2.19
C068-4	114.0	335.3	0.0088	276.7	218.4	58.3	315.3	2.21	44.74	1.23
C068-5	114.0	335.3	0.0088	407.2	251.4	155.8	315.3	3.90	54.62	1.63

CHAPTER 8 – DISCUSSION OF THERMAL MODELING RESULTS AND IMPLICATIONS FOR THE PHANEROZOIC EXHUMATION HISTORY AND TECTONIC EVOLUTION OF HALL PENINSULA

The goal of this study was to characterize the exhumation history of Hall Peninsula using a combination of low-temperature (U-Th-Sm)/He thermochronology (AHe and ZHe), 1D thermal (HeFTy), and 3D thermokinematic modeling (PECUBE) to test various scenarios for the development of the modern high-relief landscape. Results from the AHe and ZHe analyses were highly dispersed with complex cooling age patterns, precluding a straightforward interpretation of the data using a simple (cooling age-elevation or cooling age-distance) transect approach. This section discusses the limitations imposed by the data and the inherent influence of alpha-recoil damage, and presents the preferred interpretations of the tectonic history and landscape evolution based on the results of thermal and thermokinematic models.

8.1 Limitations of RDAAM and Gautheron et al. (2009) diffusion kinetics

In the past decade, much headway has been achieved toward improving our understanding of the effects of alpha-recoil damage on ^{4}He diffusion in the apatite (U-Th-Sm)/He thermochronometer (Flowers, 2009; Flowers et al., 2009; Gautheron et al., 2009; Shuster et al., 2006). However, several characteristics of the data in this study do not fully adhere to the predictions of the RDAAM or Gautheron et al. (2009) diffusion kinetics. Most prominently, according to the RDAAM, the AHe ages are expected to scale in proportion to the eU concentration. While this is true for the dataset when comparing grains from the same sample, the degree to which the AHe ages are dependent on eU varies substantially between samples (with the exception of C005, B103 and Y080,

which demonstrated a negligible relationship with eU) (Figs. 5.15–5.17). Comparing data from vertical and perpendicular transects most clearly reveals this trend. For example, the low-eU-concentration (1-10 ppm) grains from the vertical transect exhibit ages with an eU dependence of up to an order of magnitude greater than those from the perpendicular transect, which had higher average eU concentrations (> 20 ppm), reflecting a much higher apparent sensitivity of the effects of alpha-recoil damage (Figs. 5.15–5.16). Given the elimination of other, more common second-order factors as sources of dispersion in the dataset (e.g., varying grain radius and U- and Th-rich inclusions; Chapter 5), a potential (and likely) explanation for the apparent variation in eU sensitivity in the vertical transect data is the influence of grain chemistry (i.e., F/Cl ratio) on the annealing of radiation damage (Gautheron et al., 2013). An important assumption in both the RDAAM and Gautheron et al. (2009) model is that the annealing behavior of diffusivity-altering damage is directly analogous to that of apatite fission-track damage. Although this has been shown in laboratory experiments to be mostly a valid assumption (Shuster and Farley, 2009), it is also well established that the annealing behavior of fission tracks varies as a function of the Cl content of the grain (Carlson et al., 1999; Green et al., 1986). By applying a fixed Cl concentration for all AHe grains, as is done in both HeFTy and PECUBE, the diffusion kinetics do not account for differences rates of annealing, potentially miscalculating the damage dose and the resulting diffusivity of the grain. In extreme cases, this effect can result in modeled AHe ages that differ by up to ~12–15 % (Gautheron et al., 2013). Unfortunately, since the grains are destroyed during the processing of (U-Th-Sm)/He data, it was not possible to collect the chemical composition information from the analyzed grains after analysis. A semi-quantitative electron

microprobe map scan of each grain after He extraction but prior to dissolution for the actinide concentrations may be the most effective method to attain the relevant chemical information from the grain and characterize the Cl:F variability among grains, without the intrusiveness of laser ablation.

Limitations of the RDAAM and Gautheron et al. (2009) kinetic models were also demonstrated during the use of the HeFTy and PECUBE programs (respectively). In the HeFTy models, only AHe samples with < 300 Ma dispersion among grain cooling ages achieved statistically suitable tT paths when simulations used the RDAAM. This restriction directly hindered the interpretations by precluding the use of data from many of the models. Because much of the thermal history can be recorded by samples with large dispersion (i.e., AHe age $\propto$ eU), excluding select grains from the interpretation may have excluded valuable constraints for the sample's thermal history (Flowers, 2009; Flowers and Kelley, 2011; Flowers et al., 2009). Likewise in PECUBE, the Gautheron et al. (2009) kinetics were unable to reproduce the large span of measured AHe ages in any single sample, even those with higher eU concentrations (e.g., C005; Tables 6a-e). As a result, the misfit values for the PECUBE models were inherently larger. Moreover, unlike the HeFTy program, which only shows 'acceptable' or 'good' fits, the PECUBE program always outputs a misfit value. Yet, although it is used as a quantitative measure of the closeness-of-fit between the modeled ages and input data, given the highly dispersed data in this study, the relative value provides a more meaningful gauge for the model quality. In other words, a standalone misfit value is not readily interpretable with such dispersed data; it is the relative difference between two or more misfits that allows for classification of 'better' or 'worse.' This was troublesome because 1) the larger misfits were less likely

to represent a ‘best-fit’ model; and 2) the exhumation scenarios yielded similar distributions of AHe ages, and thus achieved similar (relatively low) misfits (Tables 6a-e). The combination of these factors meant that the model misfits did not reflect a closeness-of-fit among the individual samples, but rather a generalized closeness between the two groups of modeled and measured ages. To confirm this, the model misfits were plotted against the mean modeled AHe age (Fig. 8.1A). The plots revealed a strong (quadratic) correlation, with a convergence about a mean modeled AHe age of ~282 Ma, suggesting that a minimum misfit value had been achieved. However, because similar minimum misfits were achieved by models from multiple scenarios (Fig. 8.1B), the misfit values were deemed unfit for differentiating the model quality and aiding in establishing detailed constraints for the exhumation history. Thus, inferences regarding the exhumation history based on the models were limited to only first-order interpretations (rapid vs. slow average rate of exhumation).

A

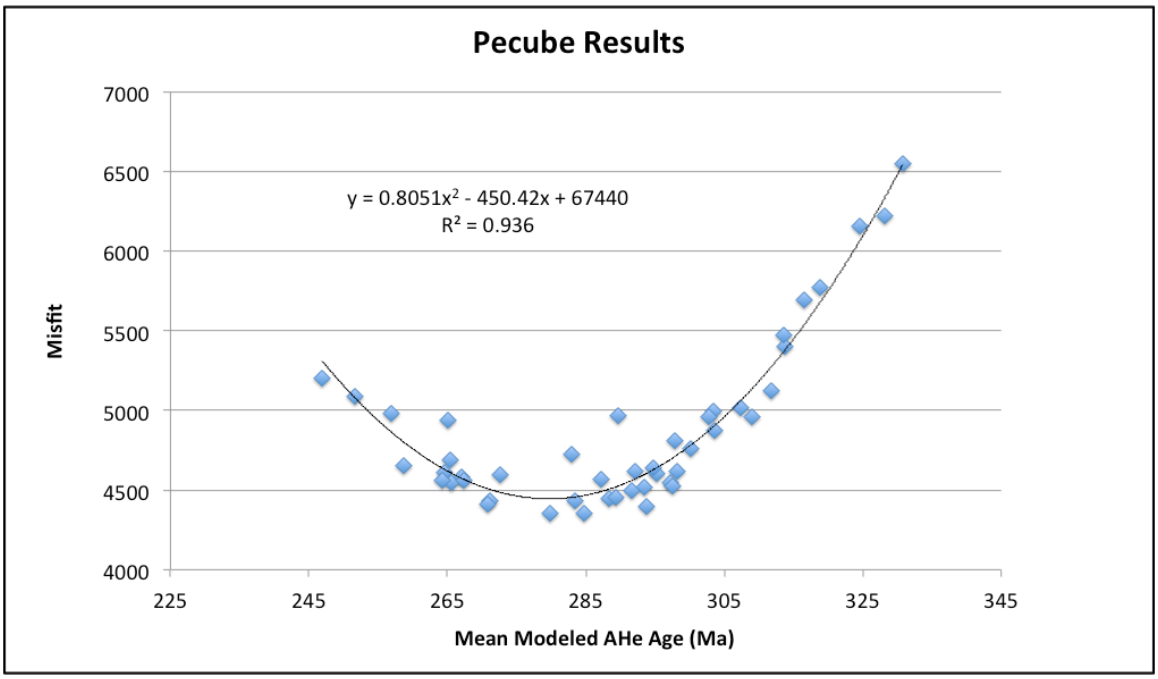

B

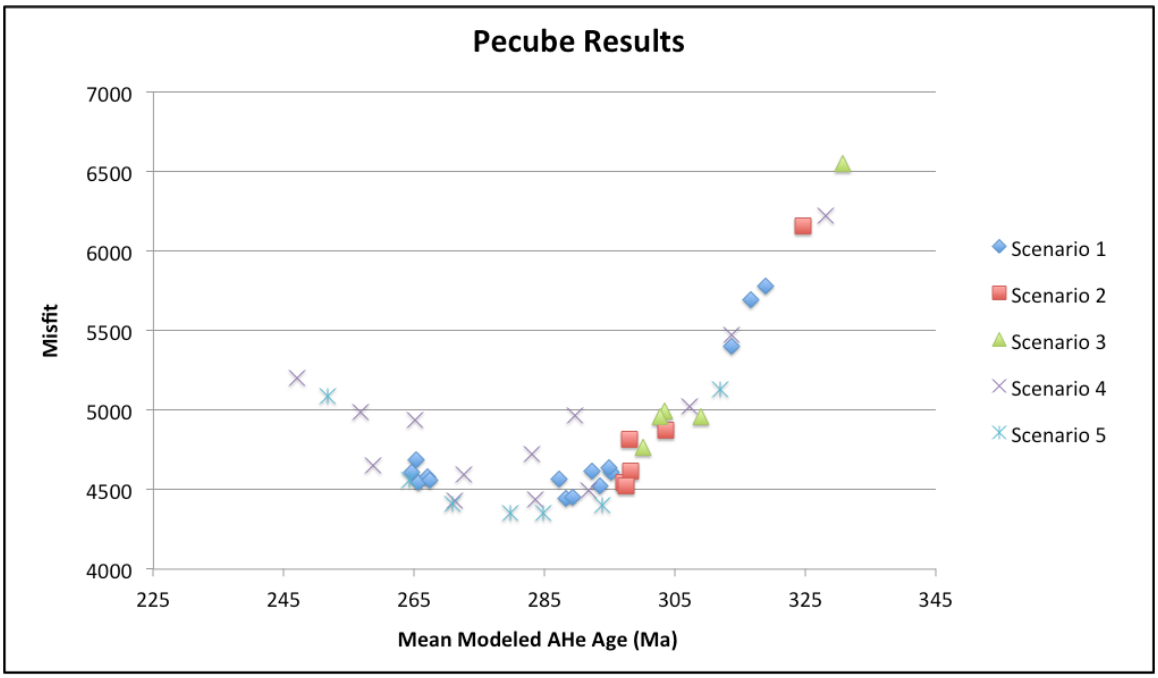

Figure 8.1. PECUBE results for scenario model groups. (B) Same plot as (A), with model results differentiated by scenario. The multiple models from each scenario were used to test the response of the misfit to changes in exhumation rate, timing and total offset of faults (if present), timing of surface elevation change, or some combination thereof for the given scenario.

8.2 Implications for the exhumation history of Hall Peninsula

Despite the limitations discussed in the previous section, several geologic constraints (interpretations) were still attained from the data.

8.2.1 Alpha-recoil damage

The most straightforward inference was provided by the data directly, in the relationships between eU and {He}/eU (i.e., He-age). As discussed in chapters three and five, grains that experience exceptionally slow cooling (< 1 ºC/Ma) are susceptible to the formation of crystal defects during the prolonged exposure to alpha decay recoil events. If the rates of slow cooling are maintained for extended time periods (i.e., 100s of Ma), the proportion of damaged sites becomes great enough to alter the ^{4}He diffusion character of the grain (Shuster et al., 2006). Because the number of alpha decays is directly related to the concentration of parent isotopes (i.e., eU), grains exposed to these conditions are predicted to yield a correspondence between He-age and eU (Flowers et al., 2009; Gautheron et al., 2009; Shuster et al., 2006). Thus, the strong dependence of the AHe and ZHe ages on eU (Figs. 5.15–5.17, 5.21) supports the first-order (qualitative) interpretation that the samples were subject to extremely slow, protracted cooling.

8.2.2 Comprehensive thermal history of the perpendicular transect

Although the results from the HeFTy models were consistent with slow cooling for most of the samples, discrepancies between the tT path constraints made it difficult to detect regional variations in cooling. Therefore, to aid interpretation of the HeFTy-derived thermal histories in a spatiotemporal context, tT constraints from the coastline-perpendicular transect samples were compiled into a single 2D time-distance plot of the thermal history (Fig. 8.2). This entailed reconstructing the paleo-isotherms based on the

range of potential times that each sample could be at specific temperatures, in ten-degree intervals between 30 – 80 ºC. For example, as shown in Fig. 6.4, the HeFTy results from sample B100 indicate that it was at 70 ºC between 310–520 Ma, 60 ºC between 260–450 Ma, 50 ºC between 120–390 Ma, and so on. In all instances, the isotherms intersect the constraints for each sample, and the isotherms were interpolated in a linear horizontal fashion except where slopes were required. The approach for fitting the isotherms was to construct a thermal history with maximum parsimony, in an attempt to minimize any unnecessary complexity in the interpretation. The result was a fit that demonstrates that the data and HeFTy models from the coastline-perpendicular transect support a unified thermal history, without needing to evoke additional external constraints.

The plot confirms that the constraints from all samples coincide with a history of slow cooling for the eastern half of Hall Peninsula. Moreover, the inconsistent tT constraints between the SW and NE samples were resolved by a gradual decrease in cooling rate towards the northeast margin (i.e., near Cumberland Sound). Most importantly, this reveals a contrast in the timing of samples cooling through the upper versus lower temperature isotherms. For instance, samples C005–B102 pass through the 70 ºC isotherm at consistent times, interpreted here between ca. 340–360 Ma, while the

Figure 8.2. (Next page) 2D time-distance plot of thermal history for the coastline-perpendicular transect samples (C005–B099; Fig. 1.2) based on a compilation of HeFTy (RDAAM) model results. (A) Spacing along the x-axis is scaled to match distance between sample locations. Samples C005, K105, B105 and B100 yielded statistically 'good' fits, and thus defined the first-order position of the isotherms. Other samples with 'acceptable' fits served as secondary constraints and constrained the position of the isotherms when interpolating between the 'good' samples. (B) Same plot as (A), with vertical bars indicating the range of times that the isotherms yielded statistically suitable fits to the data (see text for discussion). Thick vertical bars indicate 'good' tT envelopes; 'acceptable' tT envelopes are indicated by thinner bars.

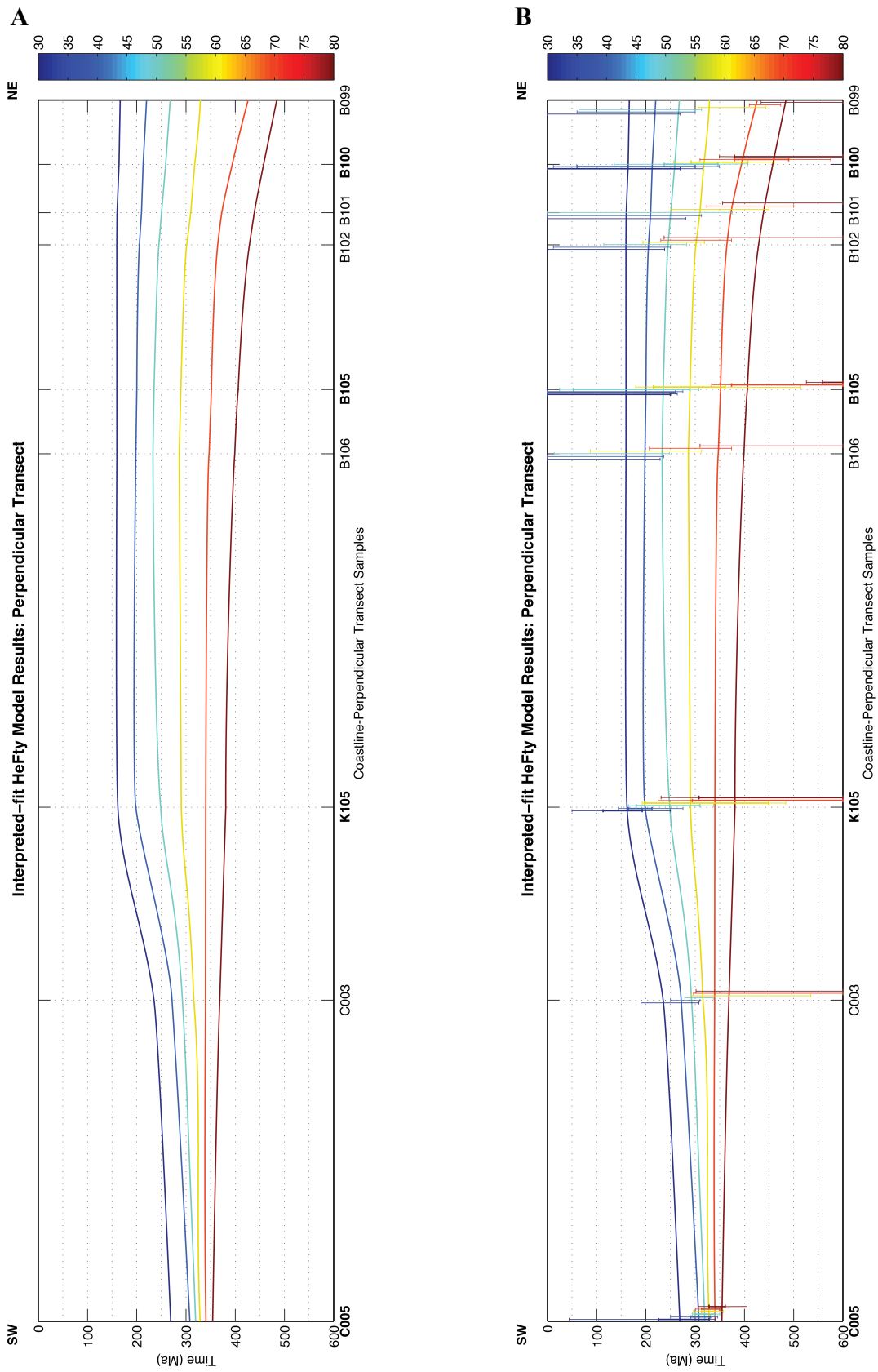
A
B
Interpreted–fit HeFty Model Results: Perpendicular Transect
SW
NE
C005
C003
K105
B106
B105
B102 B101
B100
B099
Coastline-Perpendicular Transect Samples
Time (Ma)
0
100
200
300
400
500
600
30
35
40
45
50
55
60
65
70
75
80

constraints B099–B101 require earlier cooling through 70 ºC; yet, the samples in the southwest indicate cooling through the lower temperatures much earlier than those in the northeast. It is also important to note, however, that this interpretation does not represent the only solution, but rather it is one of several possible arrangements of the paleo-isotherms based on the HeFTy tT constraints given the large uncertainties. Alternative interpretations could involve episodes of more rapid cooling (>1 ºC/Ma), or less uniform spacing of the isotherms. However, in the absence of additional constraints (e.g., AFT analyses, or better estimates for the amount of denudation since the Precambrian), owing to the principle of maximum parsimony, the preferred interpretation was the simplest arrangement for the paleo-isotherms.

Four main conclusions are interpreted from these results: 1) Overall, the thermal history of Hall Peninsula is characterized by extremely slow cooling since the Paleozoic; 2) variance in the timing of cooling through the 70 ºC isotherm (and 80 ºC, though with less certainty) between ca. 340–400 Ma in samples B099–B102 coincides with post-Ordovician fault block movements in the Eastern Canadian Arctic (Sanford, 1987), and may indicate disturbances (i.e., cooling) of the footwall isotherms during fault motion in Cumberland Sound; 3) cooling of samples from the interior of Hall Peninsula (C005 and C003; Fig. 1.2) through lower temperatures (50 to 30 ºC) occurred before the samples to the east, and since these two samples were at the bottom of large valleys and collected at higher elevation than the other perpendicular transect samples (between 50–150 m), it may be the case that the earlier cooling reflects the early (pre-Cenozoic) development of relief, though this is more speculative than the previous points; and 4) the data maintain no apparent record of accelerated cooling as a response to rifting during the late

Cretaceous to early Paleogene, or subsequent rift-flank responses, and thus are unable differentiate between the end-member types of escarpment development on Hall Peninsula (e.g., Gallagher and Brown, 1997).

8.2.3 Vertical and coastline-parallel transect samples

Construction of a similar 2D time-elevation plot was attempted for the vertical transect samples. However, the incompatible nature of samples (i.e., that structurally lower samples required lower temperatures at times when the higher samples require higher temperatures) made this impossible. Although it is possible to achieve this relationship through faulting, no faults displaying Phanerozoic offset were mapped during the field campaign on Hall Peninsula in 2012. Thus, the conflicting tT constraints were attributed to the effects of apatite composition on alpha-recoil damage (discussed in section 8.1).

Unfortunately, since only one sample (Y080) from the coastline-parallel transect yielded a thermal model with acceptable or good fits, it was not possible to construct a 2D time-distance plot for the peninsula margin. However, the comparable tT envelopes of sample Y080 and K105 (Fig. 6.2), and the fact that Y080 was collected nearly orthogonal to the location of K105 along the coastline-perpendicular transect (Fig. 1.2), supports an interpretation that the southern region of the peninsula experienced a cooling history similar to the interior.

8.2.4 Interpreted exhumation history

The suitable tT paths modeled using the RDAAM (AHe; Flowers et al., 2009) in HeFTy, and exhumation scenarios using Gautheron et al. (2009) diffusion kinetics in PECUBE, indicate that Hall Peninsula has experienced extremely slow cooling ($\leq$ 1

ºC/Ma) since the mid-Paleozoic. The ZHe models from HeFTy (ZRDAAM; Guenthner et al., 2013) indicate an earlier history of slow cooling as well, constraining the samples' temperature to between 160–140 ºC during late Mesoproterozoic to early Paleoproterozoic times. The ZHe constraints are also consistent with the higher temperature muscovite $^{40}Ar/^{39}Ar$ (T_c ~420–450 ºC) cooling ages of ca. 1690–1640 Ma (Skipton et al., 2015), and thus provide a continuous, consistent thermal history for Hall Peninsula. Collectively, these three independent thermochronometers record a thermal history characterized by protracted, slow cooling.

Several inferences were drawn from the thermal histories recorded in the data. The most significant inference was that, despite its location along the eCAR, Hall Peninsula experienced relatively little, if any, exhumation in response to the formation of Baffin Bay and Davis Strait. This is in stark contrast the to the more rapid, rift-related exhumation observed elsewhere in Labrador (Centeno, 2005) and N-C Baffin (Yaehne, 2008). The lack of exhumational cooling of the Hall Peninsula crustal block during the Cenozoic also suggests that the recent (Neogene) km-scale uplift and exhumation interpreted in West Greenland (Japsen et al., 2006; Japsen et al., 2005), on the conjugate side of Baffin Bay, either did not occur on Hall Peninsula or was limited in extent by comparison. Moreover, the history of long-term slow cooling supports an interpretation that the landscape on Hall Peninsula has experienced minimal amounts of modification since the samples cooled to low temperatures (<70 ºC) in the mid- to late-Paleozoic, such that exhumation was limited to less than 2-4 km since that time. Thus, the modern high relief (>800 m) landscape on Hall Peninsula was likely generated when the samples were cooled below the temperature sensitivity of the AHe thermochronometer (i.e., 40-70 ºC).

The absence of an accelerated exhumation event during the Cenozoic may have in part been because the peninsula is not located along a true rift-margin, as the east/southeast portion of the Baffin continental shelf is bound by the Ungava Fault Zone (UFZ), a complex transform-to-transpressional fault system (Suckro et al., 2013), thereby limiting the extent of crustal thinning and thus reducing its predisposition to rift-related uplift. Similarly, the slow exhumation during this time also suggests that the continental side of this margin (i.e., Hall Peninsula) was not subjected to thermally-driven uplift during motion along the UFZ (Parsiegla et al., 2009; Todd and Keen, 1989), or during the nearby passage of the proto-Icelandic plume beneath the region at ca. 60 Ma (Gerlings et al., 2009).

The slow paleo-erosion rates ($\leq$ 10 m/Ma) necessary to yield a landscape evolution scenario of limited modification, as required for this interpretation, are in agreement with the 1 m/My Quaternary erosion rates, measured using terrestrial cosmogenic nuclide dating of the Torngat Mountains of Labrador (Marquette et al., 2004), as well as the estimated $\leq$ 2.5 m/Ma Phanerozoic erosion rates for the interior Canadian Shield (Flowers et al., 2006). Finally, the coincidence of earlier cooling of samples on the eastern margin between ca. 400–350 Ma with the motion of NW-SE trending extensional half-graben structures bounding Hall Peninsula, and observed elsewhere on Baffin and the Canadian Arctic Platform, which have been interpreted as active in middle-to-late Paleozoic (Sanford, 1987), suggested that the samples may record motion along the Cumberland Sound normal fault system, thereby constraining its existence to at least the Paleozoic.

CHAPTER 9 – CONCLUSIONS

New apatite and zircon (U-Th-Sm)/He data from 26 samples collected along three transects across Hall Peninsula provide complex, highly dispersed cooling ages, ranging from 75 to 843 Ma and 326 to 1067 Ma, respectively. The large amount of inter- and intra-sample variation in grain ages correlates strongly with grain eU concentration, indicating a strong influence from radiation damage on the measured cooling ages. This correlation provides a first-order (qualitative) interpretation that the samples were subject to extremely slow, protracted cooling.

Suitable tT paths modeled using the RDAAM (AHe; Flowers et al., 2009) in HeFTy, and exhumation scenarios using Gautheron et al. (2009) diffusion kinetics in PECUBE, indicate that Baffin Island has experienced extremely slow cooling (≤1 ºC/Ma) that dates back to the mid to late Paleozoic. The ZHe models from HeFTy (ZRDAAM; Guenthner et al., 2013) reveal an earlier history of slow cooling as well, constraining the samples' temperature to between 160–140 ºC during late Mesoproterozoic to early Paleoproterozoic times. Collectively, the HeFTy and PECUBE results suggest that Hall Peninsula likely did not experience substantial (3+ km) exhumation as a result of rifting between Canada and Greenland in the late Mesozoic to early Cenozoic, with the overall pattern of cooling histories indicating that the peninsula experienced extremely slow exhumation throughout the Phanerozoic.

REFERENCES

Ault, A. K., Flowers, R. M., and Bowring, S. A., 2009, Phanerozoic burial and unroofing history of the western Slave craton and Wopmay orogen from apatite (U–Th)/He thermochronometry: Earth and Planetary Science Letters, v. 284, no. 1-2, p. 1-11.

Balestrieri, M. L., Stuart, F. M., Persano, C., Abbate, E., and Bigazzi, G., 2005, Geomorphic development of the escarpment of the Eritrean margin, southern Red Sea from combined apatite fission-track and (U–Th)/He thermochronometry: Earth and Planetary Science Letters, v. 231, no. 1–2, p. 97-110.

Bonow, J. M., Japsen, P., Lidmar-Bergström, K., Chalmers, J. A., and Pedersen, A. K., 2006a, Cenozoic uplift of Nuussuaq and Disko, West Greenland—elevated erosion surfaces as uplift markers of a passive margin: Geomorphology, v. 80, no. 3-4, p. 325-337.

Bonow, J. M., Japsen, P., and Nielsen, T. F., 2014, High-level landscapes along the margin of southern East Greenland–a record of tectonic uplift and incision after breakup in the NE Atlantic: Global and Planetary Change.

Bonow, J. M., Lidmar-Bergström, K., and Japsen, P., 2006b, Palaeosurfaces in central West Greenland as reference for identification of tectonic movements and estimation of erosion: Global and Planetary Change, v. 50, no. 3-4, p. 161-183.

Braun, J., 2003, Pecube: a new finite-element code to solve the 3D heat transport equation including the effects of a time-varying, finite amplitude surface topography: Computers & Geosciences, v. 29, no. 6, p. 787-794.

Braun, J., and Beaumont, C., 1989, A physical explanation of the relation between flank uplifts and the breakup unconformity at rifted continental margins: Geology, v. 17, no. August, p. 760-764.

Braun, J., and van der Beek, P., 2004, Evolution of passive margin escarpments: What can we learn from low-temperature thermochronology?: Journal of Geophysical Research, v. 109, no. F4, p. F04009-F04009.

Braun, J., van der Beek, P., Valla, P., Robert, X., Herman, F., Glotzbach, C., Pedersen, V., Perry, C., Simon-Labric, T., and Prigent, C., 2012, Quantifying rates of landscape evolution and tectonic processes by thermochronology and numerical modeling of crustal heat transport using PECUBE: Tectonophysics, v. 524-525, p. 1-28.

Brown, R. W., Summerfield, M. A., and Gleadow, A. J. W., 2002, Denudational history along a transect across the Drakensberg Escarpment of southern Africa derived from apatite fission track thermochronology: Journal of Geophysical Research: Solid Earth, v. 107, no. B12, p. 2350.

Buck, W. R., 1986, Small-scale convection induced by passive rifting: the cause for uplift of rift shoulders: Earth and Planetary Science Letters, v. 77, no. 3–4, p. 362-372.

Buck, W. R., 1991, Modes of continental lithospheric extension: Journal of Geophysical Research: Solid Earth, v. 96, no. B12, p. 20161-20178.

Carlson, W. D., Donelick, R. A., and Ketcham, R. A., 1999, Variability of apatite fission-track annealing kinetics: I. Experimental results: American mineralogist, v. 84, p. 1213-1223.

Centeno, J. P., 2005, Exhumation and incision history of the Torngat Mountains, northern Labrador and Quebec, Canada, using apatite (U-Th)/He thermochronology [MSc MSc. Thesis]: University of Kansas.

Chalmers, J. A., Green, P., Japsen, P., and Rasmussen, E. S., 2010, The Scandinavian mountains have not persisted since the Caledonian orogeny. A comment on Nielsen et al. (2009a): Journal of Geodynamics, v. 50, no. 2, p. 94-101.

Chalmers, J. A., and Laursen, K. H., 1995, Labrador Sea: the extent of continental and oceanic crust and the timing of the onset of seafloor spreading: Marine and Petroleum Geology, v. 12, no. 2, p. 205-217.

Chalmers, J. A., and Pulvertaft, T., 2001, Development of the continental margins of the Labrador Sea: a review: Geological Society, London, Special Publications, v. 187, no. 1, p. 77-105.

Creason, C. G., and Gosse, J. C., 2014, Preliminary characterization of the Mesozoic–Cenozoic exhumation history of Hall Peninsula, Baffin Island, Nunavut, based on apatite and zircon (U-Th)/He thermochronology: Summary of Activities 2013, Canada-Nunavut Geoscience Office, p. 93 - 100.

Creason, C. G., Gosse, J. C., and Young, M. D., 2013, Rift flank uplift and landscape evolution of Hall Peninsula, Baffin Island, Nunavut: an exhumation model based on low-temperature thermochronology: Summary of Activities 2012, Canada-Nunavut Geoscience Office, p. 75-84.

Ehlers, T. A., and Farley, K. A., 2003, Apatite (U–Th)/He thermochronometry: methods and applications to problems in tectonic and surface processes: Earth and Planetary Science Letters, v. 206, no. 1-2, p. 1-14.

Farley, K. A., 2000, Helium diffusion from apatite: General behavior as illustrated by Durango fluorapatite: Journal of Geophysical Research-Solid Earth, v. 105, no. B2, p. 2903-2914.

-, 2002, (U-Th)/He Dating: Techniques, Calibrations, and Applications: Reviews in Mineralogy and Geochemistry, v. 47, no. 1, p. 819-844.

Farley, K. A., Wolf, R. A., and Silver, L. T., 1996, The effects of long alpha-stopping distances on (U-Th)/He ages: Geochimica et Cosmochimica Acta, v. 60, no. 21, p. 4223-4229.

Flowers, R. M., 2009, Exploiting radiation damage control on apatite (U–Th)/He dates in cratonic regions: Earth and Planetary Science Letters, v. 277, no. 1-2, p. 148-155.

Flowers, R. M., Bowring, S. A., and Reiners, P. W., 2006, Low long-term erosion rates and extreme continental stability documented by ancient (U-Th)/He dates: Geology, v. 34, no. 11, p. 925.

Flowers, R. M., and Kelley, S. A., 2011, Interpreting data dispersion and "inverted" dates in apatite (U–Th)/He and fission-track datasets: An example from the US midcontinent: Geochimica et Cosmochimica Acta, v. 75, no. 18, p. 5169-5186.

Flowers, R. M., Ketcham, R. A., Shuster, D. L., and Farley, K. A., 2009, Apatite (U–Th)/He thermochronometry using a radiation damage accumulation and annealing model: Geochimica et Cosmochimica Acta, v. 73, no. 8, p. 2347-2365.

Flowers, R. M., and Schoene, B., 2010, (U-Th)/He thermochronometry constraints on unroofing of the eastern Kaapvaal craton and significance for uplift of the southern African Plateau: Geology, v. 38, no. 9, p. 827-830.

Flowers, R. M., Shuster, D. L., Wernicke, B. P., and Farley, K. A., 2007, Radiation damage control on apatite (U-Th)/He dates from the Grand Canyon region, Colorado Plateau: Geology, v. 35, no. 5, p. 447-450.

Funck, T., Gohl, K., Damm, V., and Heyde, I., 2012, Tectonic evolution of southern Baffin Bay and Davis Strait: Results from a seismic refraction transect between Canada and Greenland: Journal of Geophysical Research, v. 117, no. B4.

Funck, T., Jackson, H. R., Louden, K. E., and Klingelhöfer, F., 2007, Seismic study of the transform-rifted margin in Davis Strait between Baffin Island (Canada) and Greenland: What happens when a plume meets a transform: Journal of Geophysical Research, v. 112, no. B4.

Funck, T., and Louden, K. E., 1999, Wide-angle seismic transect across the Torngat Orogen, northern Labrador: Evidence for a Proterozoic crustal root: Journal of Geophysical Research: Solid Earth, v. 104, no. B4, p. 7463-7480.

Funck, T., Louden, K. E., Wardle, R. J., Hall, J., Hobro, J. W., Salisbury, M. H., and Muzzatti, A. M., 2000, Three-dimensional structure of the Torngat Orogen (NE Canada) from active seismic tomography: Journal of Geophysical Research-Solid Earth, v. 105, no. B10, p. 23403-23420.

Gallagher, K., and Brown, R., 1997, The onshore record of passive margin evolution: Journal of the Geological Society, v. 154, no. 3, p. 451-457.

-, 1999, Denudation and uplift at passive margins: the record on the Atlantic Margin of southern Africa: Philosophical Transactions of the Royal Society A: Mathematical, Physical and Engineering Sciences, v. 357, no. 1753, p. 835-859.

Gallagher, K., Hawkesworth, C. J., and Mantovani, M. S. M., 1994, The denudation history of the onshore continental margin of SE Brazil inferred from apatite fission track data: Journal of Geophysical Research, v. 99, no. B9, p. 18117-18145.

Gautheron, C., Barbarand, J., Ketcham, R. A., Tassan-Got, L., van der Beek, P., Pagel, M., Pinna-Jamme, R., Couffignal, F., and Fialin, M., 2013, Chemical influence on α-recoil damage annealing in apatite: Implications for (U–Th)/He dating: Chemical Geology, v. 351, p. 257-267.

Gautheron, C., Tassan-Got, L., Barbarand, J., and Pagel, M., 2009, Effect of alpha-damage annealing on apatite (U–Th)/He thermochronology: Chemical Geology, v. 266, no. 3-4, p. 157-170.

Gerlings, J., Funck, T., Jackson, H. R., Louden, K. E., and Klingelhöfer, F., 2009, Seismic evidence for plume-derived volcanism during formation of the continental margin in southern Davis Strait and northern Labrador Sea: Geophysical Journal International, v. 176, no. 3, p. 980-994.

Goldsmith, A. S., Creason, C. G., Stockli, D. F., and Ketcham, R. A., 2014, Using zircons from Hall Peninsula, Baffin Island, Nunavut to understand the effects of radiation damage on helium diffusion.: Summary of Activities 2013, Canada-Nunavut Geoscience Office, p. 101 – 108.

Green, P. F., Crowhurst, P. V., Duddy, I. R., Japsen, P., and Holford, S. P., 2006, Conflicting (U–Th)/He and fission track ages in apatite: Enhanced He retention, not anomalous annealing behaviour: Earth and Planetary Science Letters, v. 250, no. 3-4, p. 407-427.

Green, P. F., Duddy, I. R., Gleadow, A. J. W., Tingate, P. R., and Laslett, G. M., 1986, Thermal annealing of fission tracks in apatite: 1. A qualitative description: Chemical Geology: Isotope Geoscience section, v. 59, no. 0, p. 237-253.

Green, P. F., Japsen, P., Chalmers, J. A., and Bonow, J. M., 2011, Thermochronology, erosion surfaces and missing section in West Greenland: Journal of the Geological Society, v. 168, no. 4, p. 817-830.

Guenthner, W. R., Reiners, P. W., Ketcham, R. A., Nasdala, L., and Giester, G., 2013, Helium diffusion in natural zircon: Radiation damage, anisotropy, and the interpretation of zircon (U-Th)/He thermochronology: American Journal of Science, v. 313, no. 3, p. 145-198.

Henderson, A., 2007, ParaView guide: a parallel visualization application, Kitware Inc.

Hoffman, P. F., 1988, United Plates of America, the Birth of a Craton - Early Proterozoic Assembly and Growth of Laurentia: Annual Review of Earth and Planetary Sciences, v. 16, p. 543-603.

House, M. A., Wernicke, B. P., and Farley, K. A., 1998, Dating topography of the Sierra Nevada, California, using apatite (U-Th)/He ages: Nature, v. 396, no. 6706, p. 66-69.

Hurley, P. M., 1954, The helium age method and the distribution and migration of helium in rocks Nuclear Geology, p. 301–329.

Japsen, P., Bonow, J. M., Green, P. F., Chalmers, J. A., and Lidmar-Bergström, K., 2006, Elevated, passive continental margins: Long-term highs or Neogene uplifts? New evidence from West Greenland: Earth and Planetary Science Letters, v. 248, no. 1-2, p. 330-339.

Japsen, P., Chalmers, J. A., Green, P. F., and Bonow, J. M., 2012, Elevated, passive continental margins: Not rift shoulders, but expressions of episodic, post-rift burial and exhumation: Global and Planetary Change, v. 90-91, p. 73-86.

Japsen, P., Green, P. F., and Chalmers, J. A., 2005, Separation of Palaeogene and Neogene uplift on Nuussuaq, West Greenland: Journal of the Geological Society, v. 162, no. 2, p. 299-314.

-, 2013, The mountains of North-East Greenland are not remnants of the Caledonian topography. A comment on Pedersen et al. (2012): Tectonophysics vol. 530–531, p. 318–330: Tectonophysics, v. 589, p. 234-238.

Kessler, M. A., Anderson, R. S., and Briner, J. P., 2008, Fjord insertion into continental margins driven by topographic steering of ice: Nature Geoscience, v. 1, no. 6, p. 365-369.

Ketcham, R. A., 2005, Forward and Inverse Modeling of Low-Temperature Thermochronometry Data: Reviews in Mineralogy and Geochemistry, v. 58, no. 1, p. 275-314.

Ketcham, R. A., Carter, A., Donelick, R. A., Barbarand, J., and Hurford, A. J., 2007, Improved modeling of fission-track annealing in apatite: American Mineralogist, v. 92, no. 5-6, p. 799-810.

Kooi, H., and Beaumont, C., 1994, Escarpment Evolution on High-Elevation Rifted Margins - Insights Derived from a Surface Processes Model That Combines Diffusion, Advection, and Reaction: Journal of Geophysical Research-Solid Earth, v. 99, no. B6, p. 12191-12209.

Larsen, L. M., Heaman, L. M., Creaser, R. A., Duncan, R. A., Frei, R., and Hutchison, M., 2009, Tectonomagmatic events during stretching and basin formation in the Labrador Sea and the Davis Strait: evidence from age and composition of Mesozoic to Palaeogene dyke swarms in West Greenland: Journal of the Geological Society, v. 166, no. 6, p. 999-1012.

Lewry, J. F., and Collerson, K., 1990, The Trans-Hudson Orogen: extent, subdivision, and problems: The Early Proterozoic Trans-Hudson Orogen of North America. Edited by JF Lewry and MR Stauffer. Geological Association of Canada, Special Paper, v. 37, p. 1-14.

Lidmar-Bergström, K., Bonow, J. M., and Japsen, P., 2013, Stratigraphic Landscape Analysis and geomorphological paradigms: Scandinavia as an example of Phanerozoic uplift and subsidence: Global and Planetary Change, v. 100, p. 153-171.

Lippolt, H. J., Leitz, M., Wernicke, R. S., and Hagedorn, B., 1994, (Uranium + thorium)/helium dating of apatite: experience with samples from different geochemical environments: Chemical Geology, v. 112, no. 1–2, p. 179-191.

Machado, G., Bilodeau, C., Takpanie, R., St-Onge, M., Rayner, N., Skipton, D., From, R., MacKay, C., Creason, C., and Braden, Z., 2013, Hall Peninsula regional bedrock mapping, Baffin Island, Nunavut: summary of fieldwork: Summary of Activities 2012, Canada-Nunavut Geoscience Office, p. 13-22.

MacLean, B., Jansa, L. F., Falconer, R. K. H., and Srivastava, S. P., 1977, Ordovician strata on the southeastern Baffin Island shelf revealed by shallow drilling: Canadian Journal of Earth Sciences, v. 14, no. 8, p. 1925-1939.

MacLean, B., Srivastava, S., and Haworth, R., 1982, Bedrock structures off Cumberland Sound, Baffin Island Shelf: core sample and geophysical data: Canadian Society of Petroleum Geologists, v. Arctic Geology and Geophysics: Proceedings of the Third International Symposium on Arctic Geology — Memoir 8, 1982, p. 279-295.

MacLean, B., Williams, G. L., Jennings, A., and Blakeney, C., 1986, Bedrock and surficial geology of Cumberland Sound, N.W.T.: Current Resarch; Geological Survey of Canada, Paper 86-1B, p. 605-615.

Marquette, G. C., Gray, J. T., Gosse, J. C., Courchesne, F., Stockli, L., Macpherson, G., and Finkel, R., 2004, Felsenmeer persistence under non-erosive ice in the Torngat and Kaumajet mountains, Quebec and Labrador, as determined by soil weathering and cosmogenic nuclide exposure dating: Canadian Journal of Earth Sciences, v. 41, no. 1, p. 19-38.

McGregor, E. D., Nielsen, S. B., Stephenson, R. A., Clausen, O. R., Petersen, K. D., and Macdonald, D. I. M., 2012, Evolution of the west Greenland margin: offshore thermostratigraphic data and modelling: Journal of the Geological Society, v. 169, no. 5, p. 515-530.

McGregor, E. D., Nielsen, S. B., Stephenson, R. A., Petersen, K. D., and MacDonald, D. I. M., 2013, Long-term exhumation of a Palaeoproterozoic orogen and the role of pre-existing heterogeneous thermal crustal properties: a fission-track study of SE Baffin Island: Journal of the Geological Society, v. 170, no. 6, p. 877-891.

McKenzie, D., 1978, Some remarks on the development of sedimentary basins: Earth and Planetary Science Letters, v. 40, no. 1, p. 25-32.

Montgomery, D. R., 2002, Valley formation by fluvial and glacial erosion: Geology, v. 30, no. 11, p. 1047-1050.

Nasdala, L., Reiners, P. W., Garver, J. I., Kennedy, A. K., Stern, R. A., Balan, E., and Wirth, R., 2004, Incomplete retention of radiation damage in zircon from Sri Lanka: American Mineralogist, v. 89, no. 1, p. 219-231.

Nielsen, S. B., Clausen, O. R., Jacobsen, B. H., Thomsen, E., Huuse, M., Gallagher, K., Balling, N., and Egholm, D., 2010, The ICE hypothesis stands: How the dogma of late Cenozoic tectonic uplift can no longer be sustained in the light of data and physical laws: Journal of Geodynamics, v. 50, no. 2, p. 102-111.

Nielsen, S. B., Gallagher, K., Egholm, D. L., Clausen, O. R., and Summerfield, M., 2009a, Reply to comment regarding the ICE-hypothesis: Journal of Geodynamics, v. 48, no. 2, p. 101-106.

Nielsen, S. B., Gallagher, K., Leighton, C., Balling, N., Svenningsen, L., Jacobsen, B. H., Thomsen, E., Nielsen, O. B., Heilmann-Clausen, C., Egholm, D. L., Summerfield, M. A., Clausen, O. R., Piotrowski, J. A., Thorsen, M. R., Huuse, M., Abrahamsen, N., King, C., and Lykke-Andersen, H., 2009b, The evolution of western Scandinavian topography: A review of Neogene uplift versus the ICE (isostasy–climate–erosion) hypothesis: Journal of Geodynamics, v. 47, no. 2-3, p. 72-95.

Oakey, G. N., and Chalmers, J. A., 2012, A new model for the Paleogene motion of Greenland relative to North America: Plate reconstructions of the Davis Strait and Nares Strait regions between Canada and Greenland: Journal of Geophysical Research: Solid Earth, v. 117, no. B10, p. n/a-n/a.

Osmundsen, P. T., and Redfield, T. F., 2011, Crustal taper and topography at passive continental margins: Terra Nova, v. 23, no. 6, p. 349-361.

Parsiegla, N., Stankiewicz, J., Gohl, K., Ryberg, T., and Uenzelmann-Neben, G., 2009, Southern African continental margin: Dynamic processes of a transform margin: Geochemistry, Geophysics, Geosystems, v. 10, no. 3, p. n/a-n/a.

Pedersen, V. K., Nielsen, S. B., and Gallagher, K., 2012, The post-orogenic evolution of the Northeast Greenland Caledonides constrained from apatite fission track analysis and inverse geodynamic modelling: Tectonophysics, v. 530–531, no. 0, p. 318-330.

Pedersen, V. K., Nielsen, S. B., and Gallagher, K., 2013, Reply to: "The mountains of North-East Greenland are not remnants of the Caledonian topography. A comment on Pedersen et al. (2012)": Tectonophysics, v. 589, no. 0, p. 239-244.

Perry, H. K. C., Jaupart, C., Mareschal, J. C., and Bienfait, G., 2006, Crustal heat production in the Superior Province, Canadian Shield, and in North America inferred from heat flow data: Journal of Geophysical Research: Solid Earth, v. 111, no. B4.

Persano, C., Stuart, F. M., Bishop, P., and Barfod, D. N., 2002, Apatite (U–Th)/He age constraints on the development of the Great Escarpment on the southeastern Australian passive margin: Earth and Planetary Science Letters, v. 200, no. 1–2, p. 79-90.

Rayner, N. M., 2014, New U-Pb geochronological results from Hall Peninsula, Baffin Island, Nunavut: Summary of Activities 2013, Canada-Nunavut Geoscience Office, p. 39-52.

Redfield, T. F., 2010, On apatite fission track dating and the Tertiary evolution of West Greenland topography: Journal of the Geological Society, v. 167, no. 2, p. 261-271.

Redfield, T. F., and Osmundsen, P. T., 2012, The long-term topographic response of a continent adjacent to a hyperextended margin: A case study from Scandinavia: Geological Society of America Bulletin, v. 125, no. 1-2, p. 184-200.

Reiners, P. W., 2005, Zircon (U-Th)/He Thermochronometry: Reviews in Mineralogy and Geochemistry, v. 58, no. 1, p. 151-179.

Reiners, P. W., and Farley, K. A., 2001, Influence of crystal size on apatite (U–Th)/He thermochronology: an example from the Bighorn Mountains, Wyoming: Earth and Planetary Science Letters, v. 188, no. 3–4, p. 413-420.

Reiners, P. W., Spell, T. L., Nicolescu, S., and Zanetti, K. a., 2004, Zircon (U-Th)/He thermochronometry: He diffusion and comparisons with 40Ar/39Ar dating: Geochimica et Cosmochimica Acta, v. 68, no. 8, p. 1857-1887.

Rey, P. F., Philippot, P., and Thébaud, N., 2003, Contribution of mantle plumes, crustal thickening and greenstone blanketing to the 2.75–2.65 Ga global crisis: Precambrian Research, v. 127, no. 1–3, p. 43-60.

Sambridge, M., 1999a, Geophysical inversion with a neighbourhood algorithm—I. Searching a parameter space: Geophysical Journal International, v. 138, no. 2, p. 479-494.

-, 1999b, Geophysical inversion with a neighbourhood algorithm—II. Appraising the ensemble: Geophysical Journal International, v. 138, no. 3, p. 727-746.

Sanford, B., 1987, Paleozoic geology of the Hudson Platform: Canadian Society of Petroleum Geologists, v. CSPG Special Publications, no. Sedimentary Basins and Basin-Forming Mechanisms — Memoir 12, 1987, p. 483 - 505.

Sanford, B., and Grant, A., 1990, New findings relating to the stratigraphy and structure of the Hudson Platform; in, Interior Plains and Arctic Canada; Current Research, Part D, Geological Survey of Canada, Paper no. 90-1D: Geological Survey of Canada, Current Research, p. 17-30.

-, 1998, Paleozoic and Mesozoic geology of the Hudson and southeast Arctic Platforms: Geological Survey of Canada; Open file 3595.

-, 2000, Geological framework of the Ordovician System in the southeast Arctic platform, Nunavut: Geological Survey of Canada, Bulletin, v. 557, p. 13-38.

Schenk, C. J., 2011, Chapter 41 Geology and petroleum potential of the West Greenland-East Canada Province: Geological Society, London, Memoirs, v. 35, no. 1, p. 627-645.

Scott, D., 1996, Geology of the Hall Peninsula east of Iqaluit, southern Baffin Island, Northwest Territories: Current Research, Geological Survey of Canada, p. 83-91.

Scott, D. J., 1999, U–Pb geochronology of the eastern Hall Peninsula, southern Baffin Island, Canada: a northern link between the Archean of West Greenland and the Paleoproterozoic Torngat Orogen of northern Labrador: Precambrian Research, v. 93, no. 1, p. 5-26.

Shuster, D. L., and Farley, K. A., 2009, The influence of artificial radiation damage and thermal annealing on helium diffusion kinetics in apatite: Geochimica Et Cosmochimica Acta, v. 73, no. 1, p. 183-196.

Shuster, D. L., Flowers, R. M., and Farley, K. A., 2006, The influence of natural radiation damage on helium diffusion kinetics in apatite: Earth and Planetary Science Letters, v. 249, no. 3-4, p. 148-161.

Skaarup, N., Jackson, H. R., and Oakey, G., 2006, Margin segmentation of Baffin Bay/Davis Strait, eastern Canada based on seismic reflection and potential field data: Marine and Petroleum Geology, v. 23, no. 1, p. 127-144.

Skipton, D., Schneider, D., Kellett, D., and Joyce, N., 2015, New insights on the cooling history of Hall Peninsula, southern Baffin Island, Nunavut, using 40 Ar/39 Ar thermochronology on muscovite: Summary of Activities 2014, Canada-Nunavut Geoscience Office, p. 17-30.

Skipton, D. R., Schneider, D. A., St-Onge, M. R., Braden, Z. M., and Young, M. D., A wet affair: the middle orogenic crust of the Trans-Hudson Orogen, Baffin Island, Nunavut
, *in* Proceedings 2013 GSA Annual Meeting Denver, CO, 2013.

Spotila, J. A., Bank, G. C., Reiners, P. W., Naeser, C. W., Nancy, D., and Henika, B. S., 2004, Origin of the Blue Ridge escarpment along the passive margin of Eastern North America, p. 41-63.

St-Onge, M. R., Van Gool, J. A. M., Garde, A. A., and Scott, D. J., 2009, Correlation of Archaean and Palaeoproterozoic units between northeastern Canada and western Greenland: constraining the pre-collisional upper plate accretionary history of the Trans-Hudson orogen: Geological Society, London, Special Publications, v. 318, no. 1, p. 193-235.

Staiger, J. K. W., Gosse, J. C., Johnson, J. V., Fastook, J., Gray, J. T., Stockli, D. F., Stockli, L., and Finkel, R., 2005, Quaternary relief generation by polythermal glacier ice: Earth Surface Processes and Landforms, v. 30, no. 9, p. 1145-1159.

Suckro, S. K., Gohl, K., Funck, T., Heyde, I., Ehrhardt, A., Schreckenberger, B., Gerlings, J., Damm, V., and Jokat, W., 2012, The crustal structure of southern Baffin Bay: implications from a seismic refraction experiment: Geophysical Journal International, v. 190, no. 1, p. 37-58.

Suckro, S. K., Gohl, K., Funck, T., Heyde, I., Schreckenberger, B., Gerlings, J., and Damm, V., 2013, The Davis Strait crust--a transform margin between two oceanic basins: Geophysical Journal International, v. 193, no. 1, p. 78-97.

Sugden, D. E., 1976, A case against deep erosion of shields by ice sheets: Geology, v. 4, no. 10, p. 580-582.

Todd, B. J., and Keen, C. E., 1989, Temperature Effects and Their Geological Consequences at Transform Margins: Canadian Journal of Earth Sciences, v. 26, no. 12, p. 2591-2603.

Umpleby, D. C., 1979, Geology of the Labrador shelf: Geological Survey of Canada, Paper 79-13.

Valla, P. G., van der Beek, P. A., Shuster, D. L., Braun, J., Herman, F., Tassan-Got, L., and Gautheron, C., 2012, Late Neogene exhumation and relief development of the Aar and Aiguilles Rouges massifs (Swiss Alps) from low-temperature thermochronology modeling and 4He/3He thermochronometry: Journal of Geophysical Research, v. 117, no. F1.

van der Beek, P., Andriessen, P., and Cloetingh, S., 1995, Morphotectonic evolution of rifted continental margins: Inferences from a coupled tectonic-surface processes: Tectonics, v. 14, no. 2, p. 406-421.

Watt, W. S., 1969, The coast-parallel dike swarm of southwest Greenland in relation to the opening of the Labrador Sea: Canadian Journal of Earth Sciences, v. 6, no. 5, p. 1320-1321.

Wolf, R. A., Farley, K. A., and Kass, D. M., 1998, Modeling of the temperature sensitivity of the apatite (U-Th)/He thermochronometer: Chemical Geology, v. 148, no. 1-2, p. 105-114.

Yaehne, S., 2008, Apatite (U-Th-Sm)/He thermochronology of the Eastern Arctic Rim: Evolution of the north-central Baffin Island rifted margin [BSc. Honours Thesis: Dalhousie University.

Zhang, S., 2013, Rock Eval and Vitrinite Reflectance Data from Baffin Island Shelf and Hudson Strait: Geological Survey of Canada, Open File 7341, p. 1-29.

Zhang, S., Creaser, R. A., Pell, J., and Stasiuk, V., 2014, Discovery of organic-rich black shale xenolith from kimberlite on the Hall Peninsula, Nunavut and its implication for petroleum potential in Cumberland Sound: Bulletin of Canadian Petroleum Geology, v. 62, no. 3, p. 125-131.

Zhang, S., and Pell, J., 2013, Study of sedimentary rock xenoliths from kimberlites on Hall Peninsula, Baffin Island, Nunavut: Summary of Activities 2012, Canada-Nunavut Geoscience Office, p. 107-112.

Zhang, S., and Pell, J., 2014, Conodonts recovered from the carbonate xenoliths in the kimberlites confirm the Paleozoic cover on the Hall Peninsula, Nunavut: Canadian Journal of Earth Sciences, v. 51, no. 2, p. 142-155.